

---

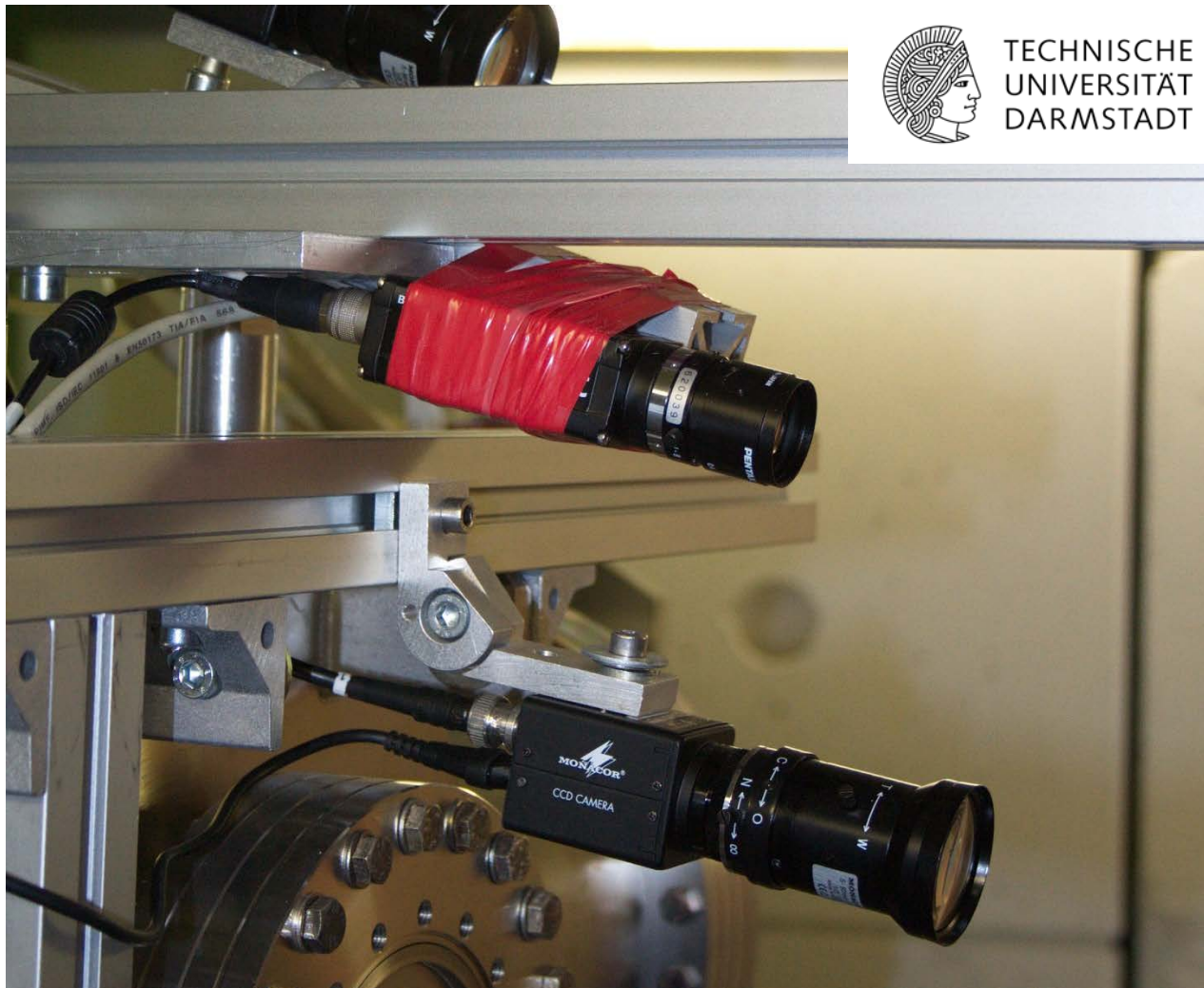
# Radiation Effects on Semiconductor Devices in High Energy Heavy Ion Accelerators

---

Strahlungseffekte auf Halbleiter-Bauelemente in Hochenergie-Schwerionen-Beschleunigern

Zur Erlangung des akademischen Grades eines Doktors der Naturwissenschaften (Dr. rer. nat.)  
vorgelegte Dissertation von Anton Belousov aus Moskau, Russland  
September 2014 – Darmstadt – D17

---



TECHNISCHE  
UNIVERSITÄT  
DARMSTADT





---

Radiation Effects on Semiconductor Devices in High Energy Heavy Ion  
Accelerators

Strahlungseffekte auf Halbleiter-Bauelemente in Hochenergie-Schwerionen-  
Beschleunigern

Vom Fachbereich Material- und Geowissenschaften der Technischen Universität  
Darmstadt

zur Erlangung des akademischen Grades eines Doktors der Naturwissenschaften  
(Dr. rer. nat.) genehmigte Dissertation von Anton Belousov M. Sc. aus Moskau,  
Russland

1. Gutachten: Prof. Dr. Wolfgang Ensinger
2. Gutachten: Prof. Dr. Marco Durante

Tag der Einreichung: 24.09.2014

Tag der mündlichen Prüfung: 20.10.2014

Darmstadt 2014

D17

---

## **Erklärung zur Dissertation**

Hiermit versichere ich, die vorliegende Dissertation ohne Hilfe Dritter nur mit den angegebenen Quellen und Hilfsmitteln angefertigt zu haben. Alle Stellen, die aus Quellen entnommen wurden, sind als solche kenntlich gemacht. Diese Arbeit hat in gleicher oder ähnlicher Form noch keiner Prüfungsbehörde vorgelegt.

Darmstadt, 24.09.2014

---

(Anton Belousov)



---

## Zusammenfassung

Strahleneffekte auf Halbleiter-Bauelemente am GSI Helmholtz-Zentrum für Schwerionenforschung nehmen stark an Bedeutung zu wegen des Anstiegs an Strahlintensität aufgrund des Ausbaus der Anlagen. Darüber hinaus wird derzeit ein neuer Beschleuniger im Rahmen des Projektes *Facility for Antiproton and Ion Research* (FAIR) aufgebaut. Die Strahlintensitäten werden hier um den Faktor 100 und die Energien um den Faktor 10 erhöht werden. Die Strahlenfelder in der Umgebung der Strahlrohre werden um mehr als 2 Größenordnungen ansteigen, begleitet von einer entsprechenden Auswirkung auf Halbleiter-basierte Geräte. Daher ist es notwendig, eine Studie zur Strahlenwirkung auf elektronische Geräte unter Berücksichtigung der spezifischen Eigenschaften der Strahlung, die typisch für Hochenergie-Schwerionen-Beschleuniger ist, durch zu führen.

Strahleneffekte auf Elektronikkomponenten in einer Beschleunigerumgebung lassen sich in zwei Kategorien aufteilen: kurzzeitige zeitlich limitierte Effekte und Langzeiteffekte mit andauernder Schädigung. Beide können problematisch für die richtige Funktion elektronischer Geräte sein. Die vorliegende Arbeit bezieht sich auf Strahlenschäden von CCD-Kameras im Strahlenfeld von Schwerionenbeschleunigern. Es wurden verschiedene Serien von Experimenten mit Bestrahlung von Komponenten (*Devices under Test* DUT) durch Sekundärstrahlung durchgeführt, welche durch Strahlverluste entsteht. Dazu wurden Monte Carlo Berechnungen zur Simulation der experimentellen Bedingungen sowie der Bedingungen der zukünftigen Beschleuniger durchgeführt. Diese wurden verglichen und daraus Schlussfolgerungen gezogen. Weiterhin wurde eine weitere Komponente an Beschleunigereinrichtungen getestet, nämlich Ethernet Schalter. Zusätzlich wurden direkte Bestrahlungen von CCDs und MOS Chips mit Schwerionen durchgeführt. Die typischen Energien der Primärionen betragen dabei 0,5 bis 1 GeV/u, die Ionensorten reichten von Natrium bis Uran, die

---

Intensitäten des Strahls bis zu  $1E9$  Ionen pro Spill mit Spilldauern von 200 bis 300 ns.

Kriterien der Zuverlässigkeit und Lebensdauern der DUTs unter spezifischen Bestrahlungsbedingungen wurden formuliert, basierend auf den experimentellen Resultaten der Arbeit. Es wurden Vorhersagen getroffen zur elektronischen Bauteil-Zuverlässigkeit und Betriebslebensdauer unter den für FAIR erwarteten Bedingungen, basierend auf Monte Carlo Simulationen. Zusätzlich zu den Hauptergebnissen wurde ein neuartiger Typ von CCD-basiertem Strahlverlust-Monitor (*beam loss monitor* BLM) vorgeschlagen und diskutiert.

---

## Abstract

Radiation effects on semiconductor devices in GSI Helmholtz Center for Heavy Ion Research are becoming more and more significant with the increase of beam intensity due to upgrades. Moreover a new accelerator is being constructed on the basis of GSI within the project of facility for antiproton and ion research (FAIR). Beam intensities will be increased by factor of 100 and energies by factor of 10. Radiation fields in the vicinity of beam lines will increase more than 2 orders of magnitude and so will the effects on semiconductor devices. It is necessary to carry out a study of radiation effects on semiconductor devices considering specific properties of radiation typical for high energy heavy ion accelerators.

Radiation effects on electronics in accelerator environment may be divided into two categories: short-term temporary effects and long-term permanent degradation. Both may become critical for proper operation of some electronic devices. This study is focused on radiation damage to CCD cameras in radiation environment of heavy ion accelerator. Series of experiments with irradiation of devices under test (DUTs) by secondary particles produced during ion beam losses were done for this study. Monte Carlo calculations were performed to simulate the experiment conditions and conditions expected in future accelerator. Corresponding comparisons and conclusions were done. Another device typical for accelerator facilities - industrial Ethernet switch was tested in similar conditions during this study. Series of direct irradiations of CCD and MOS transistors with heavy ion beams were done as well. Typical energies of the primary ion beams were 0.5-1 GeV/u. Ion species: from Na to U. Intensities of the beam up to  $1e9$  ions/spill with spill length of 200-300 ns.

Criteria of reliability and lifetime of DUTs in specific radiation conditions were formulated, basing on experimental results of the study. Predictions of electronic device reliability and lifetime were formulated for radiation conditions

---

expected in future at FAIR, basing on Monte Carlo simulations. In addition to main results a new type of CCD-based beam loss monitor (BLM) was proposed and discussed.

---

## Abbreviations

APPA	Atomic physics, Plasma Physics and Applications
BJT	Bipolar Junction Transistor
BLM	Beam Loss Monitor
CCD	Charge-Coupled Devices
CCTV	Closed-Circuit Television
CMOS	Complementary Metal–Oxide–Semiconductor
CPLD	Complex Programmable Logic Device
DN	Digital Number
DPA	Displacements per Atom
DRAM	Dynamic Random-Access Memory
DUT	Device under Test
EEPROM	Electrically Erasable Programmable Read-Only Memory
EPR	Electron Paramagnetic Resonance
FPGA	Field-Programmable Gate Array
FPS	Frames per Second
GSI	Helmholtz Center for Heavy Ion Research
HHD	High energy High intensity Dump
LET	Linear Energy Transfer

---

MOS	Metal Oxide Semiconductor
NMOS	N-Type Metal-Oxide-Semiconductor
PMOS	P-Type Metal-Oxide-Semiconductor
RAM	Random-Access Memory
SEB	Single Event Burnout
SEE	Single Event Effect
SEFI	Single Event Functional Interrupt
SEGR	Single Event Gate Rupture
SEL	Single Event Latch-up
SES	Single Event Snapback
SET	Single Event Transient
SEU	Single Event Upset
SIPMOS	Siemens P-Type Metal-Oxide-Semiconductor
SIS18	Heavy Ion Synchrotron
SOI	Silicon-On-Insulator
STD	Standard Deviation
TID	Total Ionisation Dose
UNILAC	Universal Linear Accelerator
VDMOS	Vertical Diffused Metal Oxide Semiconductor
VMOS	Vertical Metal Oxide Semiconductor

---

# TABLE OF CONTENT

---

<b>1. Introduction .....</b>	<b>9</b>
<b>2. Theory .....</b>	<b>17</b>
2.1. The influence of radiation on electronic devices .....	17
2.2. Gamma-ray damage effects .....	19
2.3. Degradation of MOS transistor parameters .....	23
2.4. Neutron damage effects .....	29
2.5. Single event effects .....	33
2.5.1.Non-destructive effects .....	34
2.5.2.Destructive effects .....	36
<b>3. Simulations .....</b>	<b>41</b>
3.1.FLUKA Monte Carlo Tool .....	41
3.2.Monte Carlo Simulations .....	43
<b>4. Experimental methods .....</b>	<b>51</b>
4.1. Beams .....	51
4.2. Target and device setup .....	53
4.3. MOS transistor testing circuit .....	57
4.4. CCD readout .....	61
4.4.1.Digital – LabVIEW based code .....	61
4.4.2.Digital CCD calibration .....	65
4.4.3.Analogue CCD acquisition .....	69
4.5. Switch testing technique .....	73
4.6. Dosimetry .....	75

---

<b>5. Results and discussion .....</b>	<b>79</b>
5.1. Indirect irradiation effects .....	79
5.1.1.Long term effects in CCD cameras .....	79
5.1.2.Short term effects in CCD cameras .....	83
5.1.3.Ethernet switch stability and SEU in digital devices .....	93
5.2. Direct irradiation effects .....	95
5.2.1.Long term effects in MOS transistor .....	95
5.2.2.Degradation of CCD sensor from direct ion beam .....	97
<b>6. CCD based beam loss monitors .....</b>	<b>101</b>
<b>7. Summary .....</b>	<b>109</b>
<b>Appendix .....</b>	<b>111</b>
<b>References .....</b>	<b>113</b>

---

# Introduction

---

Radiation damage to materials is a topical and wide field of study in modern science. Study of radiation effects on electronic components is a very important segment of this field, because one already can hardly imagine a world without various electronic devices for ordinary life, scientific or military purposes. Moreover silicon-based technology has proven to be relatively sensitive to radiation.

Radiation effects on electronics were first observed during above-ground nuclear bomb tests in 1954 [1]. Spurious signals and malfunctions of the measuring equipment were observed. During nuclear explosion most of the energy is released in form of neutrons, gamma rays, alpha particles and electrons. Temporary errors in electronics or so called single event effects (SEEs) were mainly caused by neutrons, while gammas were responsible for permanent effects like modification of characteristics of electronic components [2]. Since 1958 similar anomalies were registered in electronic devices operating in space. For example heavy ions from cosmic rays disturbed operation of transmitting modules of Explorer 1 (Fig 1.1).

On the ground level single event upsets (SEUs) were first reported during 2 kB dynamic random access memory (DRAM) tests. In that case SEUs were not triggered by cosmic rays, but by alpha particles from the decay of Thorium and Uranium present in some integrated circuit packaging materials. It was the time when IBM first noticed a serious problem with memory reliabilities and initiated a research to understand the problem better. Later more cases of errors were observed in many applications including space, military and avionics. IBM employee James Ziegler noticed SEUs in commercial devices triggered by cosmic rays at ground level [3].

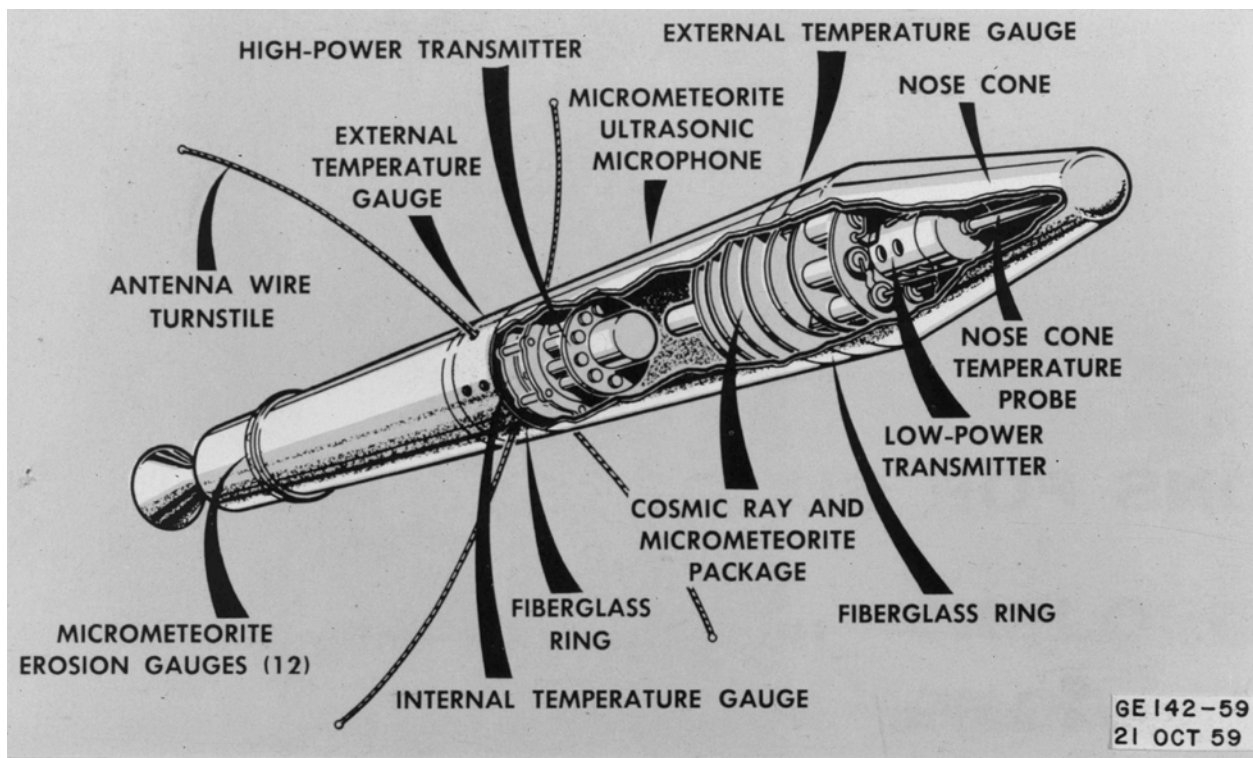


Fig 1.1: Explorer 1.

Another type of radiation sources are particle accelerators. With the launch of the first high energy synchrotrons in Brookhaven, Dubna, CERN, DESY and Fermi Lab it became clear that the radiation environment of such accelerators may be rather harsh for electronic devices. Different components of the beam diagnostic and machine control tools were located in the nearest vicinity of beam path. When high energy particles deviated from primary trajectory or collided with dense material according to experiment plan, a radiation field was produced. Thereby electronic components were repeatedly exposed to radiation in the accelerator environment.

Studies of radiation damage to electronic components may be divided into the following subgroups:

1. Military purposes. Destructive effects of radiation from nuclear weapons and electromagnetic pulse (EMP) weapons [1-2].

- 
2. Space and aeronautics research. Effects of cosmic rays on space, aero and terrestrial equipment [3-5].
  3. Particle accelerator and laser related studies. Effects of secondary radiation produced by beam interactions on various equipment or direct irradiation effects.

Various numbers of accelerators and equipment pieces, rapid development and increase of intensities and therefore radiation levels make the last subgroup especially relevant and topical in modern science.

Different accelerators may have different particular qualities of radiation environment. That is why it is often necessary to carry out individual studies of radiation damage to electronic components at each facility.

GSI Helmholtz Center for Heavy Ion Research (GSI) is a unique facility, equipped with linear accelerator (UNILAC) and synchrotron (SIS18) for acceleration of heavy ions (Fig. 1.2). It can operate with ion species up to Uranium, accelerating them up to 1 GeV/u at  $10^9$  ions/spill intensity (for Uranium). Moreover it is being upgraded in order to have a several times maximum intensity increase, and it will be used as an injection for the larger accelerator – facility for antiproton and ion research (FAIR). FAIR concept and design was first presented in 2001 [6-8]. The new facility will open opportunities for experiments in high-energy physics in the fields of nuclear structure, hadrons, atomic physics, biological and material sciences. FAIR will consist of a complex accelerator system, using GSI synchrotron SIS18 as an injection (Fig. 1.3). SIS 100 and SIS 300 synchrotrons will be operating with 100 times higher beam intensities, than those that are currently available at GSI. Moreover the energy of heavy ion beams will increase by a factor of 10 (table 1.1).

## Beschleunigeranlage

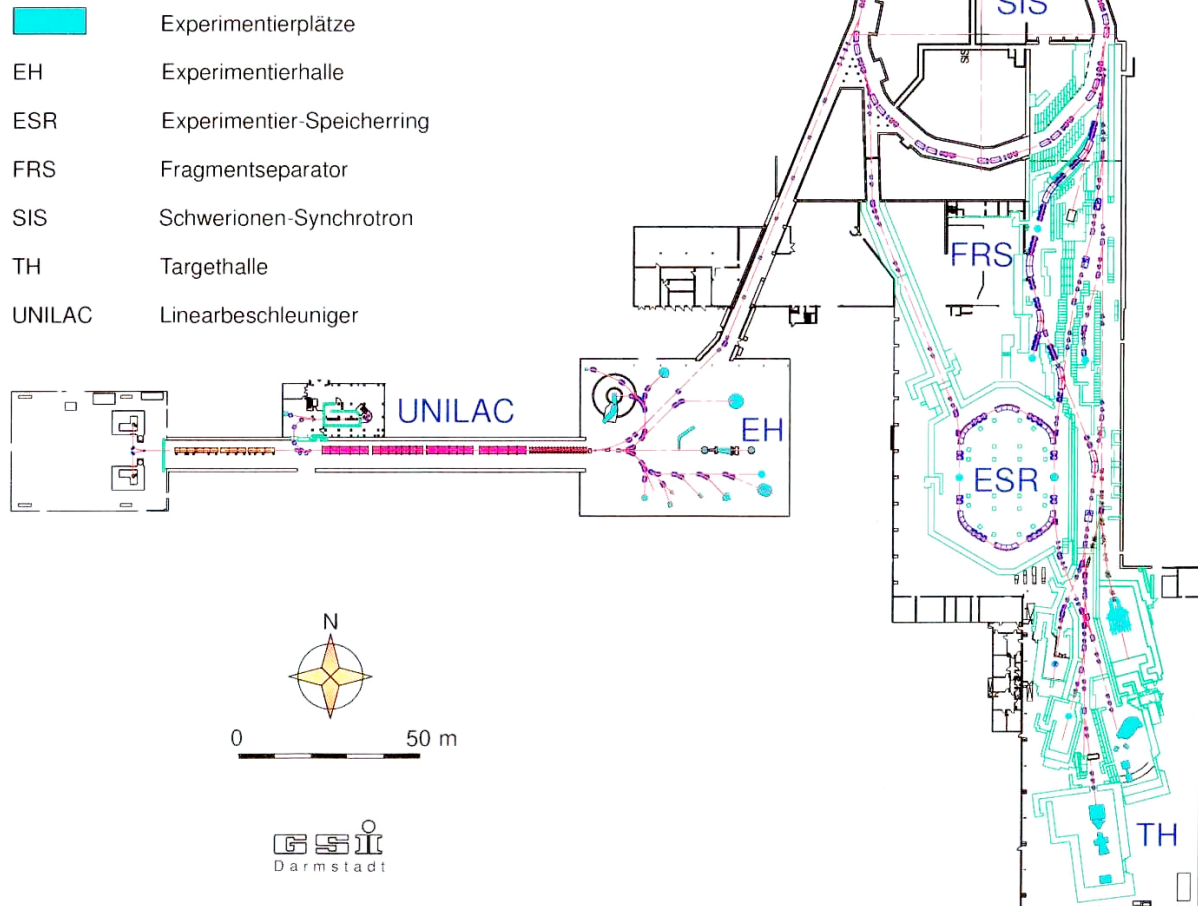


Fig. 1.2: Scheme of GSI facilities.

Failure of digital equipment and distortions of signals from cameras as well as degradation of performance of some devices were already reported in GSI. With the upcoming upgrade and construction of FAIR this issue became critically important. A study of radiation damage to electronic components considering specific properties of the radiation environment was necessary.

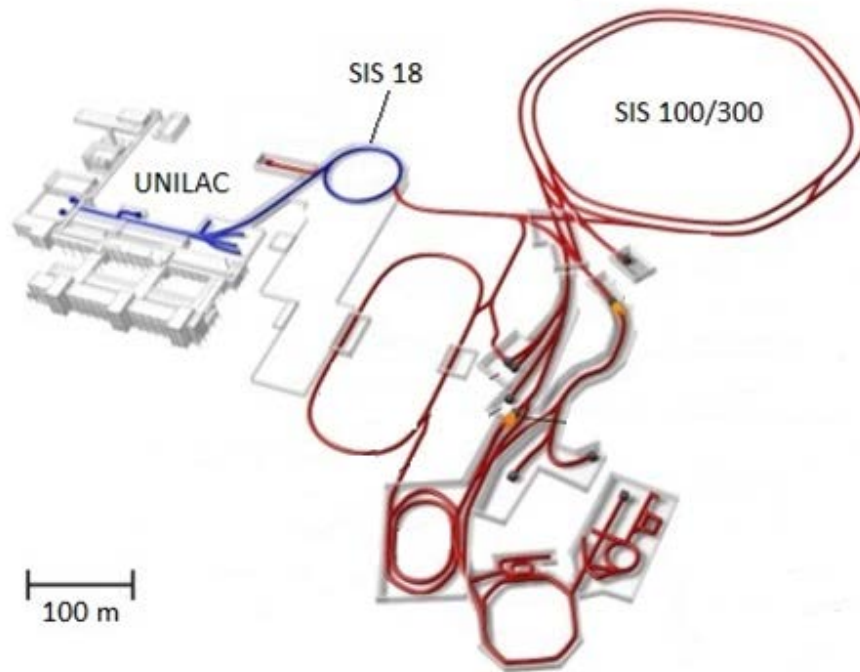


Fig. 1.3: Scheme of FAIR. Existing GSI accelerator is colored in blue.

Table 1.1: Overview of scientific topics and their demands at FAIR

Research Field	Energy	Peak Intensity	Average Intensity
Radioactive Ion Beams	0.4-1.5 GeV/u all Elements	$5 \times 10^{11}$ ions/pulse	$3 \times 10^{11}$ ions/s
Antiprotons	29 GeV	$4 \times 10^{13}$ ions/cycle	-
Dense Nuclear Matter	34 GeV/u Uranium	-	$2 \times 10^9$ ions/s
Plasma Physics	0.4-1 GeV/u	$1 \times 10^{12}$ ions/pulse	-
Atomic Physics	1-10 GeV/u	-	$1 \times 10^9$ ions/s

The aim of this study was to investigate short and long term effects of radiation to electronic devices in conditions typical for the high energy heavy ion accelerator. CCD cameras were proposed as a primary object of the study for two reasons.

---

First, it is a device that has many similar electronic elements – CCD matrix cells. It gives a benefit of high statistics. Second, CCD cameras are a typical device, frequently used in accelerator facilities for surveillance, target alignment and beam diagnostics. Another typical device – an Ethernet network switch was tested for radiation induced failures. The following objectives were considered during the study:

- criteria of CCD camera reliability and lifetime were formulated
- criteria of Ethernet switch reliability were formulated
- series of Monte Carlo simulations were performed in order to extrapolate results onto radiation conditions of specific locations in future facilities
- direct high energy heavy ion beam effect on semiconductors was investigated
- CCD camera was proven to be a good basis for construction of the new type of beam loss monitor (BLM)

### **Structure of the thesis**

**1. Introduction** section gives general description of the topic being studied. It includes a short background on the subject. Motivation is explained by means of gap statement. Aims of the study and achieved objectives are briefly described. Structure of thesis is given.

**2. Theory** section includes description of the principal phenomena causing radiation damage to electronic devices: ionization, displacement damage. Degradation of MOS parameters due to radiation is explained, single event effects (SEE) are classified and overviewed.

**3. Simulations** section describes part of study related to Monte Carlo code FLUKA. It includes simulations of experiments performed during this study,

---

comparison of calculated dose levels with experimental data, simulations of radiation conditions at FAIR and corresponding comparisons.

**4. Experimental methods** section starts with brief overview of GSI accelerator and used beam parameters. It follows with a description of every part of experimental equipment and complete assembly. This section also describes a development of custom LabVIEW based applications for data acquisition and processing. Dosimetry technique is mentioned in the end.

**5. Results and discussion** section contains all the results and is divided into subsections for each device under test (DUT). The results are followed by discussions.

**6. CCD based beam loss monitors** section describes how CCD camera may be used in a role of beam loss monitor (BLM). Advantages, disadvantages and possible improvements of the technique are stated.

**7. Summary** section contains a conclusion and sums up all the knowledge and experience obtained during this work.

**8. Appendix** contains further simulation results.



## 2. Theory

### 2.1 The influence of radiation on electronic devices

Radiation effects on silicon components may be divided in two main groups: ionizing effect and displacement damage. Semiconductor components may change their electronic properties due to radiation. Ionizing particles may produce charge in sensitive areas of devices. In general radiation effects may finally lead to functional failures of electronic systems and even to irreversible destructive effects. Neutrons and gammas are normally making the main contribution to radiation damage effects in accelerator environment. Table 2.1 shows the corresponding interaction types and significance of radiation damage type [9, 10].

Table 2.1: Neutron and gamma radiation effects on silicon components.

Radiation type	Energy range	Main type of interaction	Primary effects in Si and SiO <sub>2</sub>	Secondary effects in Si and SiO <sub>2</sub>
Photons	Low Energy	Photoelectric effect	Ionizing phenomena	Displacement damage
	Medium Energy	Compton Effect		
	High Energy	Pair production		
Neutrons	Low energy	Capture and nuclear reaction	Displacement damage	Ionizing phenomena
	High energy	Elastic scattering		

Interaction of high energy particles with matter may be described with the following phenomena:

1. Ionization of the material through the interaction with shell electrons
2. Displacement of target material atoms
3. Nuclear reaction with the target nucleus

All of the above mentioned processes may coexist and in some cases may even be triggered by one incident particle. For example a neutron can first interact with nucleus, creating displacement damage, than generate secondary charged particles, which ionize the material if they have enough energy. In case of incident high energetic charged particles ionizing dose effect predominates [9]. Only a small fracture of their energy is utilized in displacement damage. Neutral particles are mainly responsible for displacement damage or displacement cascades.

A rate of the energy loss of the particle along the path normalized to the material density is called stopping power  $= \frac{1}{\rho} \frac{dE}{dx}$ , where  $\rho$  is the mass density of the target material,  $dE/dx$  is the rate of the energy loss  $dE$  along the path  $x$ .

Slowing down of a projectile ion due to the inelastic collisions with bound electrons in the matter is called electronic stopping. The energy loss per distance in this case is described by the Bethe-Bloch equation [9, 28, 29].

$$-\frac{dE}{dx} = \frac{4\pi z^2 e^4}{m_e v^2} N_e \left[ \ln \frac{2m_e v^2}{I(1-\beta^2)} - \beta^2 \right], \quad (2.1)$$

where  $z$  is the ion charge number,  $e$  is the electron charge,  $m_e$  is the electron rest mass,  $N_e$  is the electron concentration in the substance,  $v$  is the ion speed,  $\beta$  is the ratio of  $v$  to the speed of light  $c$ ,  $I$  is the ionizing potential.

Elastic collisions between the projectile ion and atoms in the sample are called nuclear stopping [9]. Nuclear stopping increases with the ion mass. At low energy, below 0.01 MeV nuclear stopping is usually larger than electronic stopping.

---

## 2.2 Gamma-ray damage effects

Gamma-rays deposit energy in the semiconductor components mainly by ionization [11]. The ionizing effect may be caused by X-rays, Ultra-Violet radiation or indirectly through secondary recoil particles as well [12-14]. Ionization of bulk material leads to: enhancement of conductivity through production of excess charge carriers, trapped charge, variation of electric and magnetic fields and chemical effects [11]. Photons interact with matter, depending on their energy in four ways [15]:

1. Photoelectric effect
2. The Compton Effect
3. Electron-positron pairs production
4. Nuclear photoabsorption

Photoelectric effect prevails for low energy photons, the Compton effect and pair production prevails for gammas with energies higher than 0.1-1 MeV depending on the Z number of target material. Nuclear photoabsorption has a peak in cross section at about 10-30 MeV depending on the Z number of target material.

Free electrons produced during ionization may span the forbidden gap and create electron-hole pairs if they have enough energy. This temporarily increases the conductivity of the bulk material. Electron-hole pairs, produced in non-conducting materials such as SiO<sub>2</sub> may play an even greater role in changing electronic properties of some components, e.g. transistors. Production of electron-hole pairs depends on two parameters: energy necessary to produce a pair and generation rate. Table 2.2 contains values of these parameters for silicon and silicon oxide [9]. The generation rate expresses the ionization capability of unit volume for the given material.

Table 2.2: The ionization energy and ionization-induced rate for silicon and silica.

Material	$E_{ion}$ [eV]	$g_0$ [electron-hole pairs·Gy <sup>-1</sup> ·cm <sup>-3</sup> ]
Silicon	3.6	4E15
Silicon Dioxide	18	8.2E14

Electron-hole pairs created in the target material may recombine or diffuse, depending on present electrical field. Charge deposited in silicon can provoke SEE (Single Event Effects), charge trapped in SiO<sub>2</sub> leads to changes of characteristics of components. Fig. 2.1 illustrates a process of charge generation in SiO<sub>2</sub>/Si interface due to gamma radiation.

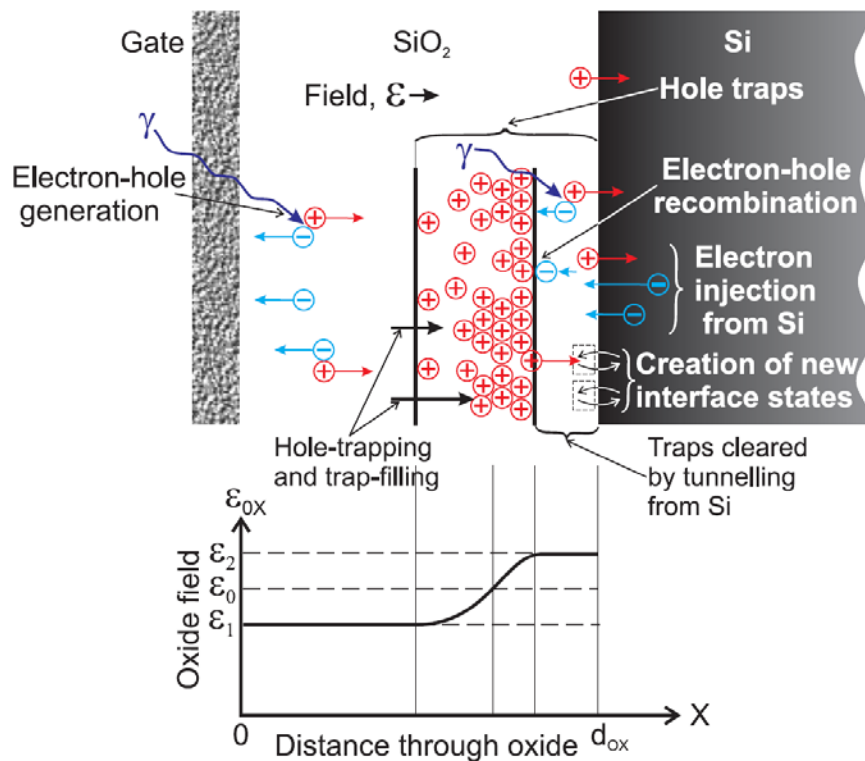


Fig. 2.1: The charge creation process in silicon dioxide, and SiO<sub>2</sub>/Si interface, disturbance of electric field [12].

---

Incident gamma creates electron-hole pairs in  $\text{SiO}_2$ . A fraction of created pairs quickly recombine. But mobility of electrons is much higher and electrons can leave silica instantaneously because of electric field presence as a part of normal circuit operation. Holes remaining in the insulator result in the charge built up in  $\text{SiO}_2$ . The amount of this charge depends on the electric field across the oxide, during the irradiation. Some of the positive traps may recombine due to tunneling effect, others stay trapped as electrically active defects. New interface states may be created with the rearrangement of atomic bonds at the  $\text{SiO}_2/\text{Si}$  interface [12]. The trapped charge has a significant effect on electrical properties of electronic components. Some of the generated traps, located in the nearest vicinity of  $\text{SiO}_2/\text{Si}$  interface may act as border traps or slow interface states. This effect plays an important role for sub-micron technologies when  $\text{SiO}_2$  thickness is less than 5-6 nm [16].



## 2.3 Degradation of MOS transistor parameters

The phenomena of charge build up in the SiO<sub>2</sub>/Si interface leads to changing of principal electrical parameters of MOS transistors. The most important is the threshold voltage  $V_{th}$ . Other effects of ionizing radiation on MOS structures are:

- an increase of leakage or dark currents
- a decrease of transconductance
- a reduction of drain-source breakdown voltage
- a deterioration of noise parameters
- a reduction of surface mobility
- an increase of the surface recombination velocity

**Threshold voltage shift  $\Delta V_{th}$**  induced by ionizing radiation may be expressed as a sum of two factors: holes trapped in silicon oxide  $Q_{ot}$  and interface states charge  $Q_{it}$ , see equation 2.2:

$$\Delta V_{th} = -e \frac{1}{C_{ox}} \Delta N_{ot} \pm e \frac{1}{C_{ox}} \Delta N_{it} \quad (2.2)$$

where  $e$  is the elementary charge,  $C_{ox}$  is the oxide capacitance expressed per unit area,  $\Delta N_{ot}$  and  $\Delta N_{it}$  are the densities of oxide-trapped charges and interface states, respectively. The voltage shift due to interface states is positive for PMOS (p-type metal oxide semiconductors) and negative for NMOS (n-type metal oxide semiconductors) [17]. Fig. 2.2 illustrates the threshold voltage shift process for PMOS.  $V_{th}$  shifts towards the negative gate voltage with absorbed dose. The typical influence of  $Q_{it}$  is illustrated as a dashed line on a characteristic curve.

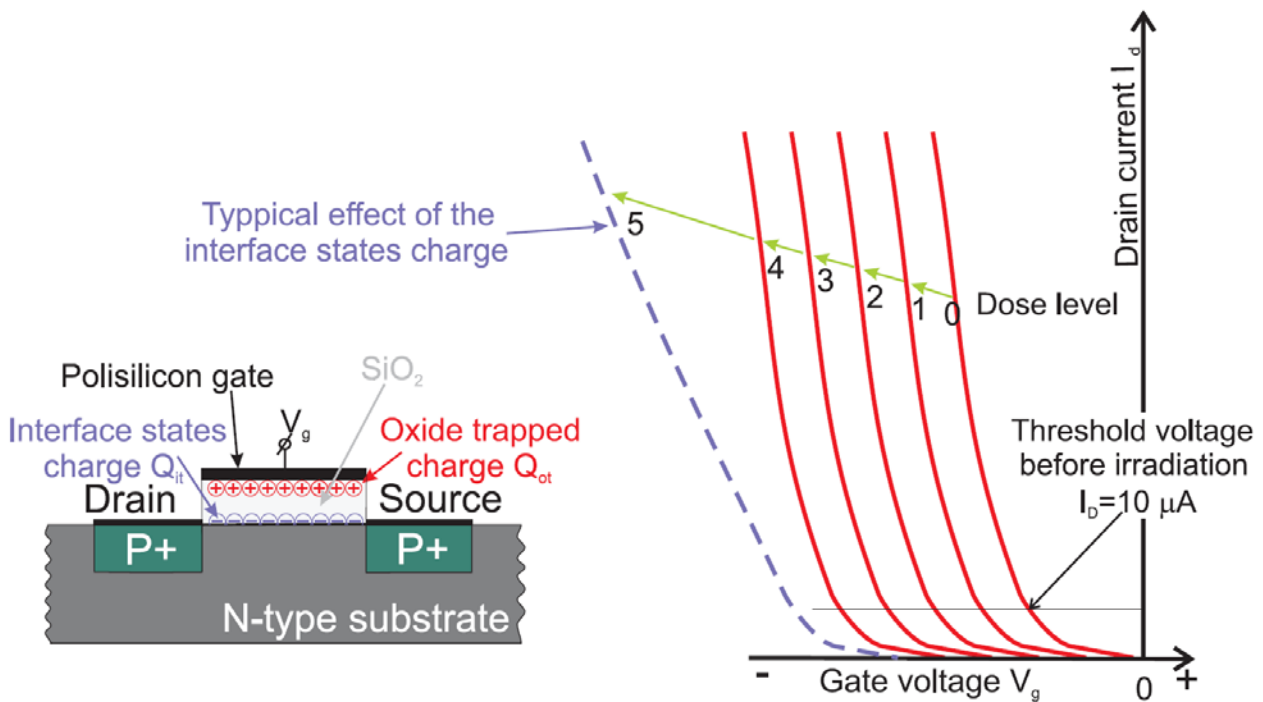


Fig. 2.2: Silicon oxide and interface trapped charges in PMOS transistor.  $I_D - V_G$  characteristic curve progression with dose. Dashed line shows typical influence of interface states charge [12].

In case of NMOS, threshold voltage may have both positive and negative shifts. Initially  $V_{th}$  will be decreasing as the  $Q_{ot}$  influence dominates. At some point enough charge will be accumulated in the silicon oxide, and the second effect can start predominating. This will lead to positive shifts of  $V_{th}$ .

Threshold voltage shift depends on the gate silicon dioxide thickness. Due to tunneling effect  $V_{th}$  shifts are significantly reduced, when SiO<sub>2</sub> layer thickness is less than 10 nm [18].

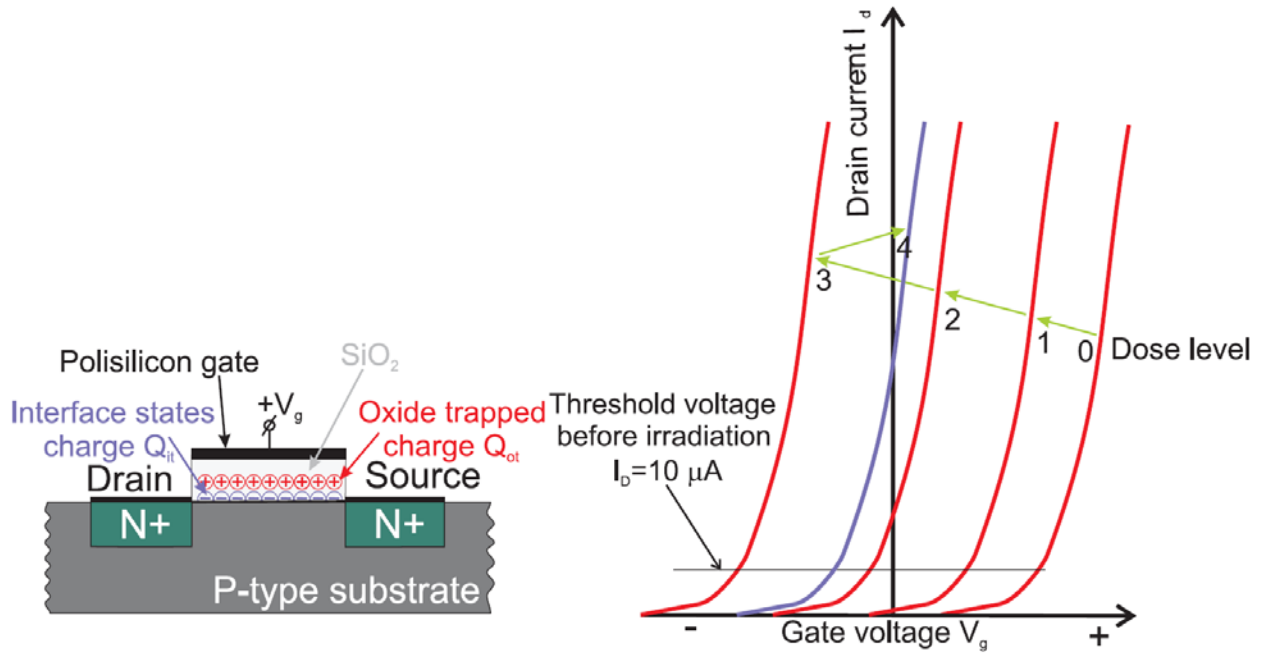


Fig. 2.3: Silicon oxide and interface trapped charges in NMOS transistor.  $I_D - V_G$  characteristic curve progression with dose [12].

### Decrease of transconductance

Charge trapped in silicon and silicon oxide reduces carriers' mobility in the transistor channel and thus leads to a decrease in its transconductance. This effect may be expressed using the following equation [19]:

$$\mu = \frac{\mu_0}{1 + \alpha_{it}\Delta N_{it} + \alpha_{ot}\Delta N_{ot}}, \quad (2.3)$$

where  $\alpha_{it}$  and  $\alpha_{ot}$  are the coefficients describing the effects of oxide-trapped charges and interface states, respectively,  $\Delta N_{ot}$  and  $\Delta N_{it}$  are the densities of oxide-trapped charges and interface states, respectively. The conductivity of the transistor reduces as well due to decrease of the carriers' mobility.

## An increase of quiescent or dark current

Silicon dioxide is often used as an insulation spacer for microchip fabrication. Radiation induced trapped charge and interface states may cause an increase of quiescent or dark current in the electronic element.

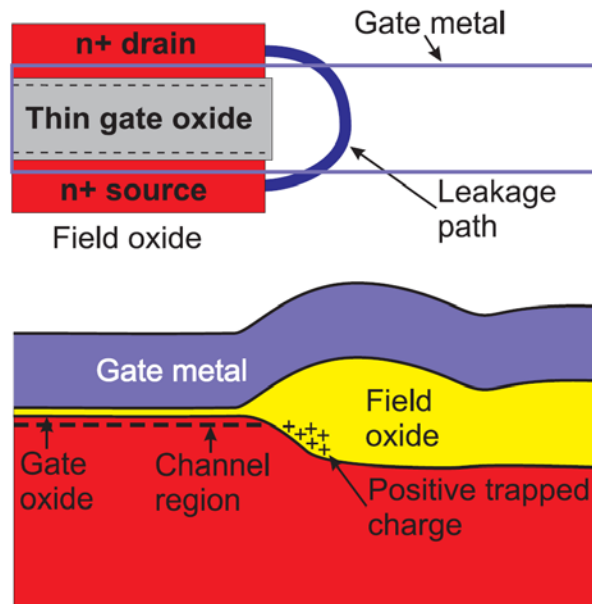


Fig. 2.4: The source-drain leakage path created by built-up charge in oxide [20].

This effect concerns CMOS, CCD, and bipolar devices using  $\text{SiO}_2$  isolation. Fig. 2.4 illustrates how build-up charge in lateral oxide structures results in creation of parasitic channel between drain and source of a NMOS transistor [18]. A constant current flow between the source and a drain can be observed after irradiation. A leakage between MOS transistors and other integrated structures is also possible due to this effect. Fig. 2.5 shows examples of quiescent current increase in CMOS devices with dose. As seen on the plot saturation is typical for such process. Submicron CMOS devices are especially vulnerable to this effect [21]. Junction breakdown voltage is altered during this process and multiguard structures are used to improve reliability of certain devices [22].

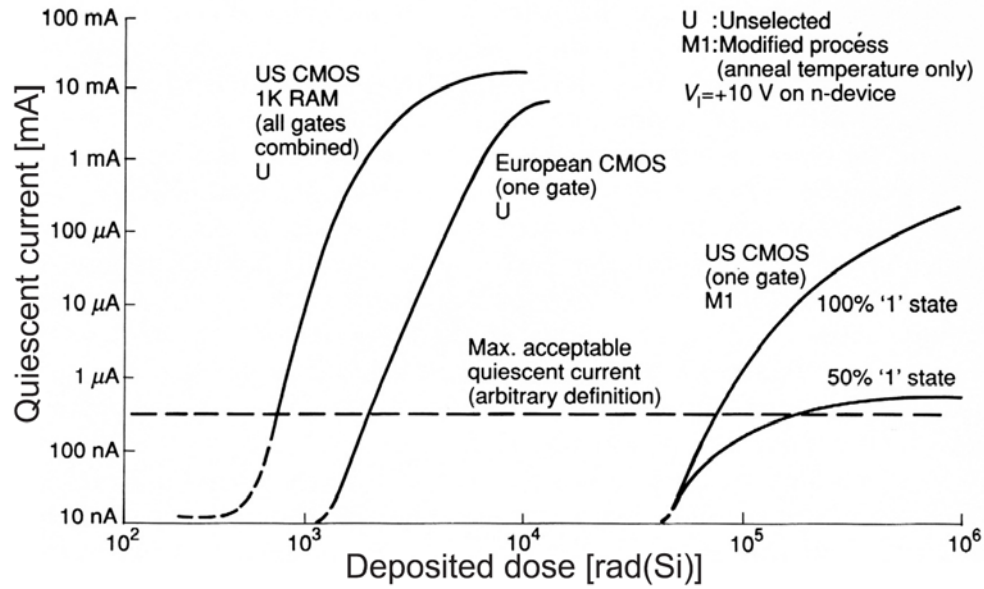


Fig. 2.5: An increase of a quiescent current as a function of absorbed dose of CMOS devices [12].

## Noise increase

It was confirmed that noise level, in particular  $1/f$  noise or pink noise is increasing with total ionizing dose [18, 23]. The reason is the same - trapped  $\text{SiO}_2$  and interface charges. Fig. 2.6 shows noise increase for a  $3 \mu\text{m}$  technology device with 48 nm oxide layer. The gate voltage was biased with 6V during the exposure. High peaks on the spectrum are caused by fundamental and higher harmonics of the power line.

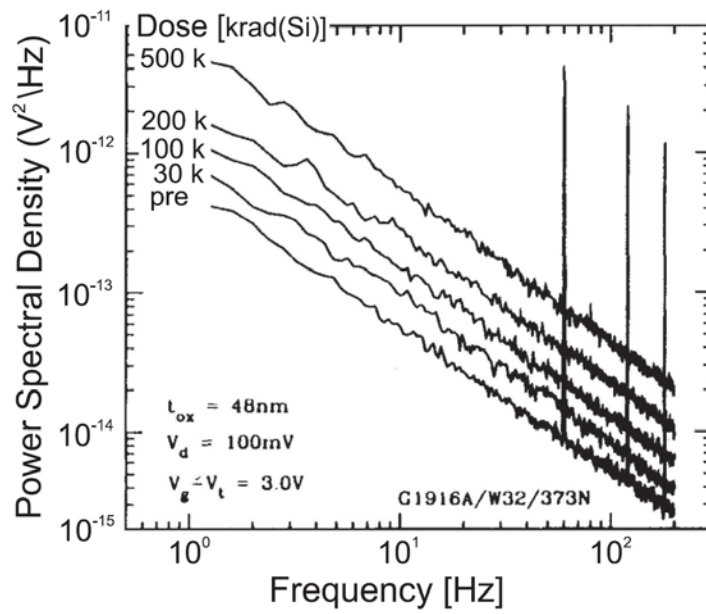


Fig. 2.6:  $1/f$  noise spectra as a function of total ionizing for W32 (G1916A) wafer [23].

---

## 2.4 Neutron damage effects

Neutrons interact with matter in several different ways:

- elastic scattering
- inelastic scattering
- capture process (n, $\gamma$ )
- nuclear reactions: (n,p), (n, $\alpha$ ), (n,2n), (n,f)

Scattering processes and nuclear reactions are dominating for fast neutrons ( $E > 1\text{MeV}$ ) and capture effect is more probable for slow neutrons [9].

In a case, when the target material has a lattice structure, an atomic displacement with lattice damage may take place, because of neutron bombardment. This effect may be compared to a classical collision between two balls. If the transferred energy is higher than the displacement energy  $E_d$ , the lattice atom will be removed from its original position. A defect will be created. The recoil atom may displace other atoms or produce electron-hole pairs depending on the energy. Cascades of disruptions in the silicon lattice are observed for highly energetic particles.

Fig. 2.7 illustrates different types of displacement effects: vacancy, divacancy, interstitial displacement, Schottky and Frenkel defects. Vacancies, Frenkel defects and interstitial displacements are more likely to appear [9]. Primary effects are usually unstable at room or higher temperatures. They normally migrate, annihilate or create more complex secondary effects. Impurities and doping atoms in semiconductor become a basis for permanent cluster effects at room temperature [26]. Permanent defect clusters act as charge trapping centers and increase the resistivity of the material [11]. Mobile vacancies play a role of recombination point for minority carriers and reduce their lifetime. Defects that act

like hole traps are called H defects and defects responsible for electron trapping are called E defects [9]. Displacement damage affects electrical characteristics of electronic components mainly by changing structure of semiconductor substrates.

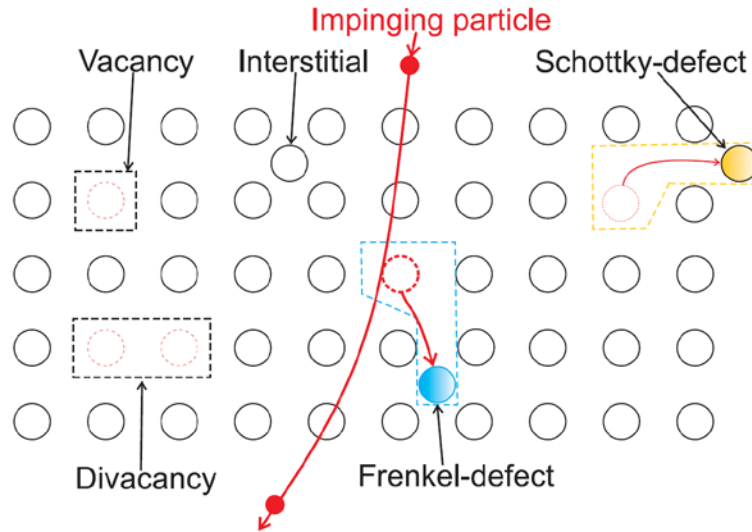


Fig. 2.7: Various defects created due to atomic displacement in lattice [9].

Even being uncharged particles neutrons may ionize atoms (Fig. 2.8):

- by collision and production of recoil elements
- by production of gamma rays through the de-excitation process of excited atomic nuclei
- by collisions followed by absorption of neutron by target nucleus

Neutrons may initiate the following nuclear reactions:  $(n,p)$ ,  $(n,\alpha)$ ,  $(n,2n)$ ,  $(n,f)$ . A charged particle may be produced as a result of such reaction, for example:  $\text{He}^3(n,p)\text{H}^3$ ,  $\text{B}^{10}(n,\alpha)\text{Li}^7$  [19]. Resulting particles, e.g. alpha particle may have high LET (Linear Energy Transfer). Besides that, alpha and heavier particles have a short range in silicon and the resulting ionization may be very significant.

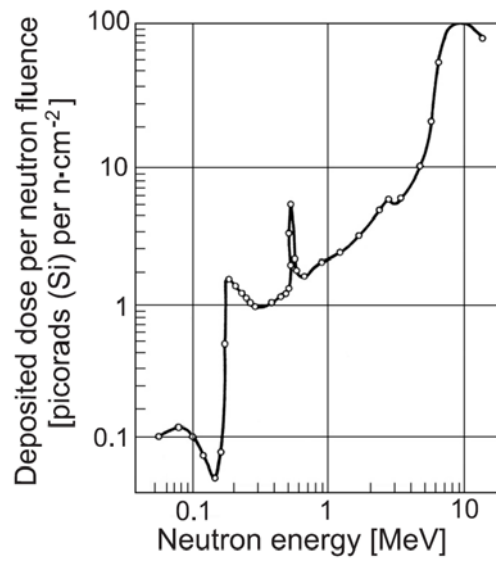


Fig. 2.8: Experimental data for neutron-induced ionization in silicon [11].



---

## 2.5 Single Event Effects

Ionization in sensitive areas of electronic devices may lead to so called SEEs (Single Event Effects). The energy  $dE/dx$  transferred from the ionizing species to matter is called LET (Linear Energy Transfer). This value is expressed in  $\text{MeV}\cdot\mu\text{m}^{-1}$  or  $\text{MeV}\cdot\text{cm}^2\cdot\text{g}^{-1}$  when it's normalized to the specific mass of the absorbing material. LET is dependent on the incident particle type, energy and absorbing material and may be calculated using Bethe-Bloch equation [9, 28, 29], see 2.1. Critical LET or  $\text{LET}_{\text{th}}$  (LET threshold) is the minimum LET value deposited in the electronic element for which SEE is observed. Corresponding charge necessary to create a SEE in the electronic element is called critical charge [30]. The value of this charge strongly depends on the feature size (Fig. 2.9).

SEEs are divided into two groups:

- non-destructive, when the device failure can be recovered by the system reset or reprocessing of affected data
- destructive or hard errors, when the failure leads to permanent damage of the device or the system

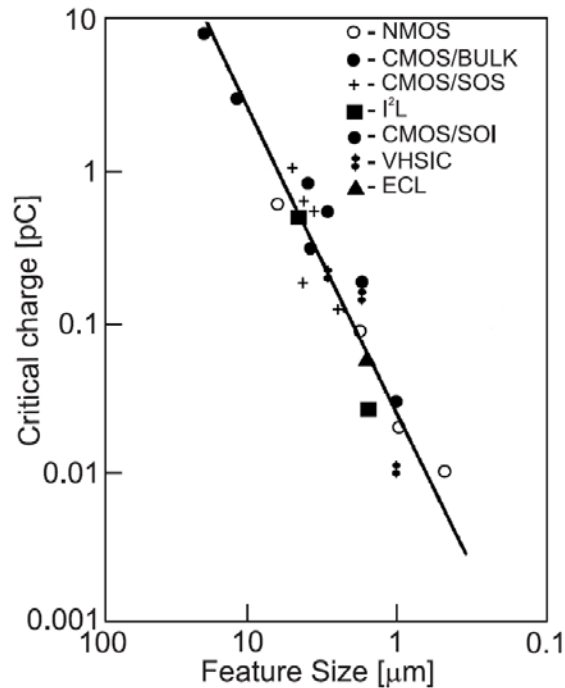


Fig. 2.9: Critical charge plotted as a function of the feature size for different technologies [9].

### 2.5.1 Non-destructive effects

**Single Event Upset (SEU)** is a change of the logic state of an electronic element due to charge production during ionization. SEUs affect mainly digital devices, e.g. microprocessors, FPGAs (Field Programmable Gate Arrays), memories. This phenomenon affects both bipolar and MOS technologies. Charged particles can ionize the sensitive volume of the element directly [31]. Neutral particles can generate SEEs through the secondary ionizing particles, which are born during interaction of neutral particle with absorbing material. Most of the neutral particles pass through silicon, but a few interact with nuclei and produce ionizing particles: alpha particles, protons or heavy ions (Fig. 2.10). High-LET particles deposit all the energy along a short path and in a small radius (typically 1 μm). When this happens near the sensitive node of the device, e.g. drain of a MOS

transistor, a spike of the drain current is observed. The induced current pulse may be hundreds of mA and lasts for nanoseconds. If the corresponding charge is higher, than critical charge – SEU takes place.

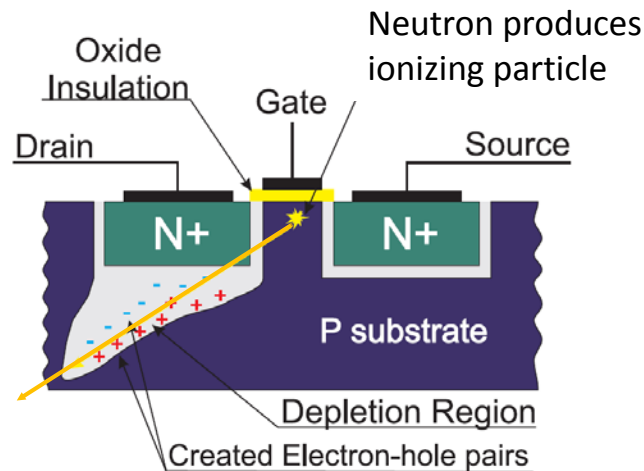


Fig. 2.10: Ionizing particle is created inside the sensitive volume of MOS transistor. SEU takes place due to ionization if the ionization charge is higher than critical.

**Single Event Functional Interrupt (SEFI)** is a subgroup of SEU effects that happens in high-density programmable devices, like CPLDs or FPGAs. SEFI usually causes logical mistake and results in malfunction of system operation. A reset of the device is needed to normalize its operation in case SEFI happens [35, 36].

**Single Event Transient (SET)** is a subgroup of SEE when the ionizing particle causes one or more voltage pulses (i.e. glitches) to propagate through the circuit. SET does not always result in a change of logical state until it propagates through digital circuitry and results in an incorrect value being latched in a sequential logic unit. Otherwise it causes distortion in analogue output signal [37,

38]. SET is harder to register and to correct than SEU. Techniques for SET correction are still under research [39-42]. This effect varies significantly with the device parameters: fabrication technology, current pulse amplitude, operation frequency. Modern technologies are becoming more vulnerable to SET, because of increasing frequency of operations and decreasing feature size. One particle may trigger multiple SETs in high density electronic components. Fig. 2.11 shows an example of SET triggering in the LM139 comparator with different loads. SETs are generated using a 815 nm laser. The comparator was supplied with 5V and the differential input was equal to +100 mV [43].

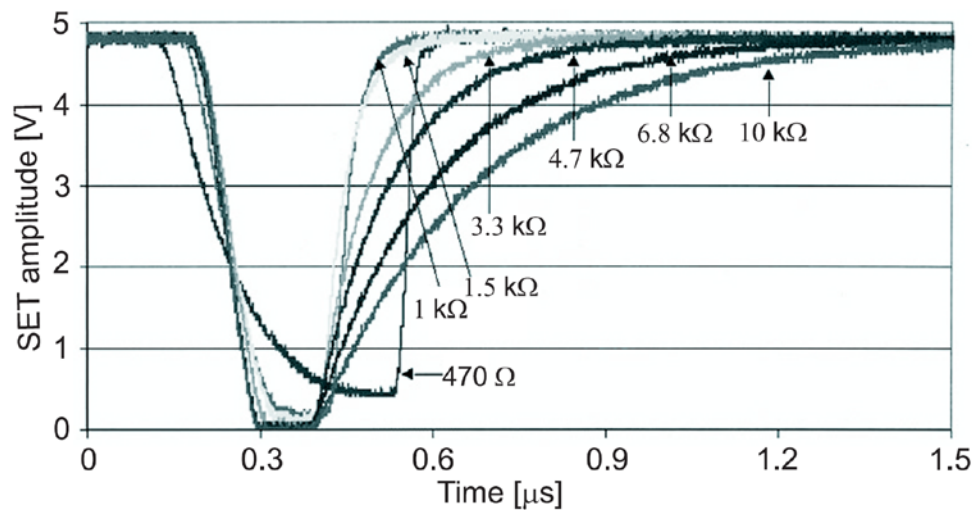


Fig. 2.11: SETs observed in LM139 comparator excited with 815 nm laser [43].

### 2.5.2 Destructive effects

**Single Event Latch-up (SEL)** usually happens in CMOS-based devices and is a potentially destructive event. CMOS integrated circuits consist of NMOS and PMOS transistors. Two parasitic lateral bipolar transistors are present between PMOS and NMOS integrated transistors: n-p-n and p-n-p (Fig. 2.12). They may be considered as a parasitic thyristor structure pnpn or npnp. This thyristor is disabled during normal operation due to reverse-biased well-substrate junctions – there is no

current flow between the thyristor and the cathode. The thyristor may be activated when all of the following conditions are fulfilled:

1. The gain product of parasitic transistors  $\beta_{npn} \cdot \beta_{pnp}$  must be greater than 1.
2. Enough charge must be injected into base-emitter junctions of parasitic transistors
3. Power supply must provide enough power to maintain the latch process

In case of thyristor activation, a high current will flow through the low-impedance patch and the component will be locally overheated. This situation is called SEL and may lead to thermal destruction of the component. To prevent the device from damage the power supply must be stopped disabling the parasitic thyristor. SEL probability is strongly dependent on the channel length and the epitaxial layer thickness of CMOS integrated circuits. Therefore newer technologies are more sensitive to SEL [45].

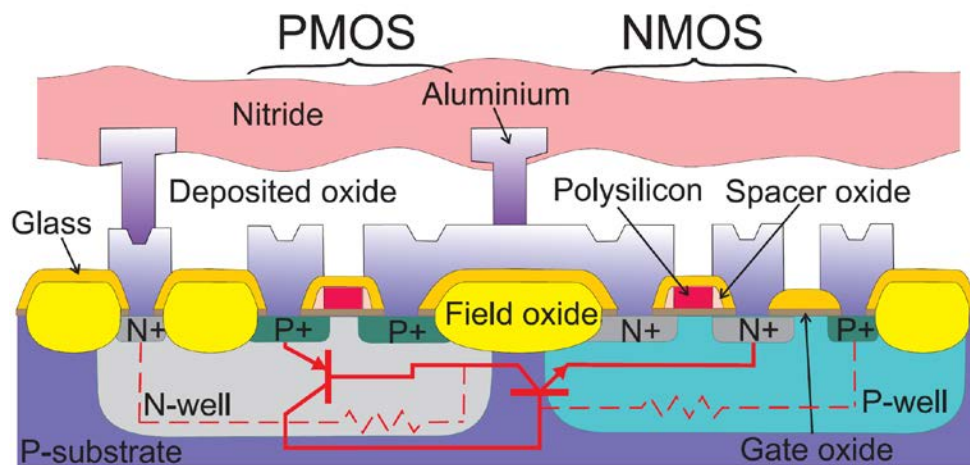


Fig. 2.12: Diagram of CMOS inverter. Parasitic thyristor is illustrated in the bottom part of the image [44].

**Single Event Burnout (SEB)** happens mainly in high-power MOS transistors, like VDMOS or DMOS. If the ionizing particle passes through a volume of parasitic

bipolar transistor in VDMOS a large current density in range of  $10^4 \text{ A}\cdot\text{cm}^2$  will be generated in the presence of the high drain-source voltage (Fig. 2.13) [46, 47]. When the voltage is applied to the base-emitter junction of the inherent parasitic bipolar transistor, the transistor may be turned on due to the avalanche multiplication of the BJT (Bipolar Junction Transistor) collector current. Junction may overheat and device burnout may happen if local power density is large enough.

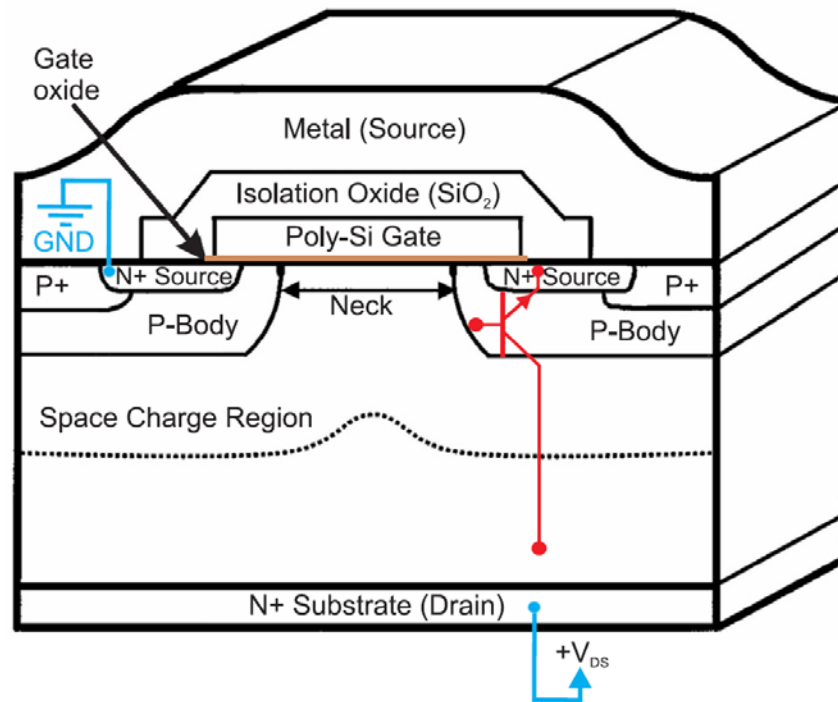


Fig. 2.13: The cross-section of the VDMOS transistor [48].

**Single Event Gate Rupture (SEGR)** is a dielectric breakdown caused by ionizing particle [49]. Electron-hole pairs produced by the ionizing particle are divided by the electric field towards the gate and the drain. Positive charge, collected near the Si/SiO<sub>2</sub> interface increases the electric field in the gate oxide. The leakage current also increases. If the transient disturbance is large enough a significant charge collected in the gate oxide will be discharged. This will lead to

local temperature increase and possible destruction of the oxide in the nearest vicinity [9, 48]. SEGR is typical for non-volatile memories, like EEPROMs, it happens during write or erase procedures when a relatively high voltage is applied to transistors gates.

**Single Event Snapback (SES)** affects mainly NMOS transistors. This effect is similar to SEL. The inherent parasitic bipolar transistor may be turned on if the incident particle has high LET (Fig. 2.14). Contrary to SEL, reduction of main supply voltage of the circuit is not necessary to recover its operation. It may be done by sequencing electrical signals. SES may be destructive when the local current density is high enough to cause critical overheating. SOI (Silicon-on-insulator) technology is much more resistant to SES than CMOS [50,51].

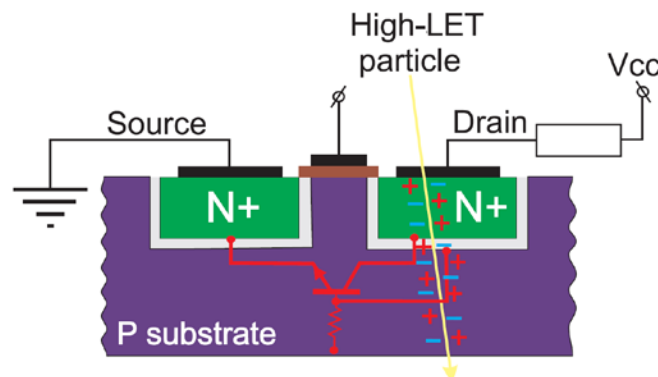


Fig. 2.14: The inherent bipolar transistor of NMOS structure affected by high-LET particle [35].



---

## 3. Simulations

---

### 3.1 FLUKA Monte Carlo Tool

FLUKA is a tool for calculations of particle transport and interaction with matter [52-54]. It covers a wide range of applications: target design, detector design, calorimetry, activation, dosimetry, shielding design, cosmic rays, neutrino physics, radiotherapy etc.

This tool can simulate with high accuracy the interaction and propagation in matter of about 60 different particles, including photons and electrons from 1 keV to thousands of TeV, neutrinos, muons of any energy, hadrons of energies up to 20 TeV. Time evolution and tracking of emitted radiation from unstable residual nuclei can be performed online.

FLUKA can handle even very complex geometries, using an improved version of the well-known Combinatorial Geometry (CG) package. The FLUKA CG has been designed to track correctly also charged particles (even in the presence of magnetic or electric fields). Various visualization and debugging tools are also available.

There is an advanced user-friendly interface for FLUKA – FLAIR [55]. The philosophy of the FLAIR interface was to work on an intermediate level. Not too high, that hides the inner functionality of FLUKA from the user, and not so low that the user is in constant need of the FLUKA manual to verify the options for each card. It has many useful features:

1. input editor front-end interface for an easy and almost error free editing as well as validation of the input file during editing;

- 
2. interactive geometry editor, allowing to edit bodies and regions in a visual/graphical way with immediate debugging information;
  3. advanced layer mechanism for graphically displaying any information from the input file on top of the geometry:
    - lattices and voxel display 2D and 3D
    - density, biasing, thresholds, ...
    - technical drawing superposition
    - interactive USRBIN plotting and surface mapping
    - real-time 3D ray tracing rendering, with shadows, edges, clipping and projection bodies
    - customizable multiple palettes
  4. debugging, compiling, running and monitoring of the status during a run;
  5. back-end interface for post-processing of the output files and plot generation through an interface with gnuplot and 3D photo-realistic images;
  6. materials library and geometrical objects, for easier editing, storing and sharing among other users and projects;
  7. python API for manipulating the input files, post processing of the results and interfacing to gnuplot;
  8. import/export to various formats:
    - MCNP
    - GDML
    - Povray
    - DXF
    - bitmap images

---

## 3.2 Monte Carlo Simulations

It was necessary to estimate prompt dose distribution in the upcoming experiments in order to prepare installations correctly. FLUKA code was chosen for this purpose as the best fitting tool. Each irradiation experiment setup was prepared with concern of corresponding calculations.

The simulation process begins with modeling the geometry of the experimental conditions. It consists of bodies made from different materials and compounds. Normally it is a target, air and material samples around the target and a beam dump. Then a beam type, position, size, shape, and direction are set. Finally one has to define virtual detectors of different kinds. These may be particle tracking detectors, energy deposition detectors, equivalent dose detectors and so on. Calculation process usually takes several hours to get required statistics and accuracy. After the calculation process is finished the output files are generated. They contain all information scored by virtual detectors, defined earlier. All the results are usually calculated per primary particle, and should be later normalized to actual number of particles in the experiment.

FLUKA calculations help to understand particle composition in the secondary radiation better. The preliminary calculations of doses are also very important. Of course the reliability of Monte Carlo calculations is always an issue. The agreement of the calculation results with the experiment may be checked after the irradiation by comparing the dosimeters readings with Monte Carlo energy deposition detector (Table. 3.1). Position A is a position on the camera. And position B is a complementary reference point (~1 m form the target). These results show, that FLUKA results may be trusted for this and similar situations with inaccuracy of 1/3 or less. Statistical error may always be reduced to at least 10 times lower level.

Table 3.1: Total dose in vicinity of 0.95GeV/u Uranium beam losses

Type of data	Position	Dose	Percent of experiment data
Monte Carlo (FLUKA)	A	61.1 Gy	86%
Experiment (Alanine Dosimeter)	A	71.4 Gy	100%
Monte Carlo (FLUKA)	B	11.5 Gy	75%
Experiment (Alanine Dosimeter)	B	15.3 Gy	100%

Fig. 3.1 shows results of particle flux detectors. Uranium beam of energy 0.95 GeV/u comes from the top and hits the Aluminum target. Target is a cylinder (coordinates 0,0). Bottom part is an iron beam dump with cylindrical entrance channel. As can be seen from the Fig. 3.1 a, b and c, the number of neutrons is about 100 times higher than protons. Number of gammas is comparable with neutrons. Moreover a typical space distribution may be noticed. It is forward directional for neutrons and protons, but for gammas it is almost isotropic.

It is also possible to calculate energy deposition or prompt dose for each type of particle separately. Fig. 3.2 shows the prompt doses in the same experiment. It is clear, that the most of the energy is deposited by protons. There are also heavy fragments like alpha particles, but their number is small. Fig. 3.2 d shows the total prompt dose. One may notice strange circular patterns. It appeared that it was a contribution from electrons and the circular nature was a code bug, which was reported. Nevertheless it did not interfere the results in a significant way. After completing the total prompt dose simulation results with experimental results we obtain a useful reference. It allows predicting device behavior in similar radiation environment, based on Monte Carlo calculations for each certain area.

Simulation of SIS18 tunnel beam losses was performed as part of this work. Fig. 3.3 shows a resulting prompt dose. The beam is going along the beam line and hits an iron magnet form inside at a small angle. There is air outside the magnet

---

and concrete walls are covering the tunnel. The red ellipse shows a position, where radiation sensitive equipment is located. The dose is about 1000 times lower, than in the ellipse in Fig. 3.2 d. It allows us to make estimates of device reliability and lifetime, based on experimental data from the study.

Another simulation for radiation protection and shielding design purposes was performed. It is the APPA building (bld. 50), one of the components of FAIR. 2.0 GeV/u Uranium beam is going along the beam line and is lost at 3 points, on the top part of the image – 3%, in the middle – 47% (target), and in the bottom – 50% (beam dump). The experimental hall is heavily shielded with 4-7 meters of concrete. The dose inside the hall is rather high and is compared to what we had in the experiments described above. Installation of equipment is not recommended in such conditions. A special area was designed with additional shielding inside this hall – the red oval in Fig. 3.5. The dose inside this area is already about  $10^4$  times lower, and conditions are more acceptable for radiation sensitive equipment. Another point of interest is located above the experimental hall, where a lot of equipment will be located, see the white oval in Fig. 3.4. The dose is already  $10^7$  times lower, therefore conditions are excellent.

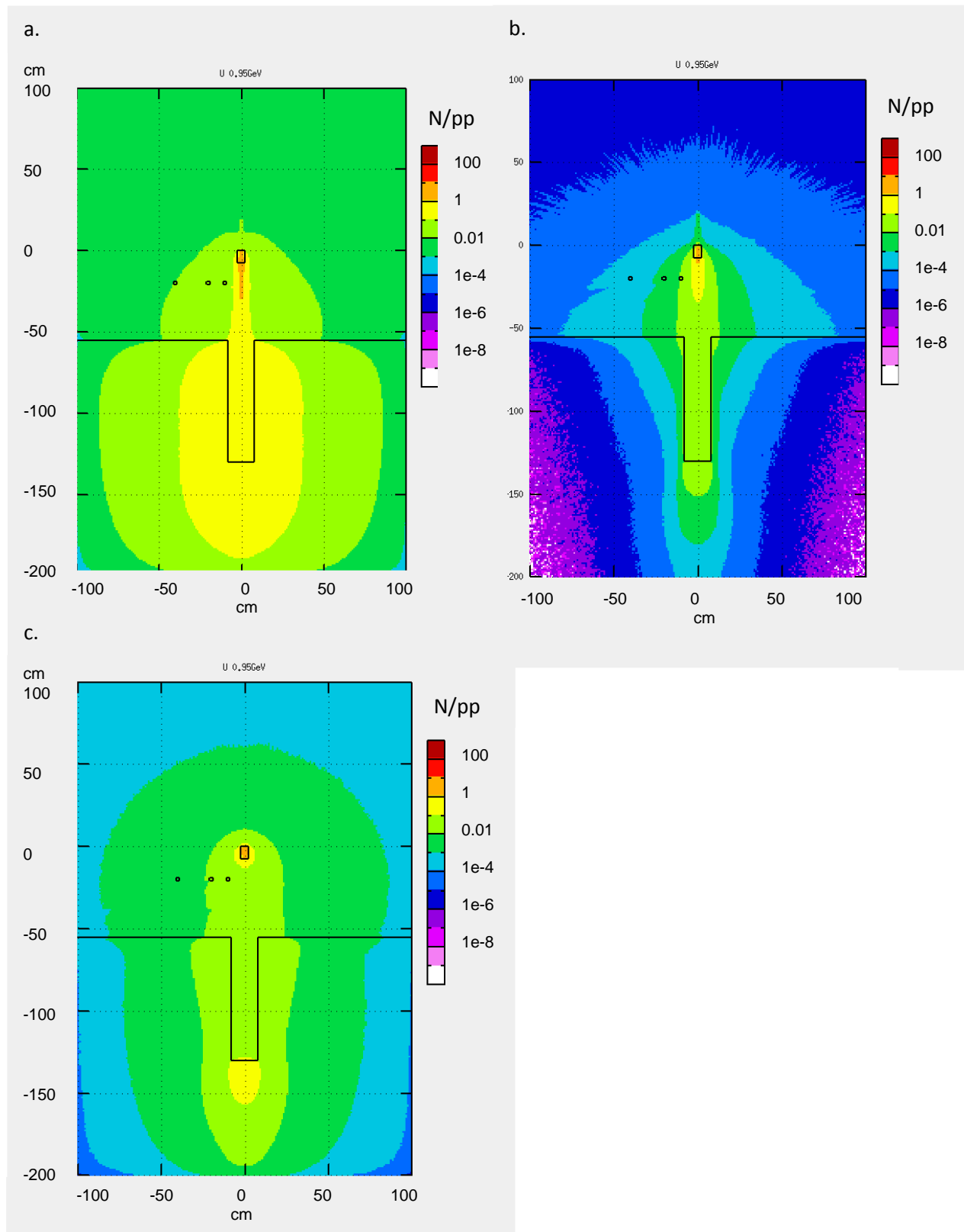


Fig. 3.1: Particle flux detectors (number of particle tracks per primary ion), a. - neutron, b. - proton, c. – gamma. Irradiation of Aluminum target with Uranium 0.95 GeV/u heavy ions.

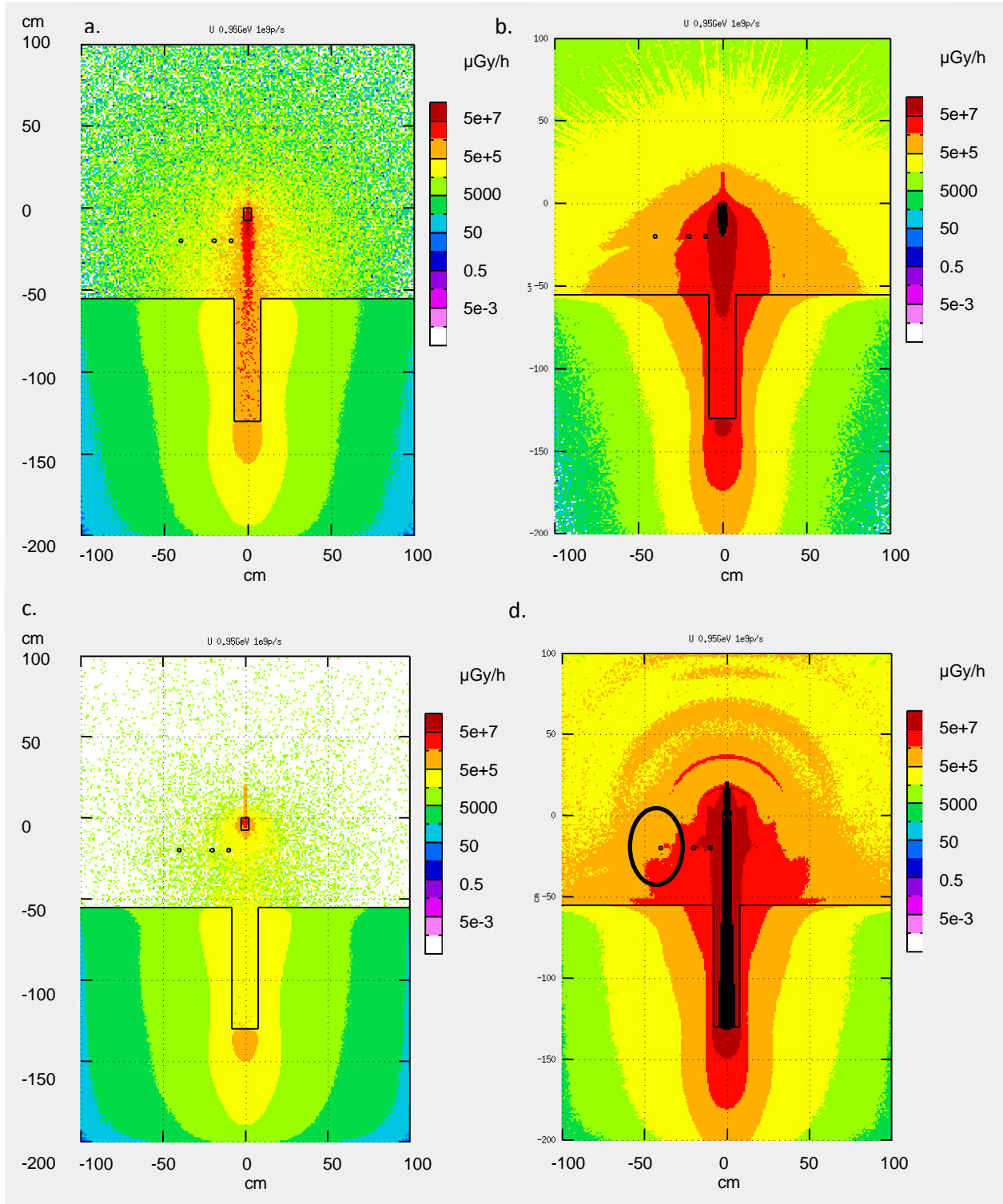


Fig. 3.2: Prompt dose detectors (Gy per hour), a. - neutron, b. - proton, c. – gamma, d. – overall. Irradiation of Aluminum target with Uranium 0.95 GeV/u heavy ions,  $1e9$  particles/s.

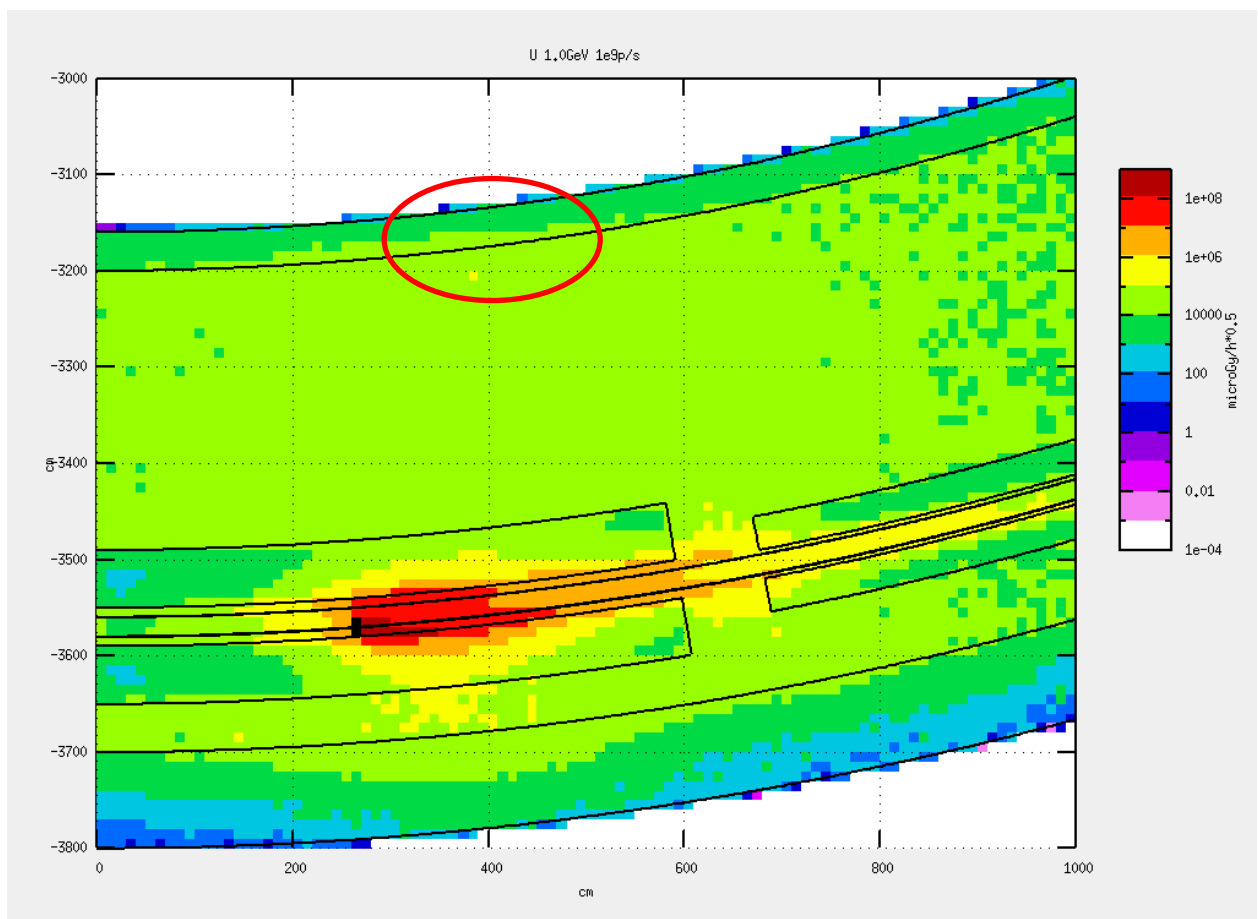


Fig. 3.3: Prompt dose detectors. Part of SIS18 tunnel, 100% beam losses in iron magnet 0.95 GeV/u Uranium heavy ions, 1e9 particles/s.

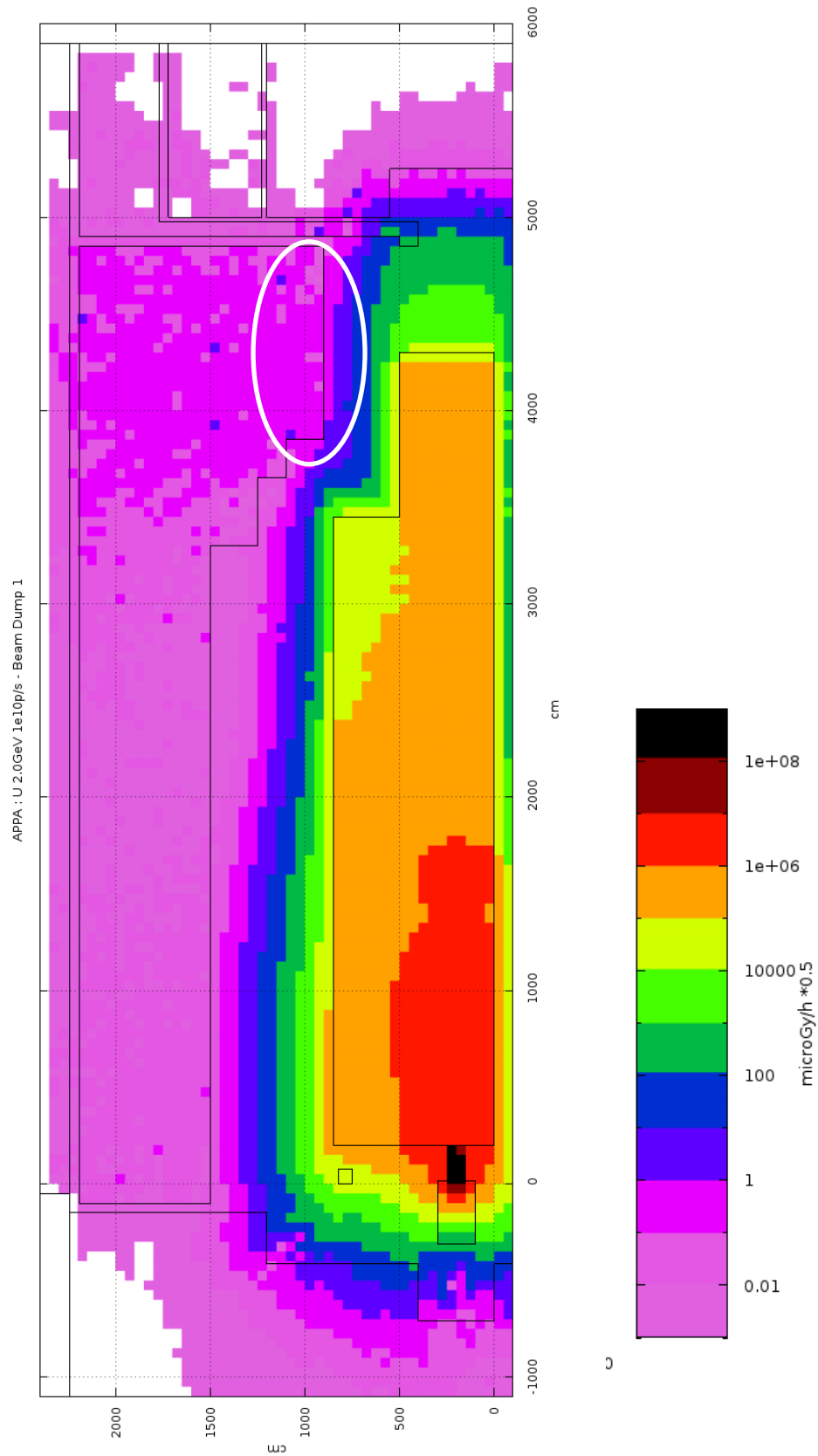


Fig. 3.4: Prompt dose detectors. FAIR APPA hall, 3%, 47%, 50% beam losses along the beam line. 2.0 GeV/u Uranium heavy ions, 1e10 particles/s.

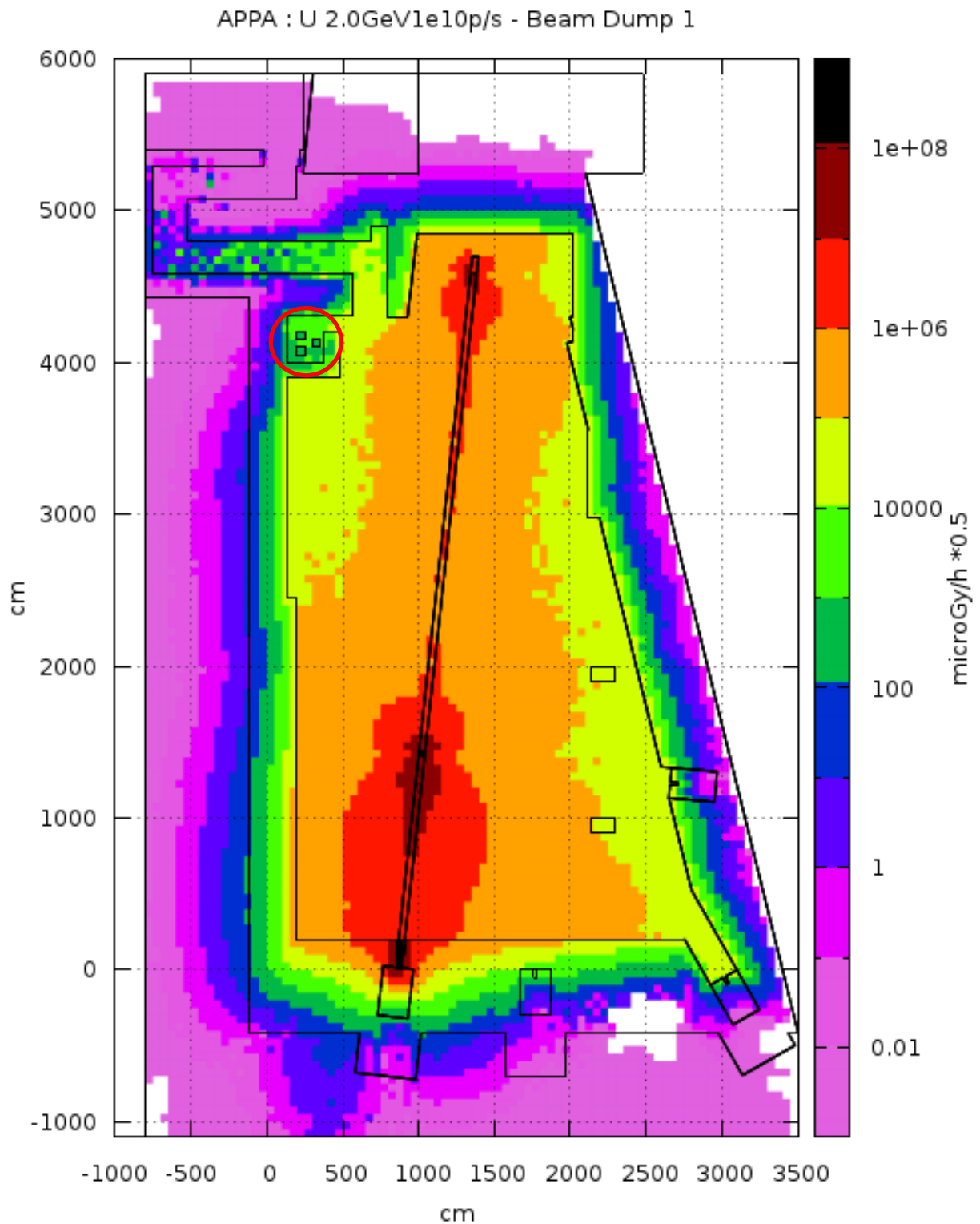


Fig. 3.5: Prompt dose detectors. FAIR APPA hall, 3%, 47%, 50% beam losses along the beam line. 2.0 GeV/u Uranium heavy ions, 1e10 particles/s.

# 4. Experimental methods

## 4.1 Beams

All experiments were performed at GSI behind the SIS18 synchrotron (Fig. 4.1). It provides heavy ion beams of different species with energies up to  $\sim 1$  GeV/u. The heaviest ion species used was U, the lightest was Na. The synchrotron is able to operate in fast extraction and slow extraction modes. In the first regime the beam is extracted with a pulse length of 200-300 ns and a repetition rate of about 2-3 s. The shortest pulse in slow extraction is 200-300 ms with a repetition rate of a few seconds. The long pulse may reach minutes, but has a disadvantage of low intensity. The beam pulses extracted from SIS18 are often also called beam spills.

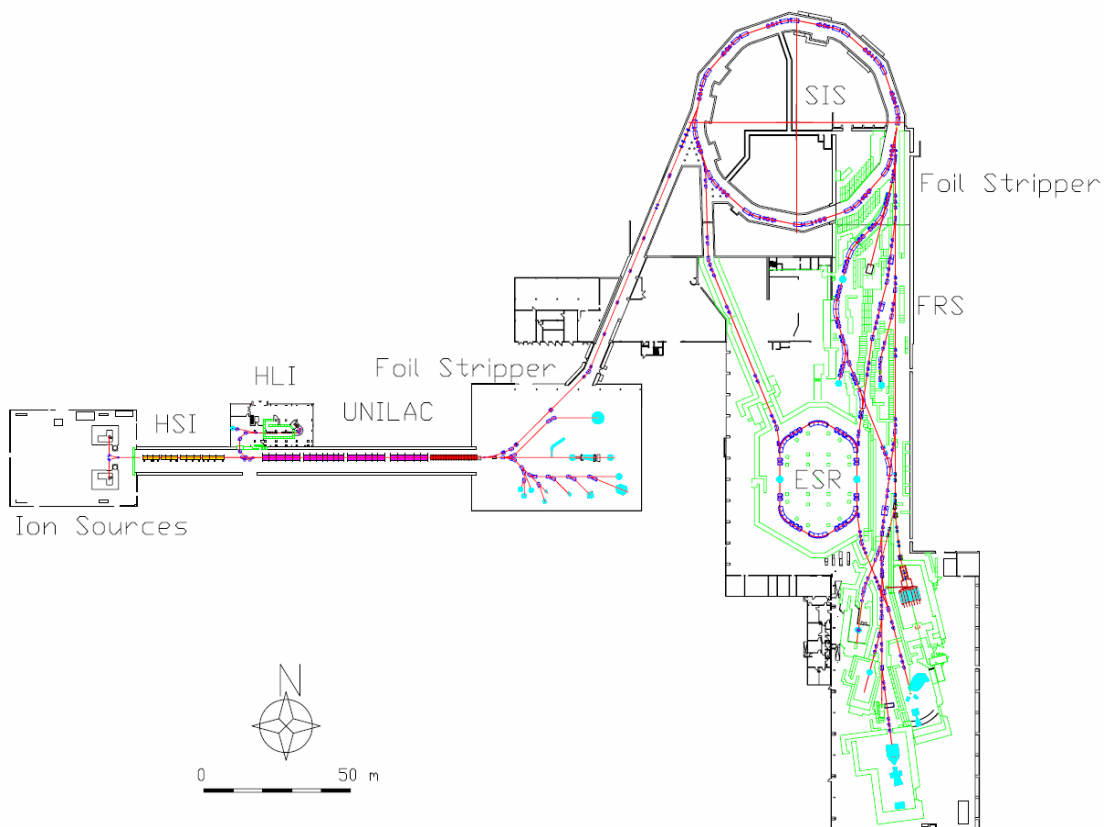


Fig. 4.1: GSI, accelerators and beam lines.

---

In most experiments we gave preference to fast extraction mode, which allows obtaining highest intensity and reducing experimental data processing complexity. Initial energy of the beam is defined by synchrotron settings. Intensity of the beam is measured before the exit window by a current transformer, which has about 3% uncertainty [56]. The beam cross section was diagnosed by grid beam profile-meter and was approximately Gaussian. Beam spot size was less than 3 cm in vertical and horizontal planes. It was confirmed both on profile-meter, and scintillating target, mounted for calibration on a moving platform behind the exit window.

---

## 4.2 Target and device setup

All irradiations took place in HHD experimental cave at GSI. There are two main reasons for this choice. The first is that this cave has the shortest transfer line from SIS ring, that means minimum intensity losses during beam transfer and fastest beam alignment, which is important for short shifts. The second is proper shielding, designed for high intensities and possible high activation of materials. Besides that most experiments, described in this work, were performed as parasitic along with primary experiments of metal target activation [57-58].

In HHD vacuum beam pipe is ending with a steel screen. 2x2x3 m beam dump with a 20 cm diameter entrance channel is located about 2 meters downstream. The experimental setup was located within these 2 meters (Fig. 4.2). For each experiment some parts of setup were installed and uninstalled (Fig. 4.3).

Two moving platforms allowed us to manipulate targets and device positions in horizontal plane. Metal targets for primary beam, scintillator screen for beam positioning, transistor chips and CCD cameras were attached to these platforms with holders. Ethernet switch HP ProCurve 2520G-24-PoE was located under the axis of beam direction at 50 cm from the axis and 50 cm downstream from primary metal target. An n-type transistor chip was mounted on the rear platform so that it may be irradiated directly with heavy ion beam. Digital CCD camera Basler scA640-74gm was mounted on beam line height on the rear platform so that it could be moved in three different positions (Fig. 4.4). Analogue CCD camera CONRAD 420 TVL was mounted on the same holder afterwards for direct ion beam irradiation.

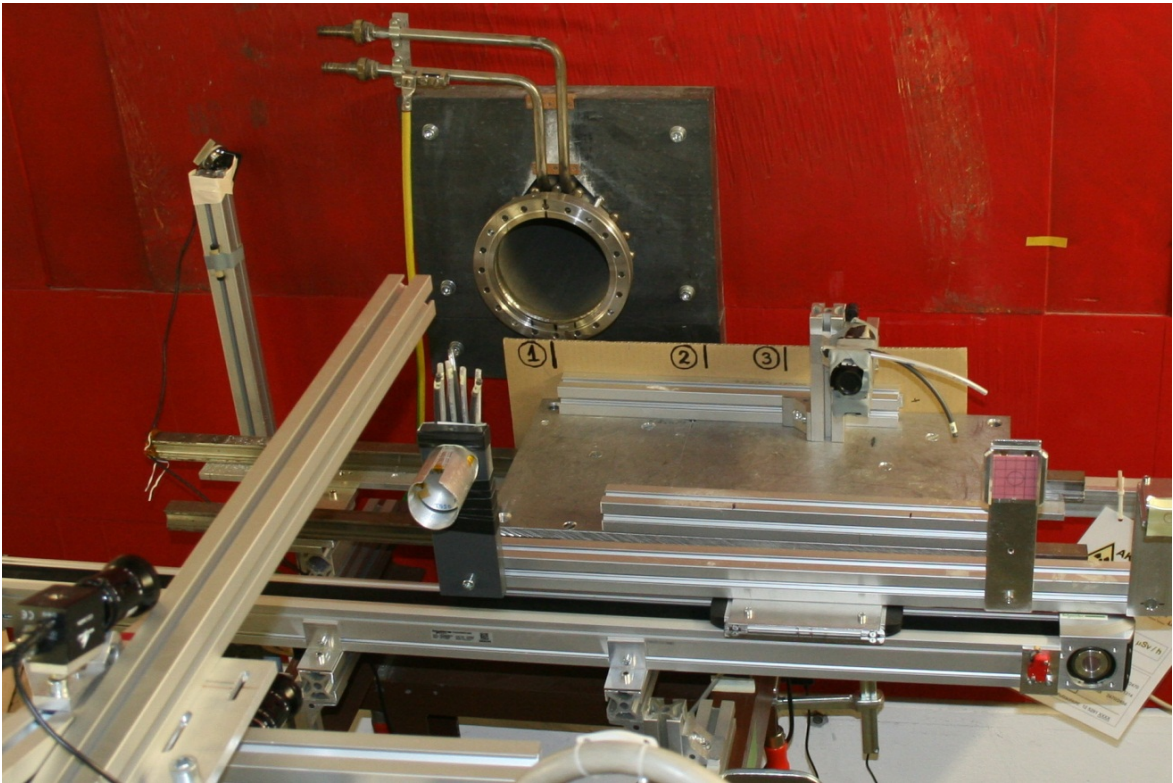


Fig. 4.2: Experimental setup in the HHD cave.

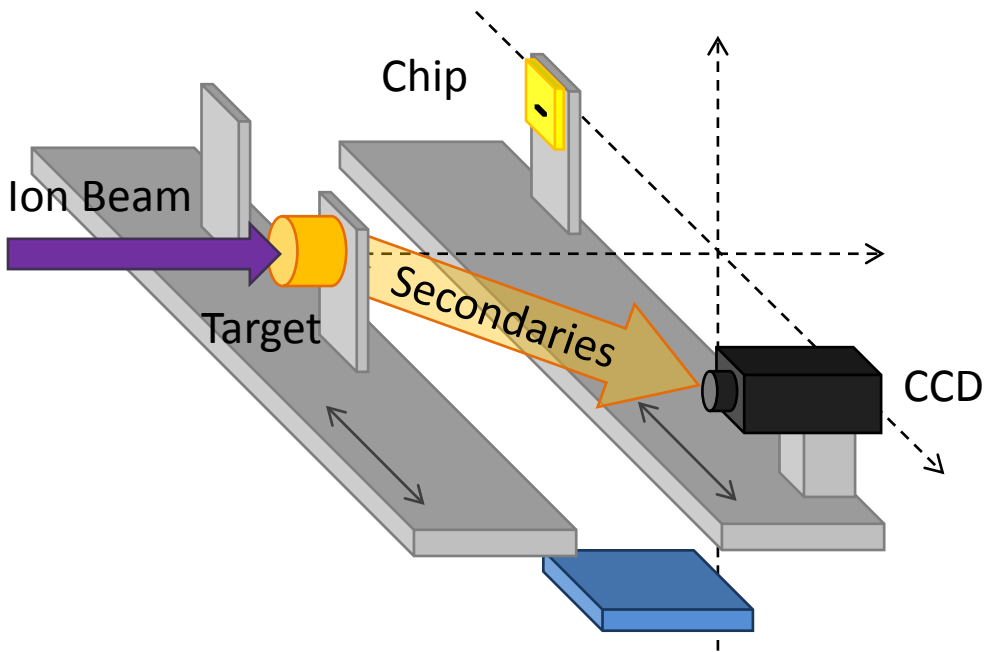


Fig. 4.3: Schematic of the experimental setup.

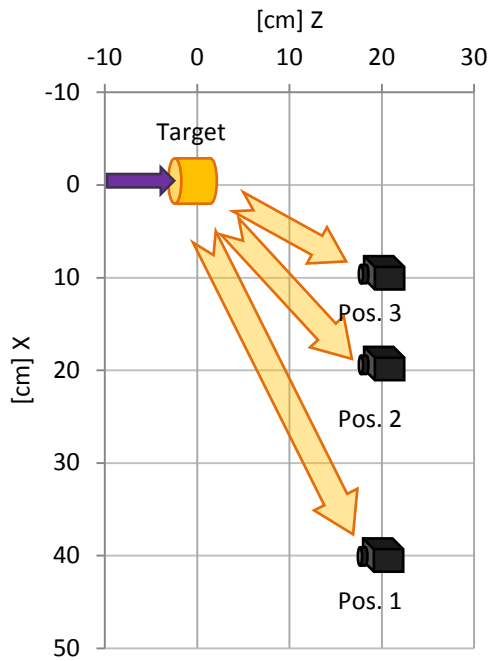


Fig. 4.4: Dimensions of the experimental setup.

The experimental setup was observed by two analogue cameras for visual alignment. Platforms were controlled remotely. Digital devices were connected through power cords, going out of the cave, for hard reset feature. Transistor chips

---

were wired outside the cave for in-situ measurements of their electrical characteristics. Ethernet connections were also routed with 20-30 m cables outside the cave for safe and reliable readout.

### 4.3 MOS transistor testing circuit.

It was decided to perform in situ measurements of characteristic curves of the MOS transistor chips. A SIPMOS<sup>®</sup> Small-Signal-Transistor [59] was selected for tests. It is a n-channel type, enhancement mode, logic level transistor (Fig. 4.5).

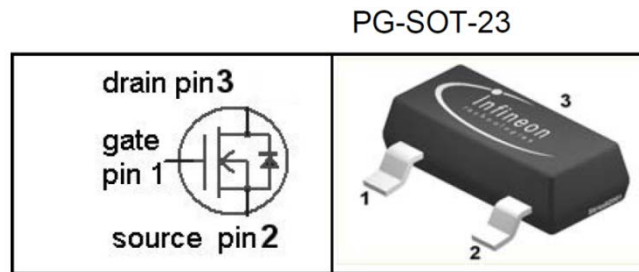


Fig. 4.5: Transistor chip.

Table 4.1: Transistor specifications.

Type	BSS131 PG-SOT23
Package Pb-free	Yes
Tape and reel information	L6327: 3000 pcs/reel
Marking	SRs

Two chips were soldered on a circuit board, mounted in special holders on the moving platform and covered with a polymer foil for verification of beam profile. The organic foil becomes darker proportionally to the number of ions passed through it (Fig. 4.6).

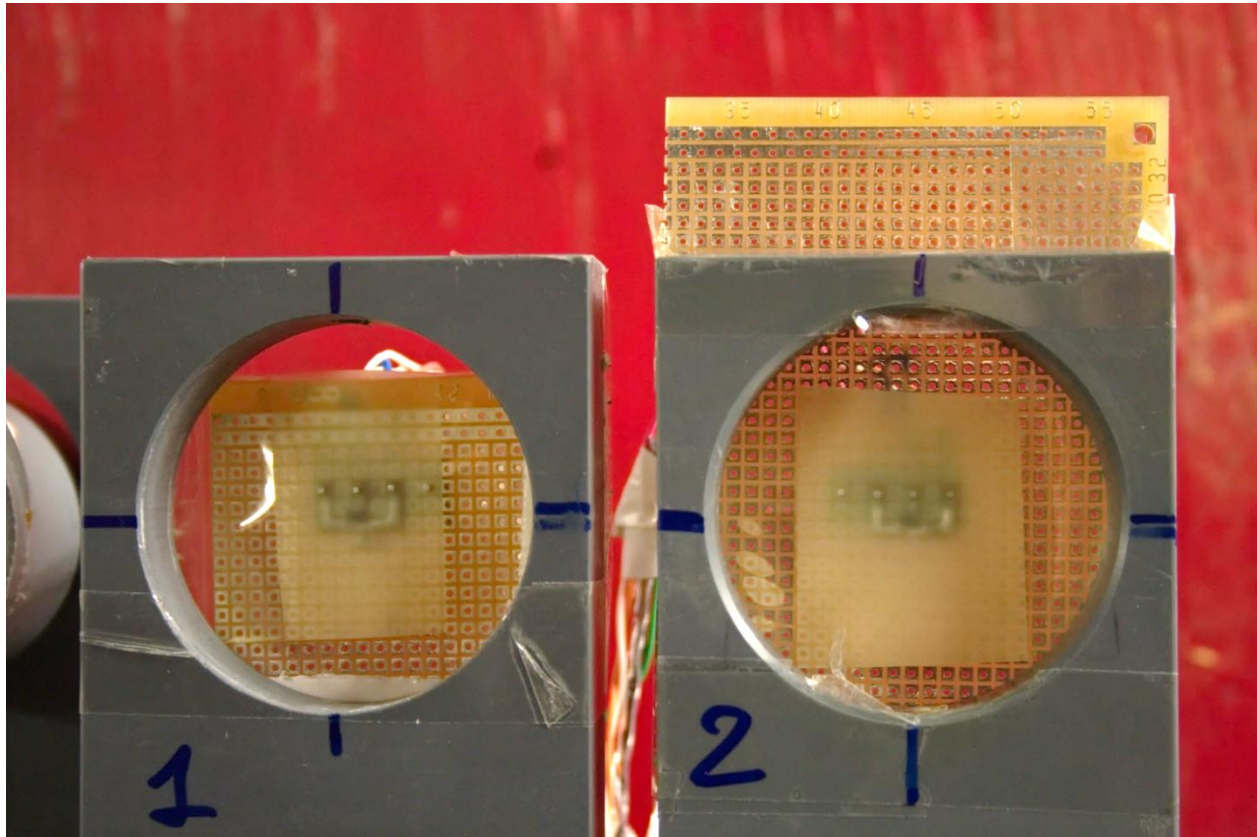


Fig. 4.6: Transistor chips setup in HHD cave.

The challenge of the measurement was to place measuring equipment and power supply in the radiation safe area, but with the shortest possible cabling to the chip in the cave in order to reduce the effect of electrical properties of the cable. The principal circuit for measurement was consisting of DC power supply, AC power supply, 10 ohm resistor and oscilloscope (Fig. 4.7). The CH1 and CH2 channels were connected to the oscilloscope X and Y axis. Therefore we could observe the characteristic curve on the screen. Oscilloscope was able to save both screenshots and raw data to USB stick at command (Fig. 4.8).

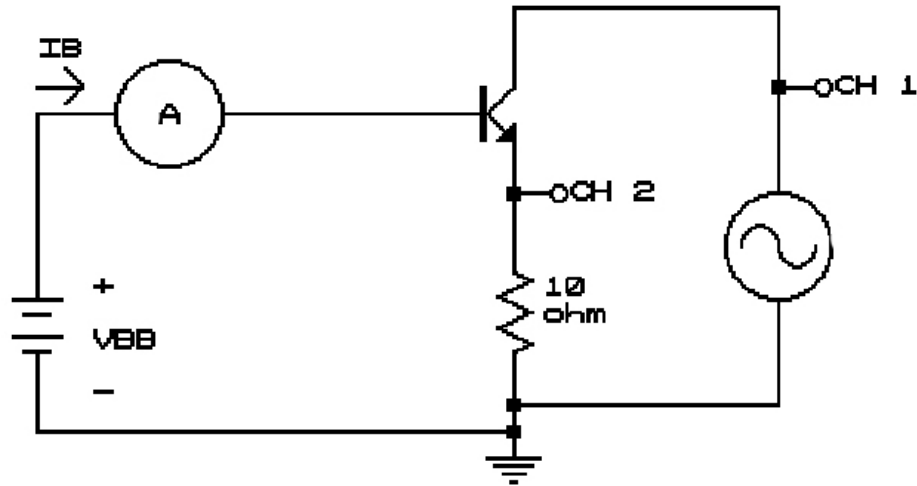


Fig. 4.7: Testing circuit.

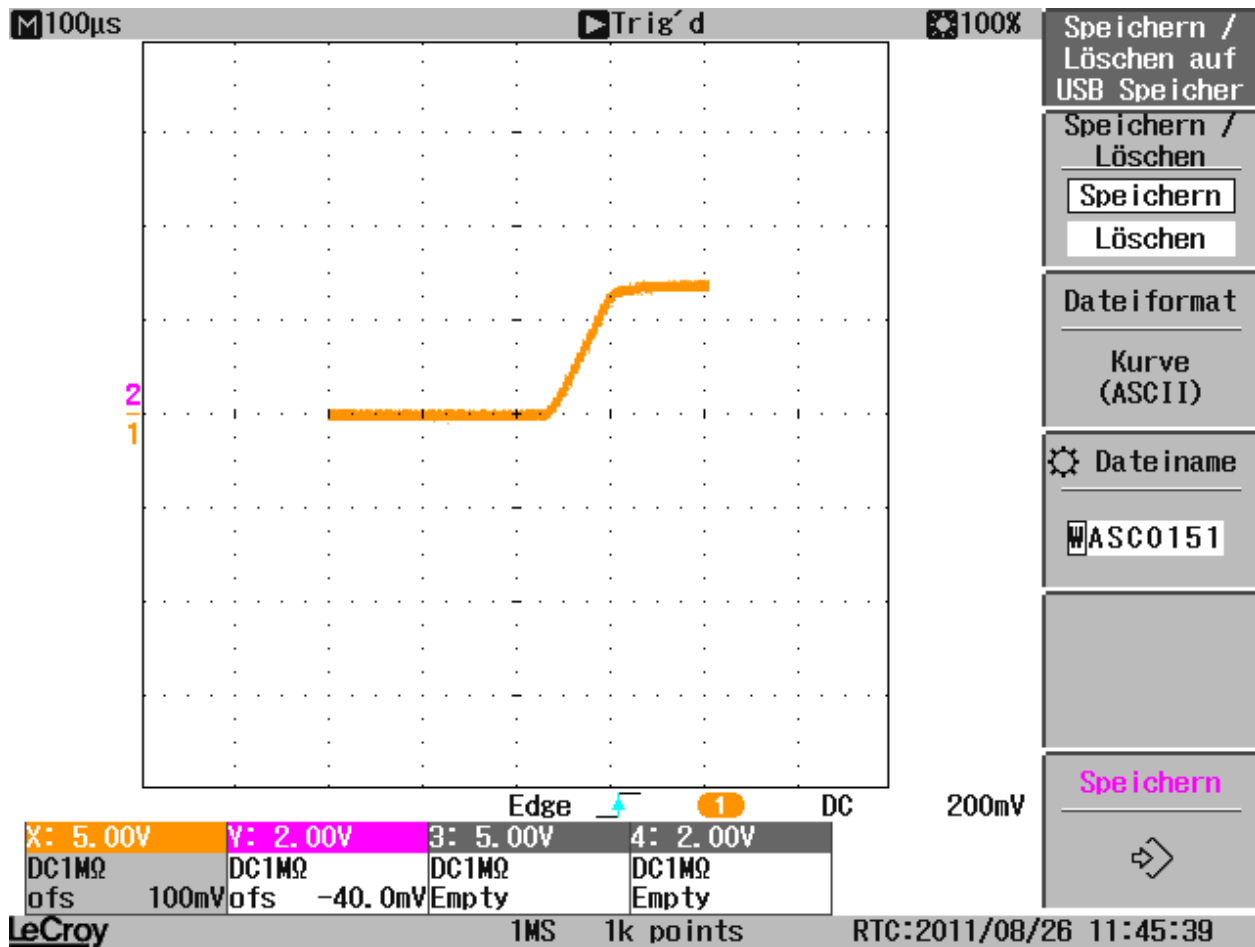


Fig. 4.8: Oscilloscope readings example.  $V_{GS}$  to  $I_D$ ,  $V_{DS} = 3$  V.



---

## 4.4 CCD Readout

### 4.4.1 Digital – LabVIEW based code

Several identical Ethernet CCD cameras were put under test during irradiation experiments. Ethernet protocol is very common for such applications as digital CCD cameras operation and acquisition nowadays. Basler scA640-74gm [60] is the camera model, which was tested (Fig. 4.9). It is a monochrome CCD camera with relatively high frame rate, designed for industrial and scientific purposes. Table 4.2 shows basic information about the model.



Fig. 4.9: Digital camera for tests.

Table 4.2: CCD camera basic information

Vendor	Basler
Model	scA640-74gm
Type of data presented	Typical
Number of samples	100
Sensor	Sony ICX414AL
Sensor type	CCD
Sensor diagonal	Diagonal 8 mm (Type 1/2)
Indication of lens category to be used	C-Mount
Resolution	659 x 490 pixel
Pixel width	9.90 $\mu\text{m}$
Pixel height	9.90 $\mu\text{m}$
Readout type	Progressive scan
Transfer type	
Shutter type	-
Overlap capabilities	-
Maximum frame rate	74 frames/second
General conventions	
Interface type	Gigabit Ethernet

Making in-situ measurements of the CCD behavior was a challenging task. The camera suppliers are not providing proper software development kit with the product. A LabVIEW development kit [61] was chosen for this task. It has a NI-IMAQ library, which is compatible with most of modern camera drivers. LabVIEW is a component based development kit, which has a graphical oriented application building system. The typical application made in LabVIEW is consisting of modules, connected with each other. Each of these modules is consisting of smaller and simpler modules and so on until it gets to very basic calculation and memory access commands. A view on a part of the module diagram of the application, developed for this study is shown in Fig. 4.10.

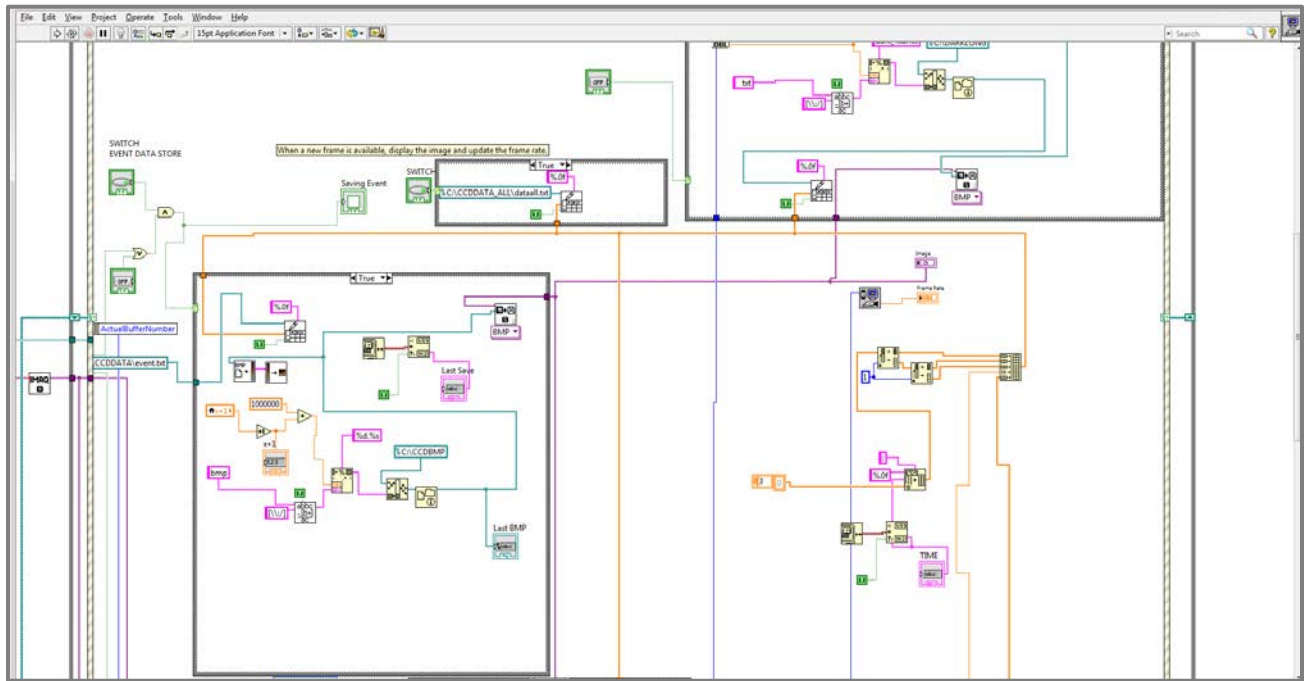


Fig 4.10: Part of the LabVIEW block diagram.

There are many modules available in LabVIEW libraries, e.g. for file IO (input output), for GUI (graphical user interface), for array and matrix operations and so on. The NI-IMAQ library contains very useful modules for camera acquisition and control, which allowed us to build rather complicated application. Besides NI-IMAQ modules it was consisting of numeric and matrix data storage and operations, IO of data and several GUI elements. The application was developed further from experiment to experiment. GUI of one of the versions of the application is shown in Fig. 4.11.

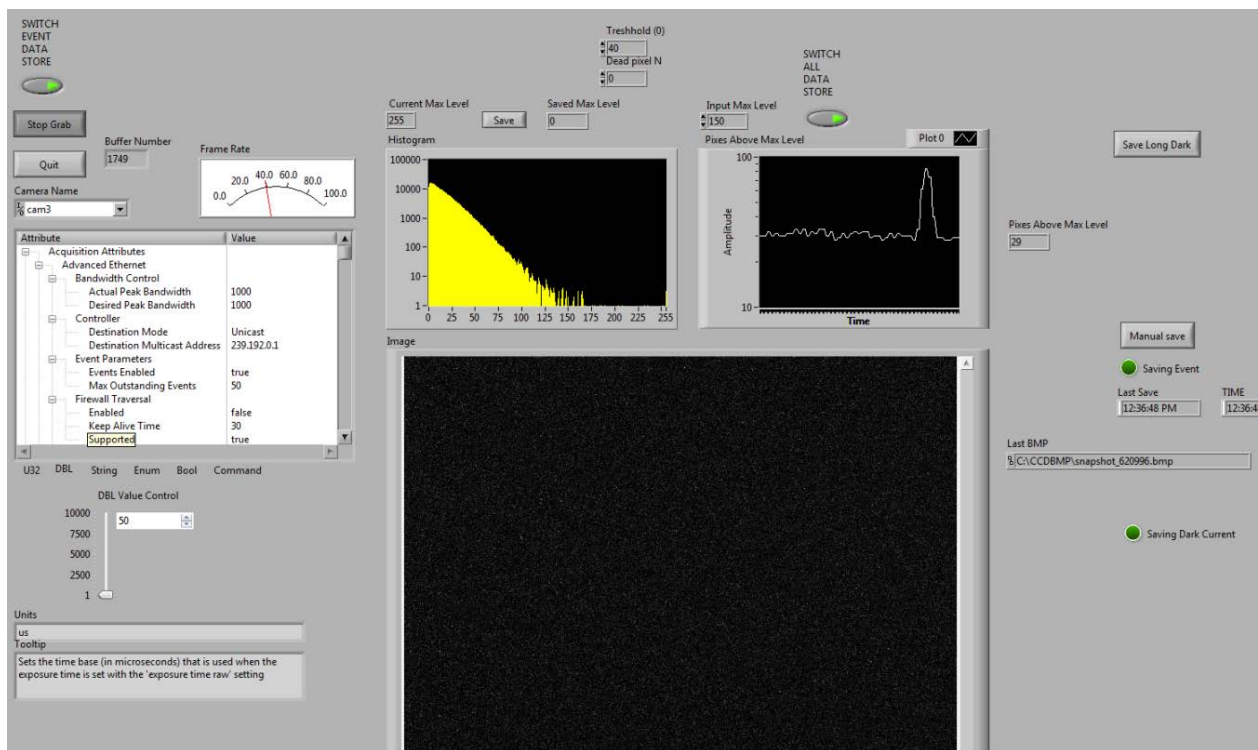


Fig. 4.11: GUI of the camera read-out software.

A group of controls over various camera parameters and attributes is on the left side of the window. In the middle there is a current picture from the camera. It is black with a slight background, produced by the dark current. Above the camera image there is a histogram and a plot, which indicates the number of pixels above certain level. This value was used for triggering the event selection process, because it has a peak during a beam pulse. A later version of the application has a plot of charge on the top (Fig. 4.12). It shows the sum of all pixel gray values in the image. This sum is proportional to the charge, collected from the matrix during a current frame exposition. This value is very important for prompt radiation effect study.

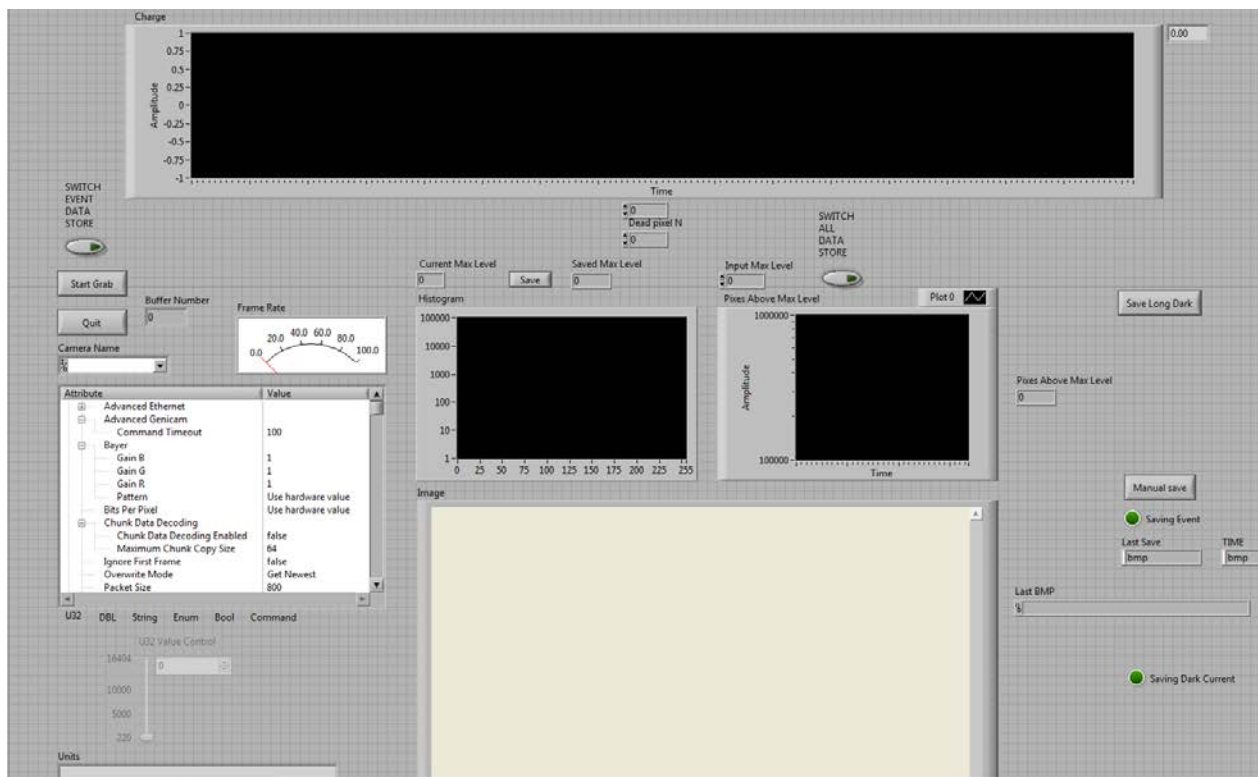


Fig. 4.12: GUI of the camera read-out software version 2.

The signal from the camera was acquired through independent local network, built for this experiment with orientation on radiation safe areas. Two Ethernet cables were installed for the possibility of simultaneous access of 2 cameras. Two power cables were installed for “hard reset” feature in case of camera malfunctions due to high radiation.

#### **4.4.2. Digital CCD calibration**

It is important to know the actual electric charge, collected by CCD during certain exposure. Normally we only have pixel grey values in digital form and we want to calculate a charge out of this number. A principle of the CCD camera operation is illustrated in Fig. 4.13. Charge units accumulated by the photo irradiance is converted into a voltage, amplified, and finally converted into a digital grey value [62].

The whole process is assumed to be linear and can be described by a single quantity, the overall system gain  $K$  with units DN/e-, where DN is the Digital Number.

$$\mu_y = K(\mu_e + \mu_d) \quad \text{or} \quad \mu_y = \mu_{y.\text{dark}} + K\mu_e, \quad (4.1)$$

with:  $\mu_y$  – signal in DN,  $\mu_e$  – number of photo electrons,  $\mu_d$  – number of dark current electrons,  $\mu_{y.\text{dark}}$  – dark current signal in DN. We will use a noise phenomenon for further calculations. Noises in a CCD camera are a result of three factors:

- shot noise (Poisson distributed):  $\sigma_e^2 = \mu_e$
- all noise sources related to the sensor read out and amplifier (normal distributed):  $\sigma_d^2$
- analog digital conversion noise:  $\sigma_q^2 = 1/12 \text{ DN}^2$

Using the linearity of process:

$$\sigma_y^2 = K^2 (\sigma_d^2 + \sigma_e^2) + \sigma_q^2 \quad (4.2)$$

And applying equation 4.1 to 4.2 we get:

$$\sigma_y^2 = \underbrace{K^2 \sigma_d^2 + \sigma_q^2}_{\text{offset}} + \underbrace{K}_{\text{slope}} (\mu_y - \mu_{y.\text{dark}}).$$

This method is known as the Photon Transfer Method [63, 64]. Now we make shots of some equally illuminated plain surfaces. We calculate standard deviation (STD) of the signal in DN, mean signal in DN and signal with closed lenses in DN, which is the dark current signal. After series of measurements we use Ordinary

Least Squares method to build a linear dependency between the variance of the noise  $\sigma_y^2$  and mean photo-induced signal. That is how we calculate Overall System Gain  $K$  (Fig. 4.14). Each camera normally has unscaled gain setting. We will call it camera gain. The calibration procedure was performed for 320, 640, 960 and 1020 camera gain values (Fig. 4.15). It is clear from the results, that the camera gain is not linear with the actual Overall System Gain. But calibration procedure may be repeated for any camera gain setting for most accurate results. Camera gain values of 320 and 640 were used during irradiation experiments.

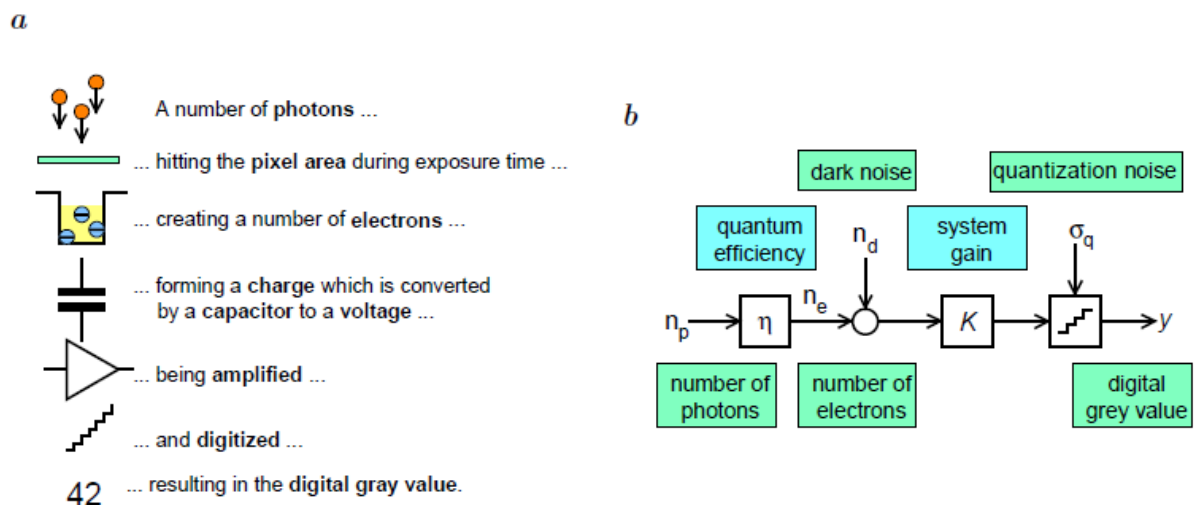


Fig. 4.13: a) Physical model of the camera and b) Mathematical model of a single pixel [62].

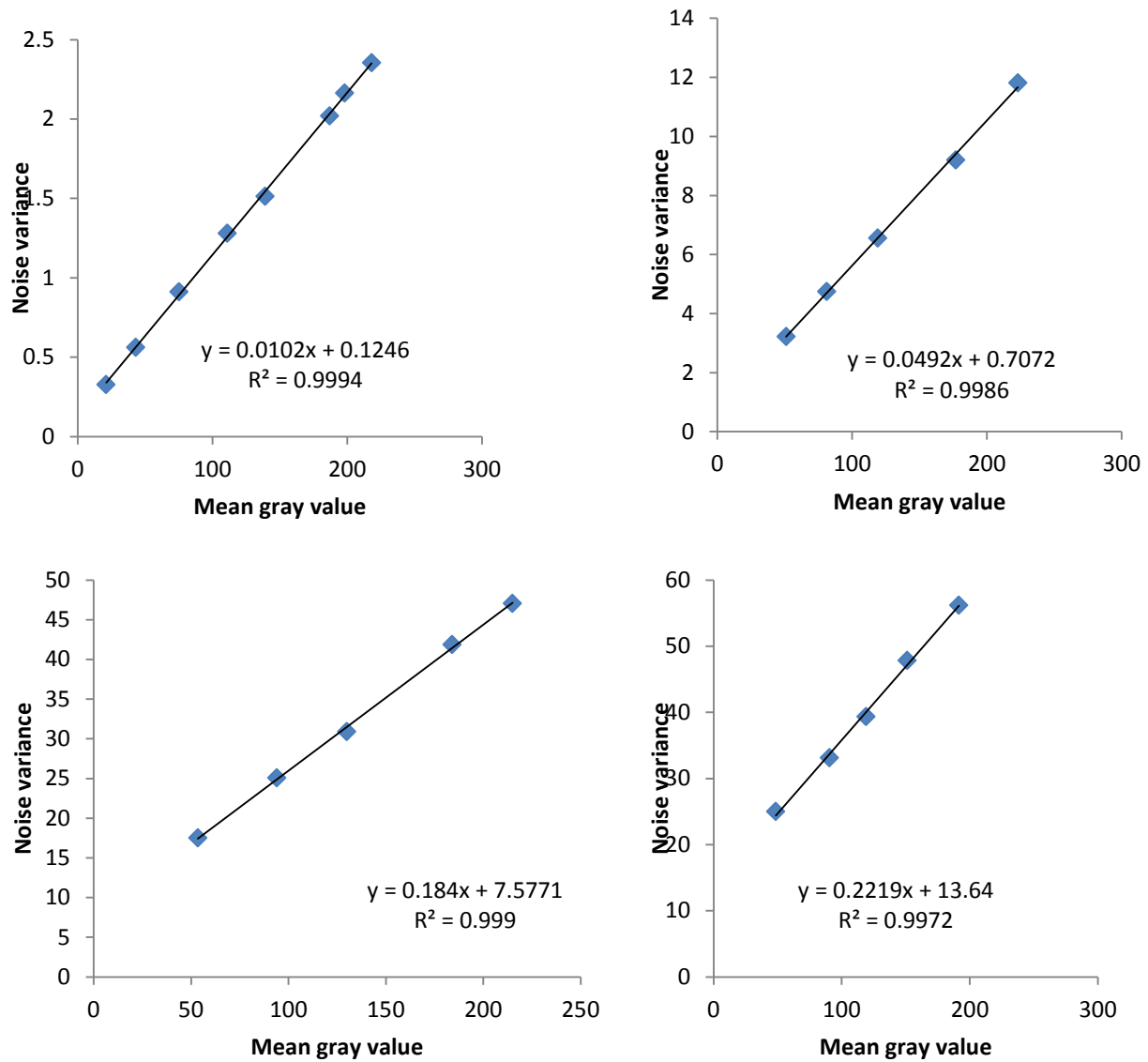


Fig. 4.14: Mean gray value versus gray value STD for 320, 640, 960 and 1020 camera gain.

Table 4.3: Camera gain to Overall System Gain relation.

Camera gain	K
320	0.0102
640	0.0492
960	0.184
1020	0.222

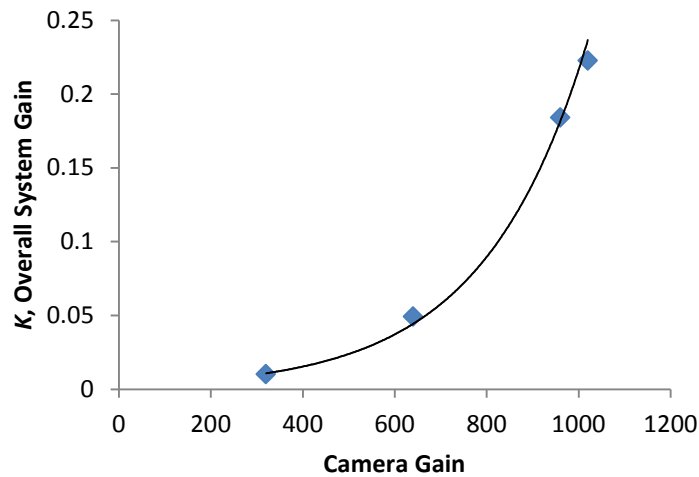


Fig. 4.15: Camera gain to Overall System Gain relation.

#### **4.4.3. Analogue CCD acquisition**

The advantage of analogue CCD is the ultimate reliability of operation during irradiation sessions. When digital components of Ethernet cameras tend to turn into the error state and require reboot of the device, analogue cameras work with no significant failures and provide an image of CCD continuously. It was decided to use this advantage to study the effect of direct high energy Heavy Ion beam hitting the CCD matrix. Unfortunately, with the technology progress, digital products are taking advantage of analogue in most applications. That is why it was complicated to find a camera, which would meet the experiment requirements for 100%. The one, which was available for a reasonable price was not a professional industrial one, so the information about gain and some other attributes was not 100% reliable. But for the purposes of the experiment even such a device was sufficient. It was a monochrome CCD camera, manufactured by CONRAD, model name 420 TVL (Fig. 4.16). Table 4.4 shows some basic information about the camera.



Fig. 4.16: Analogue camera for tests.

Table 4.4: Analogue camera basic properties.

Resolution	420 TVL
Output	1x BNC 75 Ohm 1Vss
Operating voltage	12V/DC
Operating temperature range	-10 to +50 C
Image sensor	8.5 mm
Focal length	3.6 mm
Light sensitivity	0.05 lx
Protection type	IP65
Power consumption	Max 200 mA

The existing GSI cable system was used to transfer the camera signal from the cave to the main control room. At this point it was acquired with a CCTV video receiver card. An application was saving images continuously with a 24 frames per second rate. These image stacks were later processed with another LabVIEW based application, designed for offline image processing. It was calculating the

---

sum of pixel gray values over the whole frame for these groups of images, as well as mean pixel gray value and its standard deviation over the frame. The system was operating with no failures, and analogue CCD readout was proven to be reliable even under direct heavy ion bombardment.



## 4.5. Switch testing technique

An Ethernet switch HP 2520-24-PoE [65] was selected for tests, because it is one of the models, which were ordered for installation in GSI network system, including accelerator network in vicinity of “hot spots”, where radiation conditions are critical for semiconductors (Fig. 4.17). Specifications are presented in Table 4.5.



Fig. 4.17: HP 2520-24-PoE Ethernet Switch

The switch was configured as a node of the accelerator network of GSI. It was connected to another network node in a nearest rack box outside the cave in a radiation safe area, behind the concrete shielding. The switch was given a static IP address. A batch script for a windows command line was written so, that it was pinging given IP every second, writing a status in a command line window and saving a log in a text file. For a packet loss situation a warning beeping sound was implemented. That allowed us to notice failure immediately and safely hard reset the switch. A power supply cable was routed outside the cave for such a scenario.

Table 4.5: HP 2520-24-PoE Ethernet Switch specifications.

Address table size	8000 entries
Form Factor	1U height
Input Frequency	50/60 Hz
Input Operating Current	3.3/1.6 A
Input Voltage	100-127/200-240 VAC
Power consumption	257 W (maximum)
Power consumption, standby	21.6 W
Product dimensions (W x D x H)	9.69 x 17.44 x 1.75 in.
Total Number of Network Ports	26
Number of PoE (RJ-45) Ports	24
Number of Network (RJ-45) Ports	2
Port/Expansion Slot Details	24 x Fast Ethernet Network 2 x Gigabit Ethernet Expansion Slot
Media & Performance Network Technology	10/100/1000Base-T 10/100Base-TX
Ethernet Technology	Gigabit Ethernet Fast Ethernet

---

## 4.6. Dosimetry

Irradiation experiments always require estimations of doses and deposited energy in the tested material. In the current studies we use two approaches for dose estimation and verification.

Firstly we carry out simulations of the experiment scenario with Monte Carlo codes and placement of virtual detectors to score energy depositions and doses. This allows us to have an estimation of the expected dose levels in different points of the experimental cave with given beam parameters and design the experiment accordingly. Monte Carlo calculations are described in detail in a separate chapter of this work.

The second approach is the experimental measurement of the dose by passive dosimeters. Alanine Electron Paramagnetic Resonance (EPR) dosimetry technique was chosen for current study because of several advantages, such as small dosimeter size, good accuracy and dynamic range, reasonable price and good reliability [66-68]. This technique is accepted internationally as reference standard dosimetry system and is often used in industrial radiation processing and radiotherapy. A specification of the type, used in the experiment is given in the Table 4.6.

Dosimeters were mounted as close as possible to the devices under test, considering radiation field direction and gradient (Fig. 4.18), so that the actual dose on the device would be equal to the dose collected by the dosimeter. Small size of dosimeter units allowed us to achieve reliable accuracy. Sometimes additional dosimeters were mounted in the experimental area. They served as complementary reference points, to reproduce spatial dose map and cross check Monte Carlo calculations (Fig. 4.19). After irradiation, dosimeters were removed from experimental cave and sent for processing to the dosimetry laboratory, located in

Munich. Sometimes it was impossible to remove dosimeter right after the irradiation, because of high activation in experimental cave. Such scenarios could have led to small additional expositions of dosimeters to secondary ionizing radiation, coming from beam dump and losses in transport line. Such uncertainties were estimated to be less than 15%.



Fig 4.18: Dosimeter (red ellipse) mounted on the CCD camera.

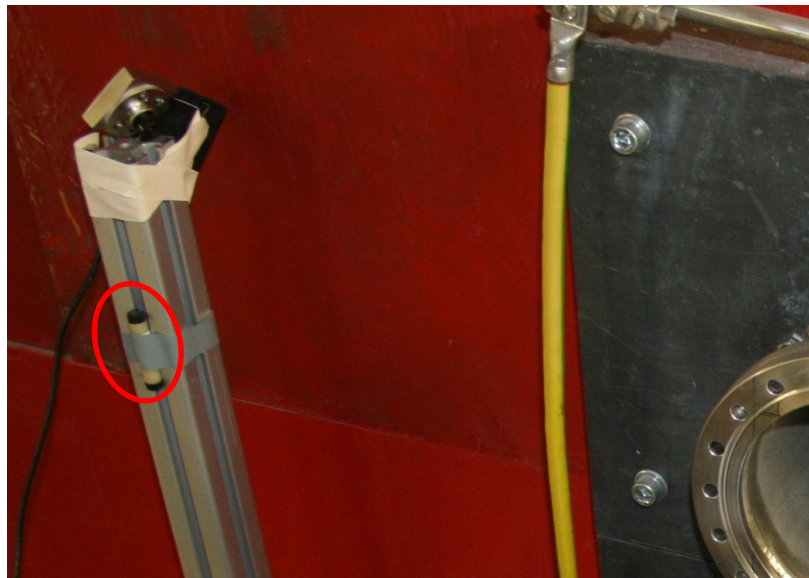


Fig 4.19: Dosimeter (red ellipse) mounted in the vicinity of beam loss point.

Table 4.6: Technical information of Alanine EPR dosimeter.

Type:	AWM230
Material:	85% w/w L- $\alpha$ -Alanine 15% w/w Paraffin wax (binder)
Shape:	Rods,      Diameter    4.8 mm Length        10 mm
Mass:	ca. 230 mg
Lot mass variation:	< $\pm 1\%$
Density:	1.27 g/cm <sup>3</sup>
Lot EPR reproducibility:	< $\pm 0.5\%$ <sup>(1)</sup>
Most suitable dose range:	1 Gy to 200 kGy
Detection threshold / upper limit:	ca. 0.1 Gy / ca. 500 kGy
Type of dose response function:	$A(D) = A_{\max} * [1 - \exp(D_{37}^{-1} * (D + D_0))]$ <sup>(2)</sup>
Temperature coefficient of dose response:	0.19 - 0.40 %/ $^{\circ}$ C <sup>(3)</sup>
Max. irradiation temperature:	70 $^{\circ}$ C
Fading of dose response:	< 0.5 %/year <sup>(4)</sup>



---

## 5. Results and discussion

---

### 5.1 Indirect irradiation effects

#### 5.1.1 Long term effects in CCD cameras

Digital CCD cameras are rather radiation sensitive, because of digital components, that is why they were only irradiated in secondary radiation fields, caused by heavy ion beam interaction with metals. During several irradiation sessions the cameras have collected up to several hundred grays, based on alanine dosimeter indications. Such dose led to significant effect in CCD sensor, and finally even the digital readout and processing circuits were irreversibly damaged.

Normally, each CCD sensor chip has some level of background noise that is usually stated by the manufacturer in the device specifications. It is caused by so called dark current. During exposure of CCD chip to radiation field the dark current is increasing. It is also dependent on the temperature. That is why all measurements were done on “warm” device, i.e. operating CCD chip at a room temperature environment.

Practically increase of dark current is observed as increase of grey level of each pixel. Some pixels are more damaged, some less, i.e. some appear as more bright dots some as less bright. All in all it results in an increase of the mean pixel gray value and seen as a TV screen noise, but in static. Fig. 5.1 shows an example of picture, filmed by the camera with closed lenses after being exposed to 70, 170 and 400 grays.

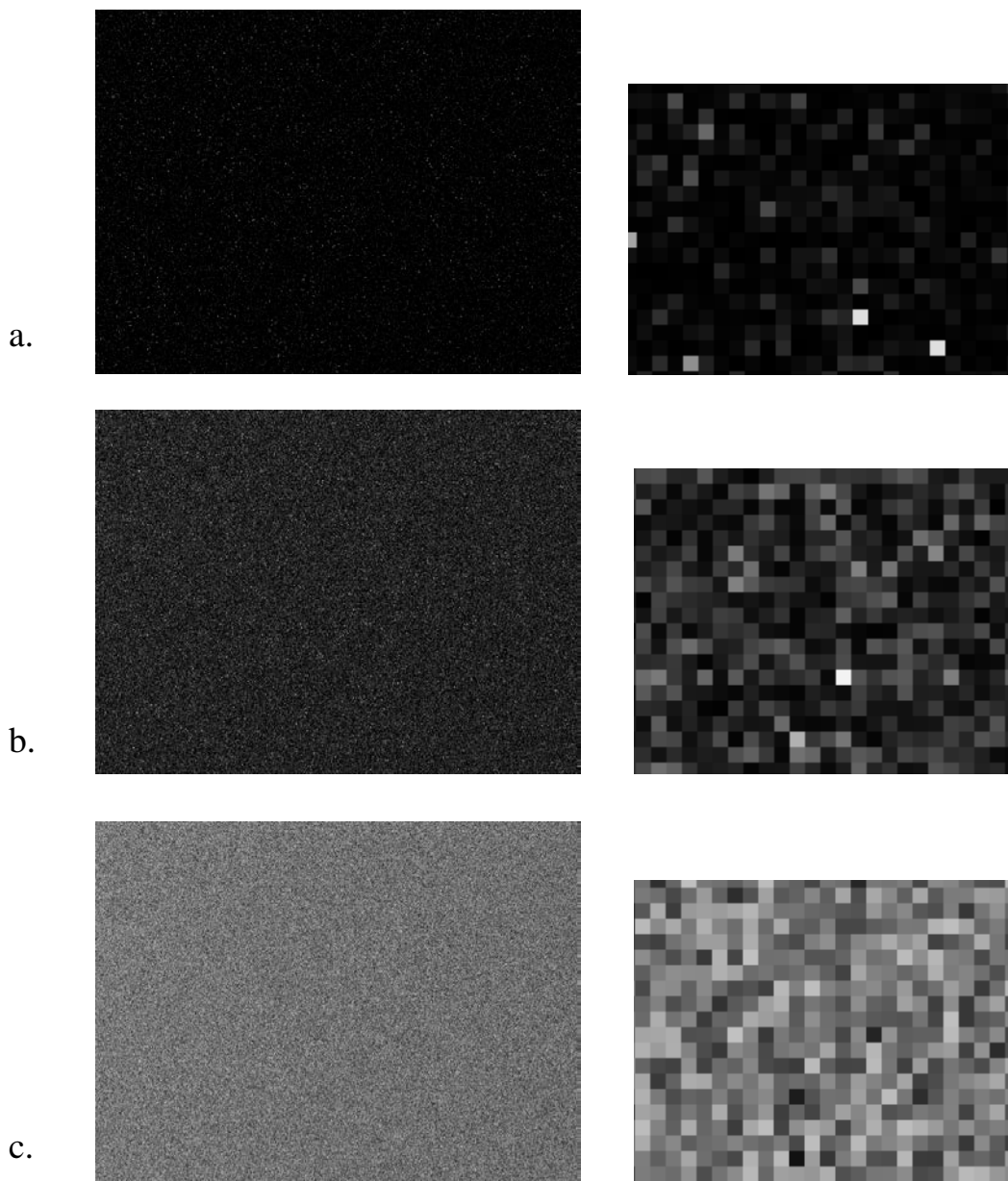


Fig. 5.1: Full screen and zoomed part of the screen, filmed by the camera with closed lenses after a – 70 grays, b – 170 grays, c – 400 grays.

The frames were taken with the following camera attributes: exposure time – 200 ms, camera gain – 360 (default setting). Camera gain is a conditional value; each manufacturer may use a different scale. The process of calculation of actual

---

physical values such as electrical charge from the pixel gray value is described in detail in subchapter 4.4.2 of the current work.

We may conclude, based on these images, that the quality of pictures from such a CCD camera would degrade dramatically after being exposed to doses of hundreds of grays. The background noise caused by dark current is so high, that it basically makes it impossible to get descent images from the camera.

The physical numerical characteristic of this noise – dark current is normally measured in charge/pixel/sec. It may be calculated using formula 5.1.

$$\mu_y = K(\mu_e + \mu_d), \quad (5.1)$$

with  $K$  – Overall System Gain,  $\mu_y$  – grey value of the pixel,  $\mu_e$  – number of photo electrons and electrons produced by ionisation in the pixel,  $\mu_d$  – number of dark current electrons in the pixel. We assume that  $\mu_e = 0$ , because the lenses are closed and we take a shot, when there is no beam on, and no ionising particles are passing through the CCD. We have a value of  $K$  from camera calibration for current attributes. Fig. 5.2 shows the evolution of dark current, calculated as a mean value over all pixels in the CCD chip [69]. The value of TID (Total Ionisation Dose) is taken from alanine dosimeter readings. This result shows that the dark current value is increasing in direct proportion to TID in a range of up to 400 grays. The radiation damage effect in CCD cells does not reach saturation under the given conditions. At about 500 grays the electronics of the camera stopped responding even after numerous hard resets. Most likely it means that the electronic components, being exposed to radiation, accumulated enough defects to reach a critical threshold voltage shift. It means that logical states 0 and 1 may be no longer distinguished in some logical components, which leads to impossibility of further device operation.

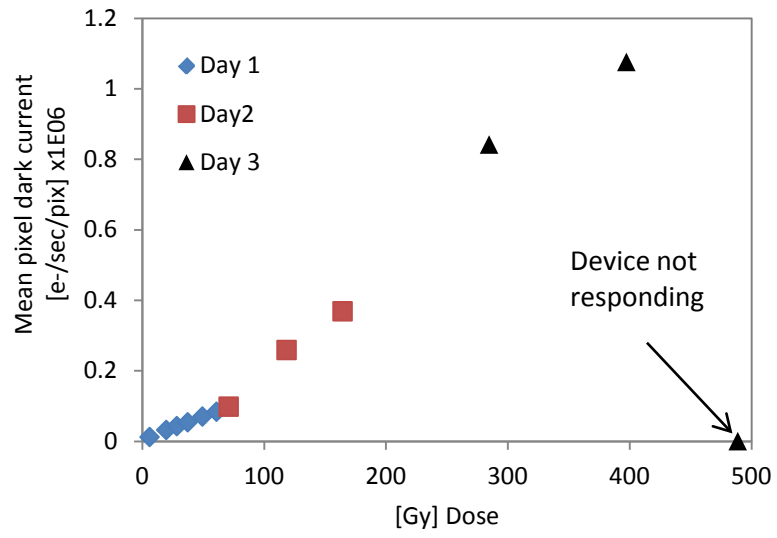


Fig. 5.2: Dark current evolution with total dose.

---

### **5.1.2 Short term effects in CCD cameras**

When ionizing particles travel through the materials of a CCD chip they produce electron-hole pairs, which are later collected and registered by the camera electronics [69]. This happens at the moment when the beam interacts with a metal target and produces secondary radiation. Considering the fact, that the beam pulse is about 300 ns, the whole process takes no longer than a one frame exposure which is 20 ms. It means that normally each beam pulse is affecting only one frame in acquisition sequence. Experimental data confirm this fact. We will call such frame an “event frame” and all other frames in between we will call “dark frames”.

Visually an event frame looks like a dark frame, but with an addition of some bright pixels all over the frame. On a video sequence it looks like a short splash, synchronised with a beam loss. An example of typical dark frame and event frame is shown in Fig. 5.3. These frames are captured during irradiation of a 5cm long aluminium cylinder with 0.95 GeV/u Uranium beam with camera in position 3 (Fig. 4.4) and beam intensity  $1e8$  ions/spill. Bright pixels on the dark frame are permanent defects, long term effects have been described before. Additional bright pixels on the event frame are formed by charges from ionizing particles, passing through the CCD matrix. Sometimes these pixels are grouped in clusters and even form discernible traces of ionizing particles.

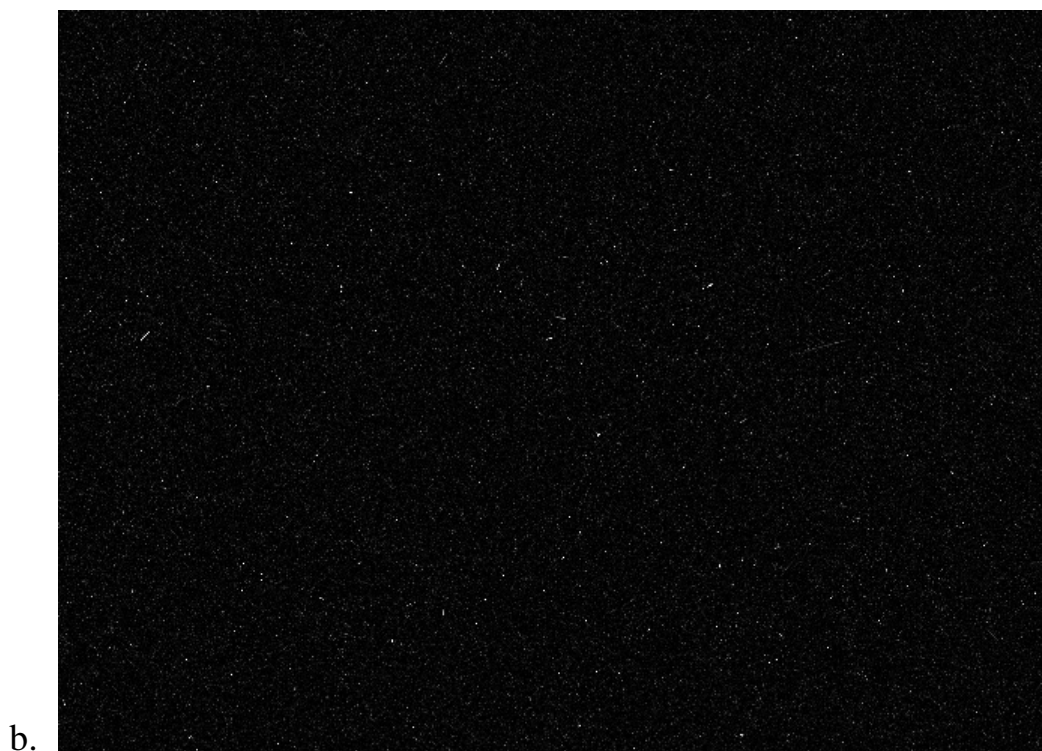


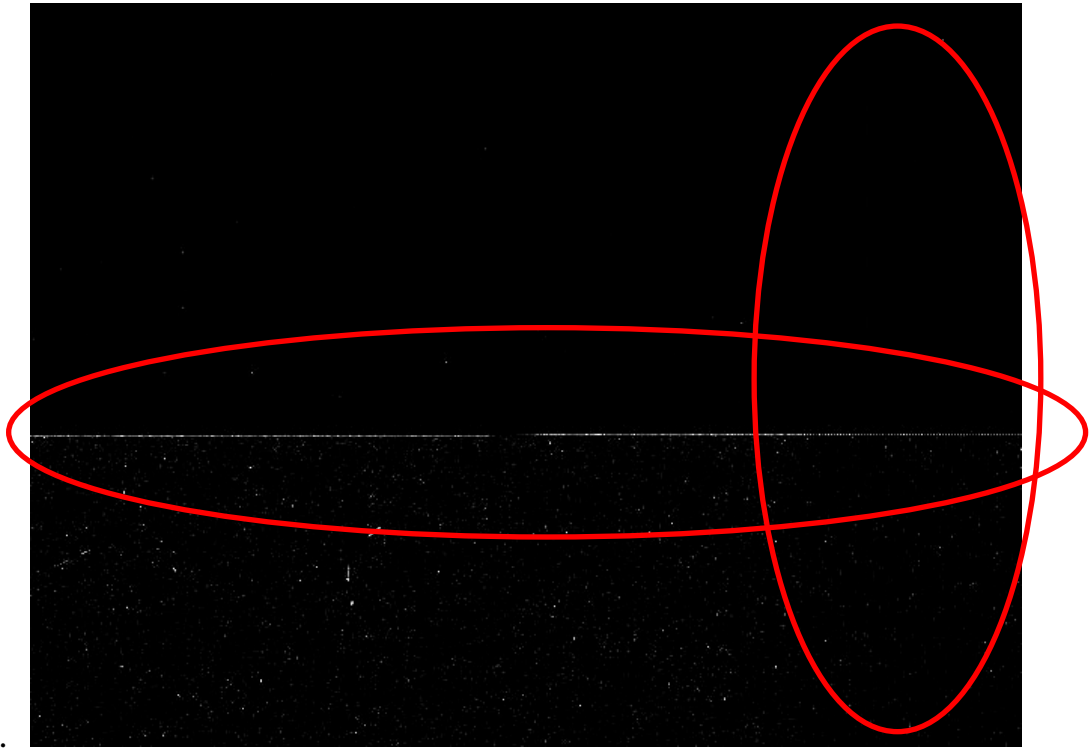
Fig. 5.3: a) Typical dark frame, b) Typical event frame. Frames were captured during irradiation of a 5cm long aluminium cylinder with 0.95 GeV/u Uranium beam with camera in position 3 (Fig. 4.4) and beam intensity  $1e8$  ions/spill.

---

Sometimes during the beam spill we have observed more unusual frame acquisition than just the normal event frame. We have noticed several types of distortions on some of the event frames. A digital CCD camera is a rather complicated device, and not only the CCD chip is exposed to radiation, but all of the electronics, that is responsible for correct processing and acquisition of data. As a result we got frames with the following distortions (Fig. 5.4):

1. Partial loss of the frame. Upper part of the event frame is represented by the previous frame (dark frame). The part may be bigger or smaller. The 1 pixel wide stripe of bright pixels is separating normal part of the frame from the lost part. Pixel grey value in this stripe is not uniform.
2. Loss of every second pixel column in part of the frame. The width and position of the defect area is always the same - right side of the frame and about 1/5 part of the frame width. Each second column of the defect area is represented by pixels with absolute 0 grey value, i.e. the signal from these pixel columns is completely lost.
3. Horizontal dark wave effect. A gradient horizontal darkening is seen on top of the normal event frame. The size is always the same and is about 1/10 of frame height and full width. The position is different.

These 3 defects appeared independently and sometimes together on the same frame. Detailed analysis of the principles of the occurrence of these effects has not been carried out as part of this work. These defects may vary, depending on camera model and concept.



a.



b.

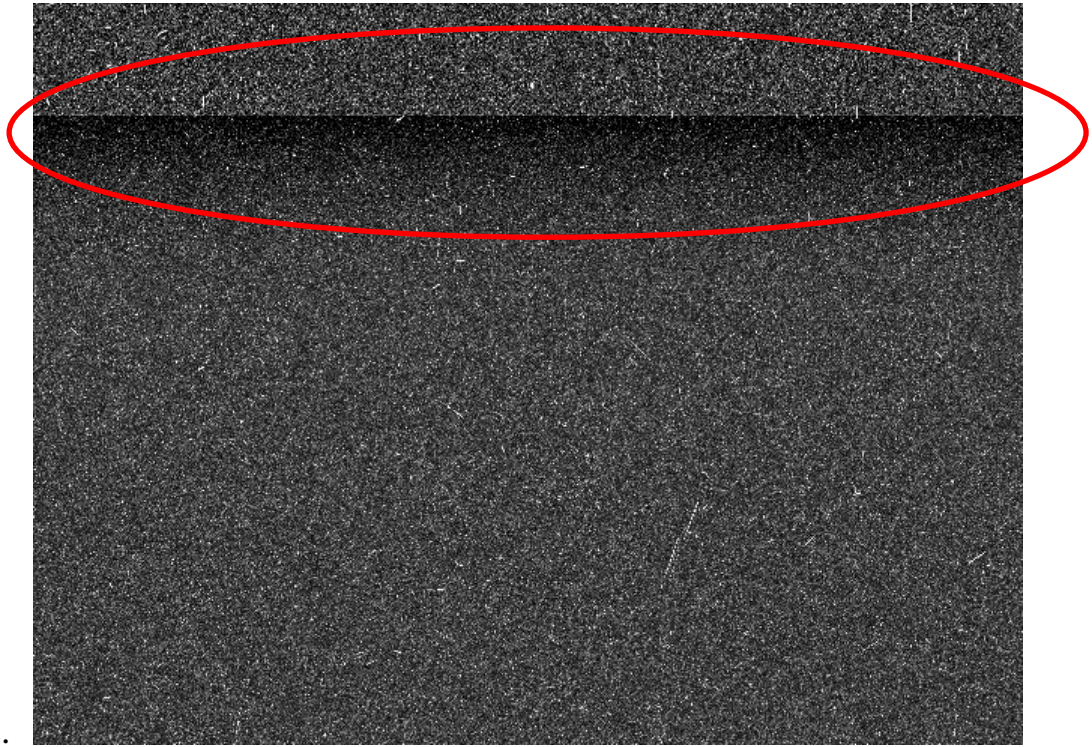


Fig. 5.4: a) Distortion of 1 and 2 type, b) Distortion of 2 and 3 type, c) Distortion of 3 type. Frames a and b were captured during irradiation of a 5 cm long aluminium cylinder with 0.95 GeV/u Uranium beam with camera in position 3 (Fig. 4.4) and beam intensity  $1e8$  ions/spill. Frame c was captured with the same conditions, but  $1e9$  ions/spill intensity of primary beam.

Visual brightness of given pixel is its grey value and is represented as a number from 0 to 255 in 8bit mode. This number is proportional to the charge, collected from the pixel during frame exposure. We may calculate total and mean grey values of pixels all over the CCD chip. An Overall System Gain coefficient defined earlier allows us to convert grey value to charge. Fig. 5.5 shows an example of mean pixel value evolution with time. Peaks are event frames and background consists of dark frames. We are subtracting mean background value

around the peak from peak values to calculate grey value difference and then charge, induced by the prompt ionizing radiation in the chip for each event frame.

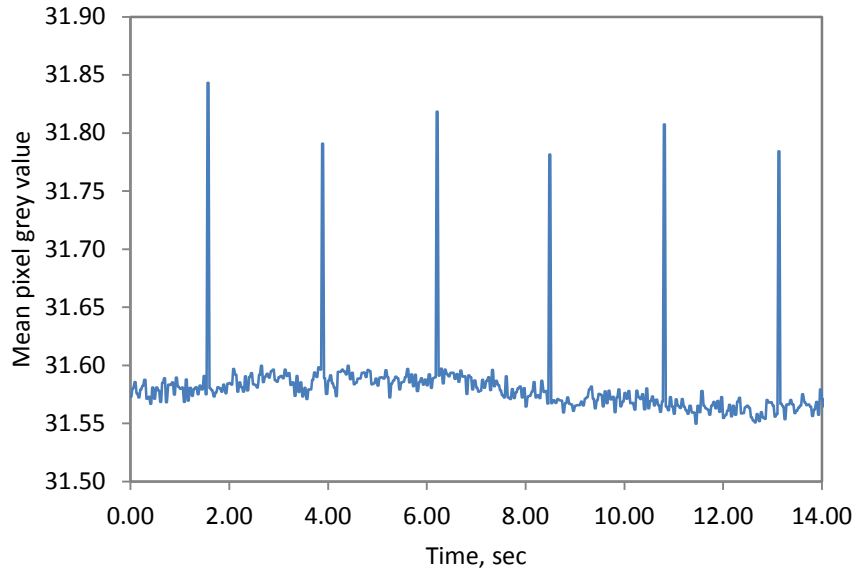


Fig. 5.5: Mean pixel grey value evolution in time. Data from irradiation of 10.8 cm long aluminium cylinder with 0.5 GeV/u  $N^{+7}$  ion beam with camera in position 1 (Fig. 4.4) and beam intensity  $1e9$  ions/spill.

The charge induced by prompt ionizing radiation is a good physical numerical indication of the radiation effect on CCD matrix. Fig. 5.6 shows data points, measured during series of 0.95GeV/u Uranium beam pulses onto the 5 cm long aluminium target with different intensities and camera in position 3. One can notice that data points are clustered along a linear relation. The spread is bigger for lower values, because of the logarithmic scale. We may separate the data points in 2 general groups. The first group consists of points, clustered along the linear relation – these are normal event frames. The second group is located below the linear approximation. The charge value is significantly lower for these data points. The second group consists of distorted event frames. As described above all distortions lead to the underestimation of the total grey value and therefore the

charge. That is why the points are below the linear approximation and have a different offset.

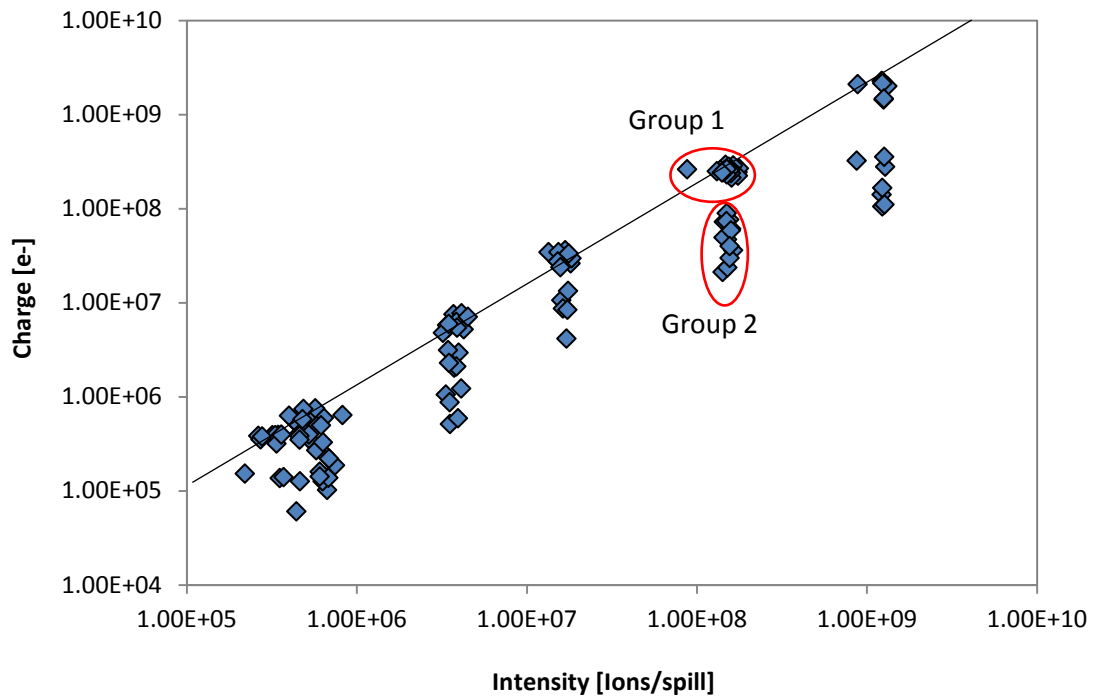


Fig. 5.6: Charge in CCD versus primary beam intensity. Data acquired during irradiation of 5cm long copper cylinder with 0.95 GeV/u Uranium beam and camera in position 3 (Fig. 4.4). Group 1: normal event frames, group 2: distorted event frames.

We were able to carry out measurements in primary beam intensity ranges of more than 4 orders of magnitude. Lower intensity would give us too much spread, and higher intensities were not technically available. But even at the highest available intensity the stability of the CCD camera operation was rather poor. It would stop working every 5-10 beam spills, and required hard reboot. These malfunctions were related to Single Event Upsets (SEU) and will be discussed later. Visually prompt ionizing radiation effects look a lot different within several orders of magnitude. Fig. 5.7 shows an example of frames with zoomed parts.

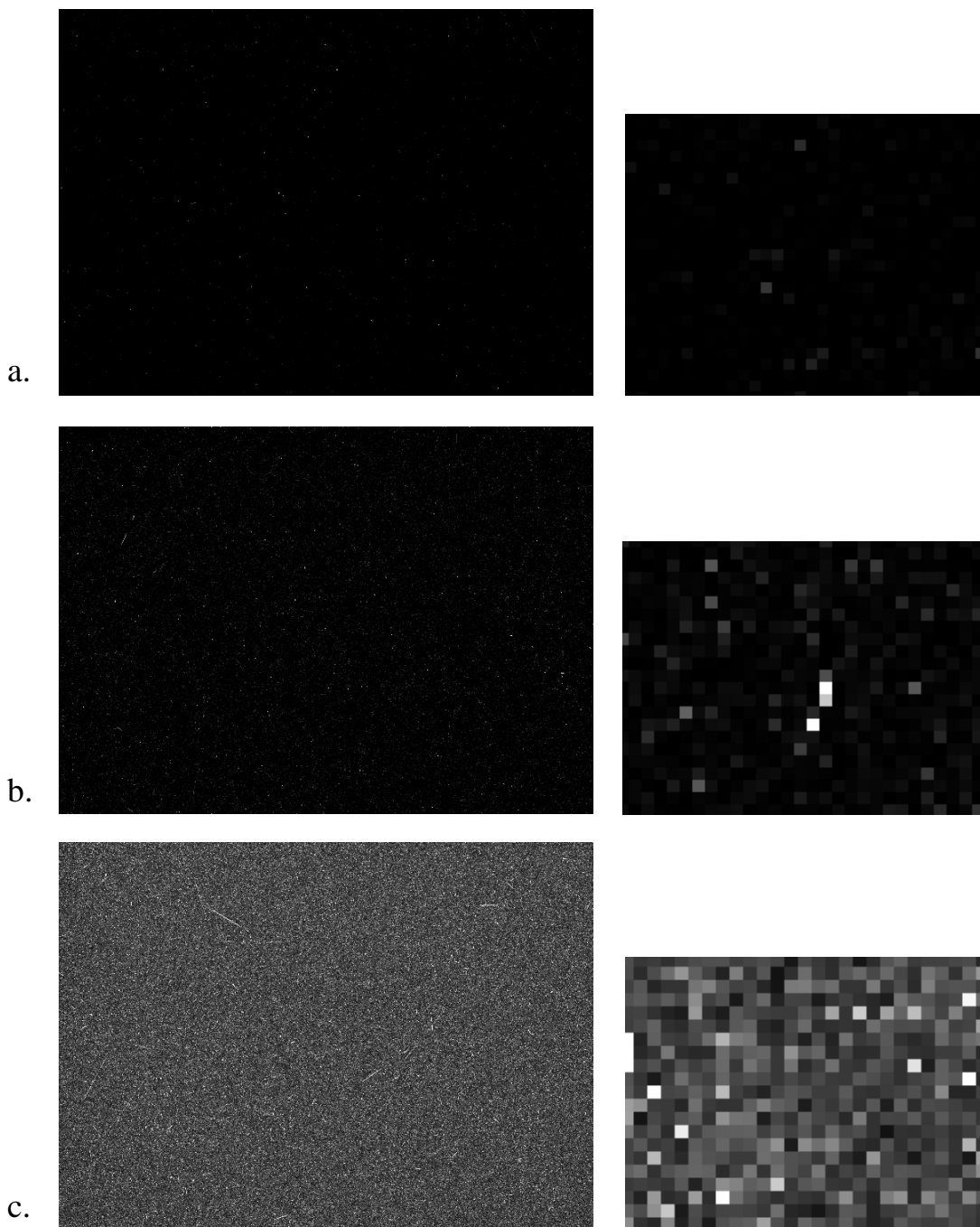


Fig. 5.7: Event frames with zoomed parts. Data acquired during irradiation of 5cm long aluminium cylinder with 0.95 GeV/u Uranium beam and camera in position 3 (Fig. 4.4), a)  $1e7$  ions/spill, b)  $1e8$  ions/spill, c)  $1e9$  ions/spill.

While at  $1e7$  ions/spill the effect of prompt radiation is not visually significant, at  $1e9$  it is so great that it would definitely interfere with any kind of scientific

measurements and even simple surveillance. Criteria formed by this result may be very useful during design of future accelerators or upgrade of current machines.

One of the experimental goals was also to get an idea about the angular distribution of secondary ionizing radiation and corresponding effects on the CCD chip. Fig. 5.8 shows event frame data points for all three camera positions, measured during series of 0.95 GeV/u Uranium beam pulses onto the 5 cm long aluminium target with different primary beam intensities. The pattern of data points is identical for all three camera positions. Linear approximation includes only event frames, which are not of distorted type.

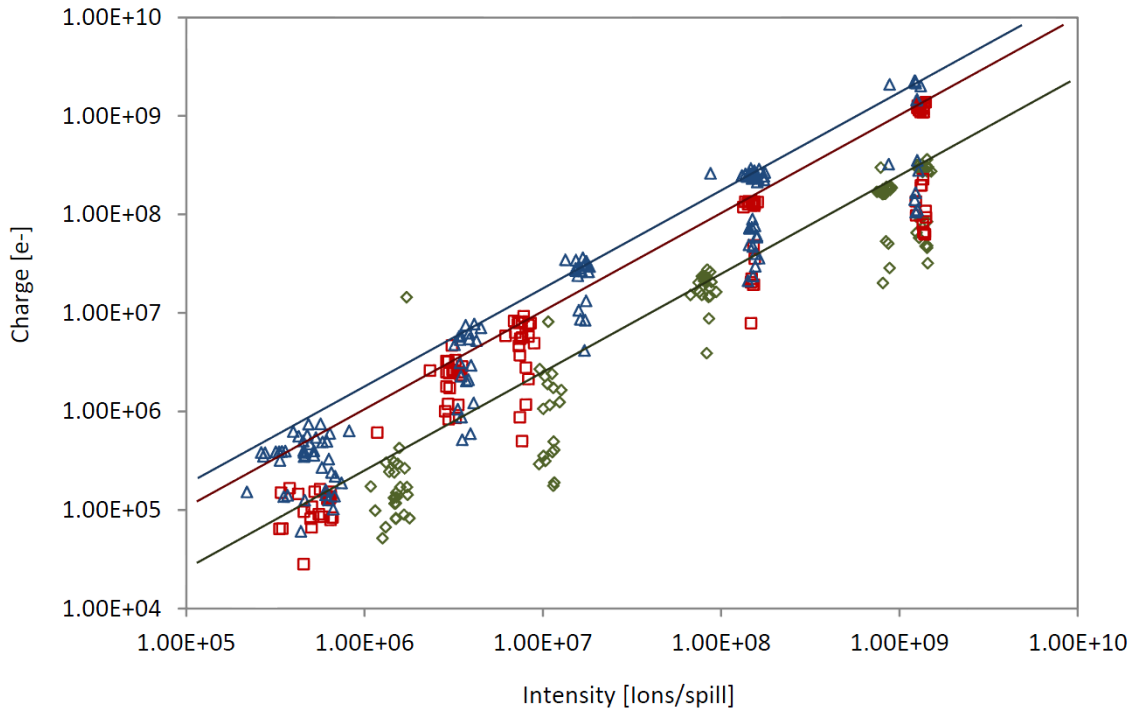


Fig. 5.8: Charge in CCD versus primary beam intensity. Data acquired during irradiation of 5cm long aluminium cylinder with 0.95 GeV/u Uranium beam.

Camera positions: 1 – green diamonds, 2 – red squares, 3 – blue triangles.

To characterize a prompt radiation effect on the CCD chip depending on position we may calculate a value of charge per primary beam intensity for each

camera position 1, 2 and 3 (Table 5.1). Graphically this value is represented as an offset of linear approximation for each of the three camera positions on Fig. 5.8. Furthermore, we may plot this value over  $1/r^2$ , where  $r$  is the distance of the CCD chip from the target – the source of secondary radiation. (Fig. 5.9)

Table 5.1: Charge produced in CCD by prompt secondary radiation divided by intensity of primary 0.95 GeV/u Uranium beam for three camera positions.

	Distance from the target, $r$ [cm]	Charge/Intensity [e-/ions/spill]
Pos. 1	45	1.7
Pos. 2	28	0.9
Pos. 3	22	0.2

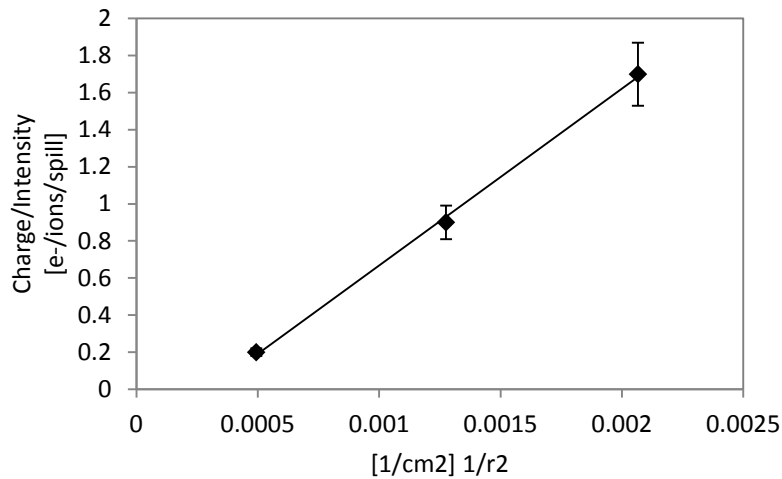


Fig. 5.9: Charge/Intensity over  $1/r^2$ , where  $r$  is a distance of CCD chip from the target.

Data points fit on the linear approximation for three camera positions that are located at about 25, 45 and 60 degree to primary beam direction. It means that the secondary radiation effect on the CCD is roughly isotropic within angles of 25 to

---

60 degree to primary the beam direction. This fact may be useful for estimations of radiation effects on CCD cameras in the presence of known beam losses.

### **5.1.3 Ethernet switch stability and SEU in digital devices**

The ethernet switch was tested in a 6 hour irradiation session with a 0.95 GeV/u Uranium beam pointed at a 5cm long aluminum target at maximum intensity of  $1e9$  ions/spill. Device positioning in relation to target was chosen on the base of reports of similar device failure rate in SIS18 tunnel of GSI facility and described above. It was expected to have failures due to SEU not more often than every 10 minutes. Switch failed 3 times during the whole irradiation session. This result does not have a good statistical accuracy, but is enough to make rough order-of-magnitude estimate. Unfortunately it was impossible to repeat the experiment, because of technical problems and very limited amount of beam time shifts.

SEUs were observed in digital CCD cameras during irradiation as well. We were counting every failure, which was leading to a state when the camera stopped responding and required a hard reset. With known beam spill repetition rate and known beam intensity we arranged the results in the following way (Table 5.2, Fig. 5.10). SEU cross section for the digital CCD cameras is roughly proportional to  $1/r^2$ , where  $r$  is distance from the target. SEU for the switch has an offset of more than 1 order of magnitude from digital camera SEU value. This result proves that SEU may vary significantly due to feature size, used in different digital devices.

Table 5.2: SEU cross sections.

Device, position	Distance from the target [cm]	Failure rate, 1/hr	SEU cross section, 1/Ions	Dose, $\mu\text{Gy}$
CCD pos. 1	45	20	2.00E-10	0.5E07
CCD pos. 2	28	80	6.67E-10	2.0E07
CCD pos. 3	22	140	1.17E-09	0.5E08
Switch	55	0.5	4.17E-12	0.3E07

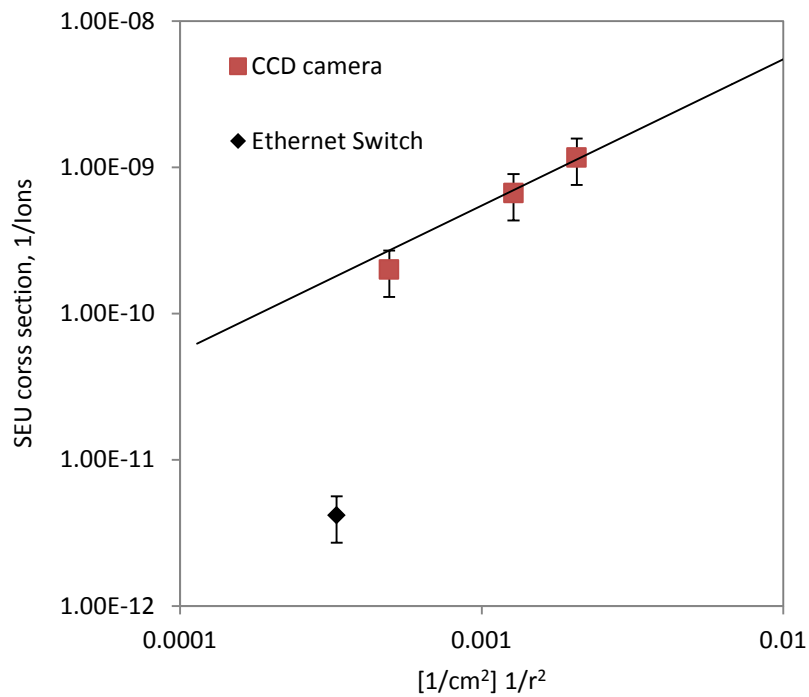


Fig. 5.10: SEU cross sections as a function of distance between DUT and beam loss point.

---

## 5.2 Direct irradiation effects

### 5.2.1 Long term effects in MOS transistor

Besides irradiation of semiconductor devices with secondary radiation it was also interesting to make some tests under direct ion irradiation. This is a situation which directly takes place in space where the devices are hit by HZE (high mass and energy) ions from Galactic Cosmic Rays. MOS transistor chip was irradiated with 0.5GeV/u Ta beam directly. Naturally such high energy ions are penetrating through the MOS chip. The total number of ions on the chip was  $9.2E10$  ions/cm<sup>2</sup>. The characteristic curve of the transistor was measured in-situ. Fig. 5.11 illustrates the threshold voltage shift. The plot shows the shape of the characteristic curve and indicates the position of the threshold voltage. Red curve is initial curve before irradiation. Blue curve is measured after chip exposure to  $4.4E10$  ions/cm<sup>2</sup>. The shape of the curve remains identical, but it's position changes.

The evolution of characteristic curve may be divided into two stages. (Fig. 5.11-12) At first it was only shifting to the left, i.e. the threshold voltage was decreasing. When the chip had been exposed to about  $4.4E10$  ions/cm<sup>2</sup> the behavior of evolution of the characteristic curve changed. On the second stage the curve would jump back and forth, i.e. threshold voltage was decreasing or increasing, balancing around some middle value. Assuming that the second stage starts from  $4.4E10$  ions/cm<sup>2</sup> we can calculate the average threshold voltage value - 7.05 V, i.e. the overall threshold voltage shift is 8.6 V in negative direction.

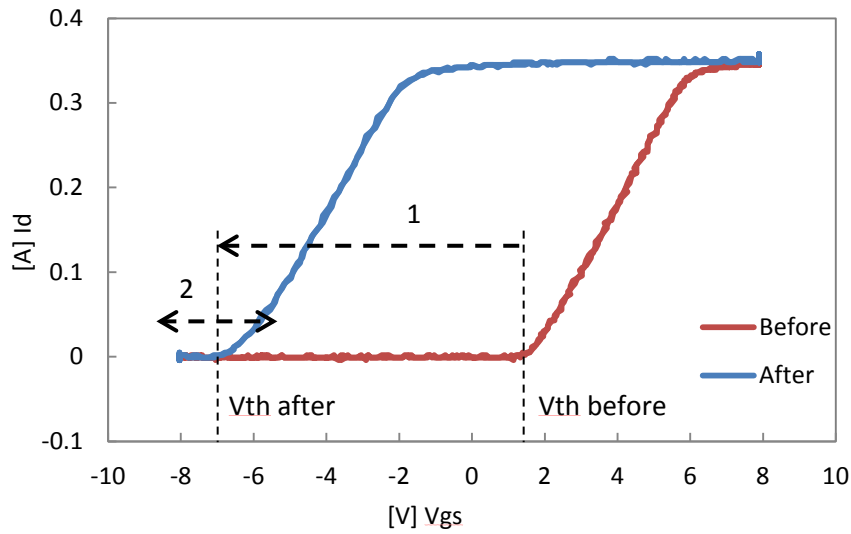


Fig. 5.11: MOS transistor characteristic curve evolution during irradiation with 0.5 GeV/u Ta beam. Red curve: before irradiation. Blue curve: after irradiation with  $4.4E10$  ions/cm<sup>2</sup>. Numbers 1 and 2 indicate two stages of evolution.

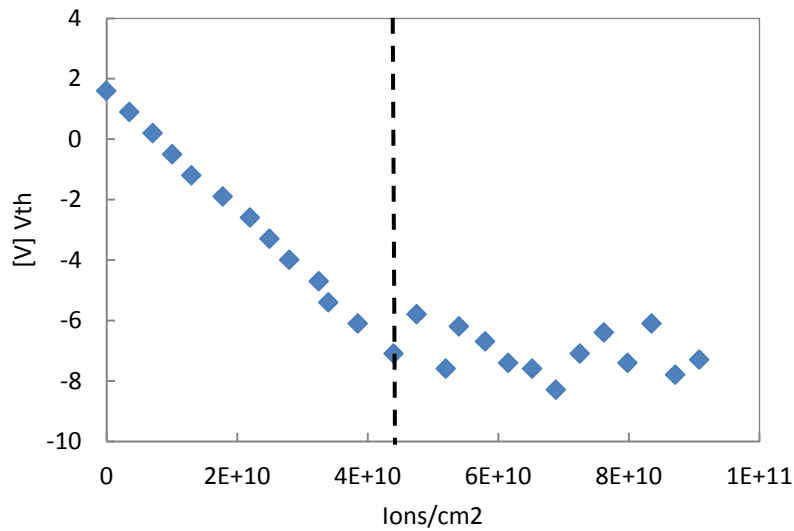


Fig. 5.12: MOS transistor threshold voltage evolution during irradiation with 0.5 GeV/u Ta beam. Dashed line indicates two stages of Vth evolution.

### 5.2.2 Degradation of CCD sensor from direct ion beam.

An interest in direct effects on CCD matrix came during our studies. A low cost analogue CCD camera was acquired in order to carry out such test. The camera was irradiated with a direct beam of 0.2 GeV/u Uranium. Each spill was about  $1e9$  ions. Beam was focused in  $2 \text{ cm}^2$  area. The camera was staying in radiation environment before direct irradiation, and collected a rather high dose. That is why the image with closed lenses on the moment of direct irradiation had quite a lot amount of bright pixels due to high dark current. The first frame on fig. 5.13 shows a picture from the camera on the moment of start of direct irradiation.

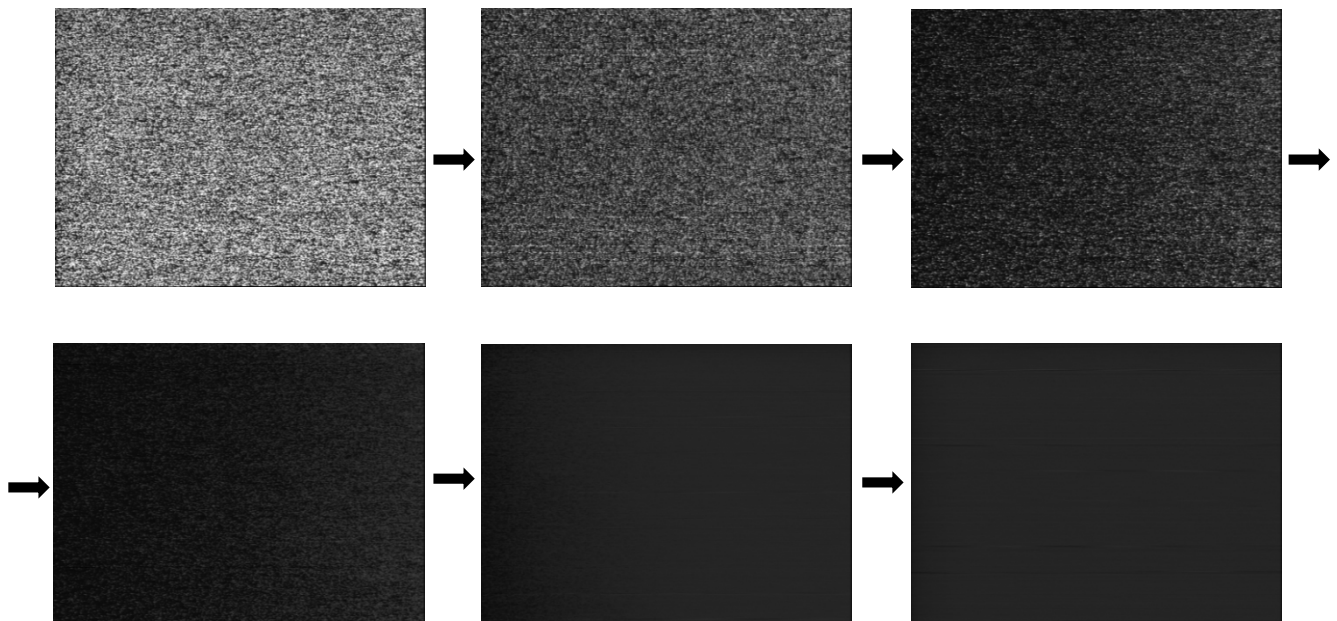


Fig 5.13: Camera image evolution during direct irradiation with 0.2 GeV/u Uranium over 6 beam spills consisting of  $1e9$  heavy ions each. Every other frame is taken after each spill.

---

Unfortunately this camera model had automatic gain feature and it was not possible to disable it. That is why we will be not focusing on absolute values in results processing. The evolution behavior may be described as loss of contrast and sensitivity of the CCD matrix. Absolute value of total grey pixel value dropped as well. Frames acquired during irradiation were processed with LabVIEW based application. Sequence of frames was processed and a plot of total pixel gray value versus frame number was displayed (Fig. 5.14). Significant changes are happening approximately every 50 frames, which is 2 seconds at 25 fps (frames per second) – beam spill repetition frequency.

Frames were further processed with image analysis software to calculate standard deviation of pixel gray value. The STD of mean pixel grey value in this case describes contrast. Number of picture value on Fig. 5.14 is proportional to the number of beam spills value, displayed on Fig. 5.15. Each point on fig 5.15 corresponds to frame on fig 5.13. As we see the mean pixel grey value STD drops even more with further irradiation after the 4th frame, it describes further loss of contrast and sensitivity of the CCD matrix. The same is not true for the absolute value of mean pixel grey value. As an outcome from this result we may summarize that the CCD chip is very sensitive to high intensity heavy ion beam spills. CCD chip completely lost sensitivity and contrast during only 20 spills of  $1e9$  0.2 GeV/u Uranium beam. And only four spills were enough to make already about 80% of the whole effect.

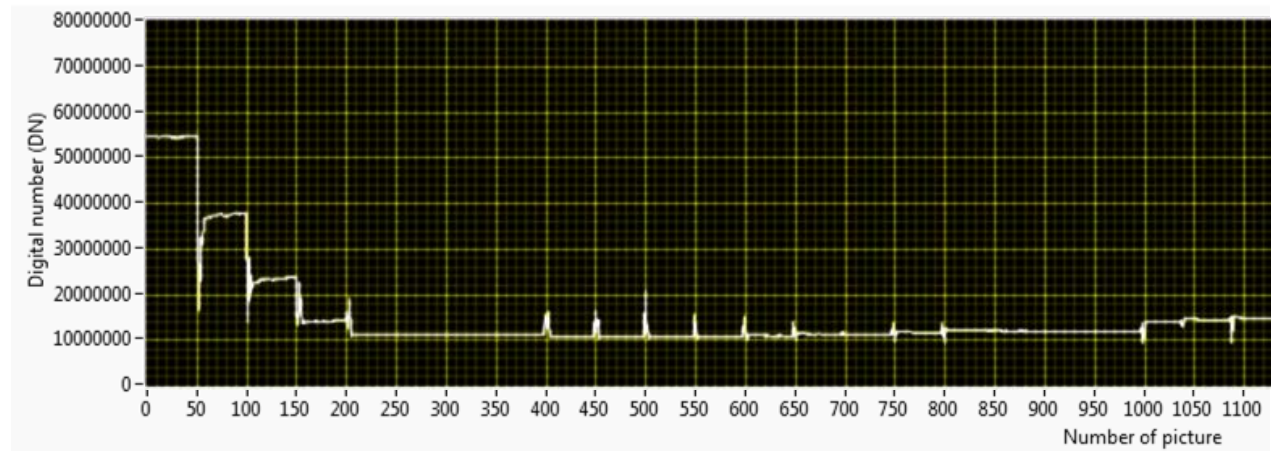


Fig. 5.14: Application plot area. Total grey value or total DN (Digital Number) versus frame number at 25 frames per second.

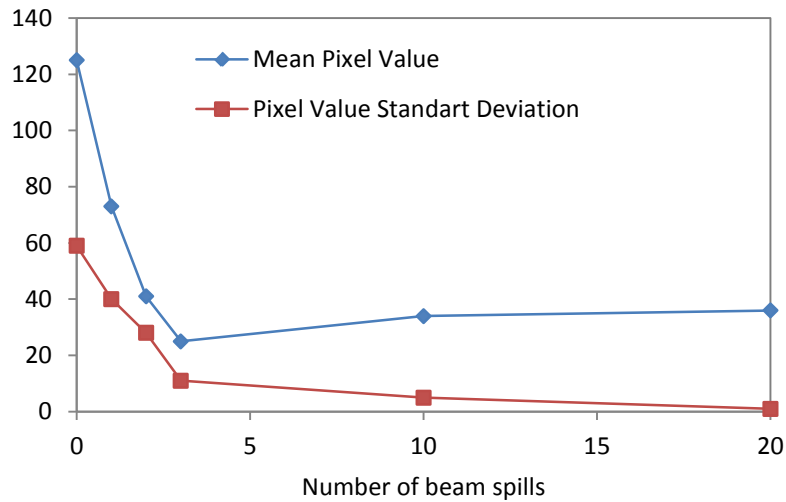


Fig. 5.15: Evolution of mean pixel grey value and STD of this value with number of heavy ion beam spills.



## 6. CCD based beam loss monitors

Studies of CCD cameras behavior in radiation environment described above has led to idea of application of CCD cameras as Beam Loss Monitors (BLMs).

BLMs operation is usually based on ionization phenomenon. There are many different types of BLMs with different materials serving as active element. And there are several important properties, which characterize a BLM: dynamic range, time resolution, size, lifetime in radiation environment, cost etc.

One of the most common BLMs is an Ionization Chamber (IC) (Fig. 6.1) [70-72]. ICs have slow response, low efficiency with gamma rays and do not register neutrons. But they are radiation hard and rather inexpensive. ICs are usually shaped as cylinders of 5-20 cm in diameter and 10-30 cm in length.



Fig. 6.1: Ionization Chamber BLM (yellow).

---

Scintillator-based BLMs [73-74] are sensitive to gamma rays, neutrons, electrons, and charged hadrons. They show fast response and very large dynamic range, but they are not radiation hard and comparatively expensive. The size of the active area is typically about  $20 \times 20 \times 50 \text{ mm}^3$ , but with the housing and amplification they end up about the same size as ICs.

$\text{BF}_3$  proportional tubes (Fig. 6.2) register only neutrons [74]. Such detectors are usually used at power plants. They have a slow response and they are expensive, but radiation hard.  $\text{BF}_3$  proportional tubes are usually about 15 mm in diameter and 400 mm in length.



Fig. 6.2:  $\text{BF}_3$  proportional tubes.

Solid state detectors, such as PIN diodes (Fig. 6.3) are used at many accelerators [75-76]. They are not very sensitive, but they show fast response. PIN diodes are inexpensive, but they have problems with radiation hardness, as any silicon-based equipment. They have a small size  $10 \times 10 \text{ mm}^2$  with an active layer of typically  $300 \text{ }\mu\text{m}$ .



Fig. 6.3: PIN diode beam loss monitor.

Electron multipliers (Fig. 6.4) are about as sensitive as ICs, but they have fast response and are radiation hard [77].

Optical fibers have the advantage of very high spatial resolution. They happen to be slow and not very sensitive [78]. Optical fibers are relatively radiation hard, too.

Results of our irradiation experiments showed at least two factors, which make CCD camera easy to calibrate and adjust as a detector for secondary radiation produced by heavy ion beam losses in a metal target. The first factor is good linearity and accuracy of charge versus number of lost ions within four orders of magnitude (Fig. 5.8). The second is good isotropic response to secondary radiation within angles from 25 to 60 degree to the primary beam direction (Fig. 5.9). Moreover it is possible to make estimations of prompt radiation effect on CCD cameras based on results of this study, allowing proper positioning of CCD cameras near beam lines for BLM purposes in future.

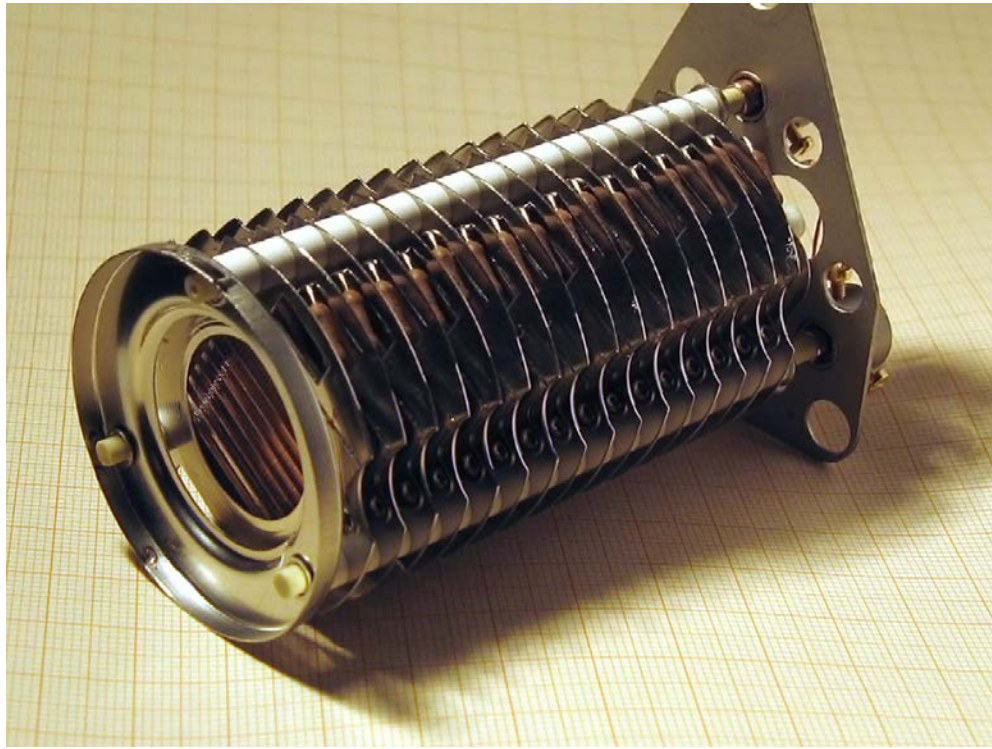


Fig. 6.4: Venetian blind electron multiplier.

Another LabVIEW based application was developed for in-situ acquisition and processing of CCD output for BLM purposes. Fig. 6.5 shows examples of in-situ data acquisition. These plots were captured during irradiation of a 10.8 cm long aluminium cylinder with a 0.5 GeV/u  $N^{+7}$  ion beam with camera in position 1 (Fig. 4.4) and beam intensities of  $1e10$ ,  $1e9$  and  $1e8$  ions/spill. A 100% beam losses in a small volume are simulated with these experiment conditions. Peaks on the plots are caused by beam spills lost in the aluminum target. Background is caused by the dark current in CCD matrix. It may increase with total dose. It is seen from the plots that the difference in peak height (applicable signal) is rather small. We assume that beam intensity is constant for all the spills and use standard deviation of the applicable signal for each series of measurements as an indication of accuracy of technique. We also use signal to background noise ratio to describe a possibility to distinguish the signal. These values are collected in table 6.1. It

shows that for chosen camera position in relation to loss point we may use this technique for  $1e9$  ions per spill and higher with reasonable accuracy. Registration of  $1e8$  ions per spill losses was already problematic due to background noise and higher deviations of the applicable signal. One may choose different camera positions depending on the expected beam losses.

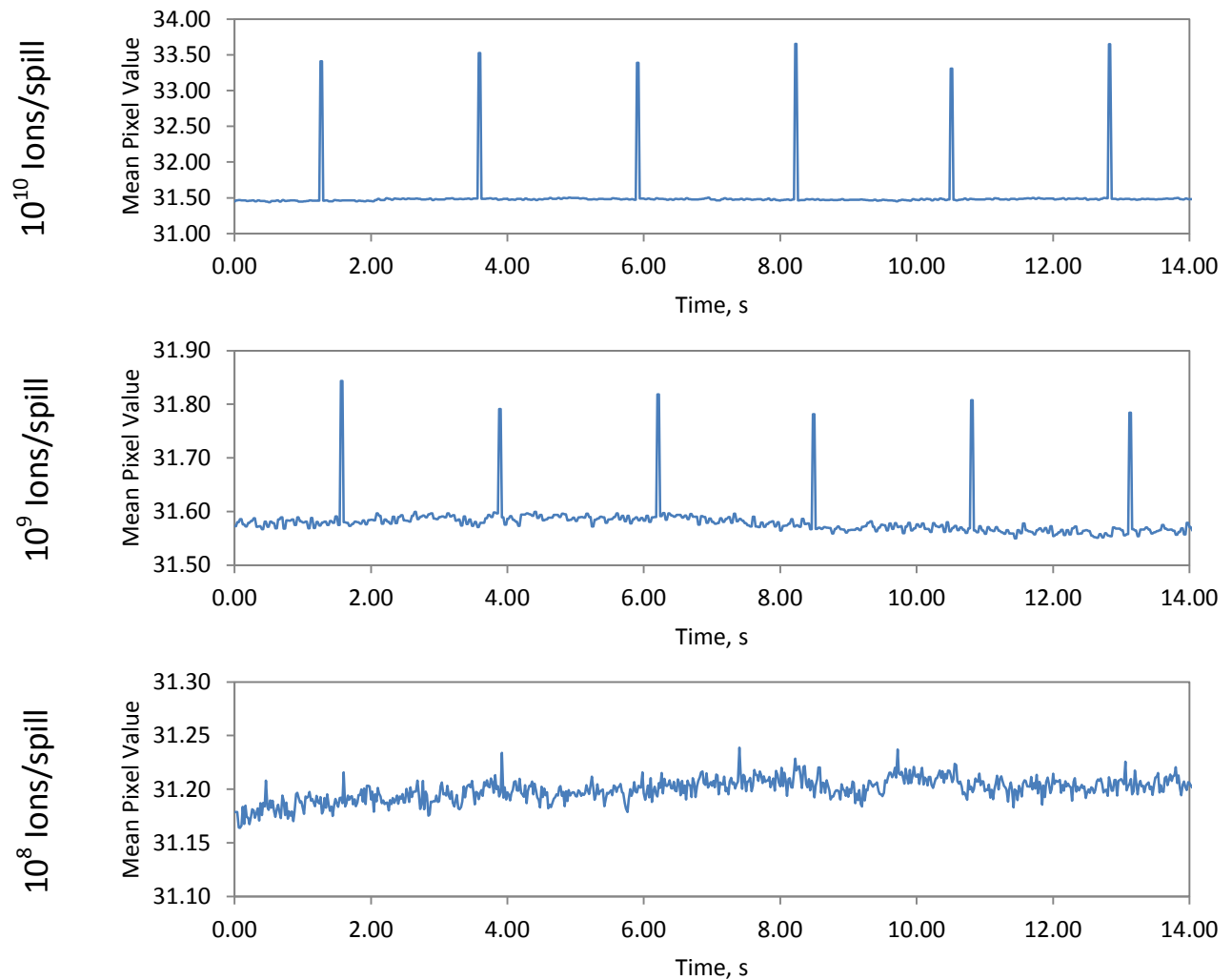


Fig. 6.5: Mean pixel grey value evolution with time. Data from irradiation of a 10.8 cm long aluminium cylinder with 0.5 GeV/u  $N^{+7}$  ion beam with camera in position 1 (Fig. 4.4) and beam intensities  $1e10$ ,  $1e9$  and  $1e8$  ions/spill.

Table 6.1: Standard deviation (STD) of the applicable signal and signal-to-noise ratio

Ion beam intensity, ions/pulse	applicable signal STD	signal/background noise
$10^{10}$	7%	73
$10^9$	10%	8.2
$10^8$	18%	1.1

A BLM system based on CCDs has several advantages and disadvantages:

- + small piece size. Compact size of such a detector allows multiple device installation for ultimate space resolution.

- + preinstalled devices. Normally there are plenty of different cameras, installed around the beam lines. They may serve as surveillance cameras, for scintillator profilometer observation, for target alignment and other purposes. These cameras may be calibrated for beam loss monitoring purposes as well, especially if they are equipped with a remote control shutter system.

- + comparatively inexpensive. Most of other BLM types have several times higher price per piece.

- low reliability of digital cameras. Digital devices are affected by SEU phenomena in radiation environment. Cameras may suffer from malfunctions from time to time, depending on level of prompt radiation. Normally in such cases they have to be hard-rebooted, i.e. powered off and back on. This process may be automated though.

---

- rather sensitive to total dose. Doses of about 0.5 kGy may be a lifetime limit for a common camera model. Depending on manufacturing process, chip size and feature size this value may differ.

Analogue cameras are proven to be much more reliable, because they are not affected by SEUs. A BLM system based on analogue cameras may be a very effective solution for the hottest spots of the accelerator and transport tunnels. Degradation of CCD chip with dose may be compensated by relatively low unit price and possibility of frequent replacement.



---

## 7. Summary

---

Short and long term effects of radiation to electronic devices in conditions typical for high energy heavy ion accelerators were studied in this work. CCD cameras, Ethernet switches and single transistor chips were tested in series of experiments with direct and indirect irradiation in the experimental hall behind the SIS18 heavy ion synchrotron. Criteria of lifetime and reliability in radiation environment of the accelerator were formulated for these devices based on experiment results. These criteria may be as well applicable to other typical semiconductor devices, used in the vicinity of heavy ion accelerators. Experience gained during this work and experimental methods used give a good groundwork for further detailed studies of radiation hardness on certain electronic components in heavy ion accelerator environment.

A series of Monte Carlo calculations were performed. These calculations helped to understand the typical particle composition of secondary radiation from heavy ion beam losses, their influence and energy deposition portion. Moreover these calculations together with experimental results are a very good reference point. This data help to predict device lifetimes and reliability in case of installation in different areas of constructed facilities or in case of upgrades. Each new facility component is usually modeled and tested for radiation safety and shielding design with the same Monte Carlo code FLUKA, that was used in this study. This fact makes comparisons more reliable and easy. Results of this study help to identify tolerable radiation conditions and design proper shielding for electronic components in FAIR buildings.

Prompt radiation effects on CCD cameras showed results that led to the idea to use CCD cameras as beam loss monitors in heavy ion accelerators. CCD

---

cameras show good linearity in response within a range of several orders of magnitude of beam losses. The noise level is rather low, but it increases with total dose, collected by the device. A calibration and simple software processing is required for proper interpretation of CCD camera readings into beam loss values. This system has certain advantages and disadvantages, but overall it may be a perspective direction.

# Appendix

FLUKA simulations of neutrons, protons, gammas, alphas, and heavy ions:

- Particle fluence (per primary ion)
- Linear energy transfer (LET per primary ion)
- Displacements per atom (DPA per primary ion)

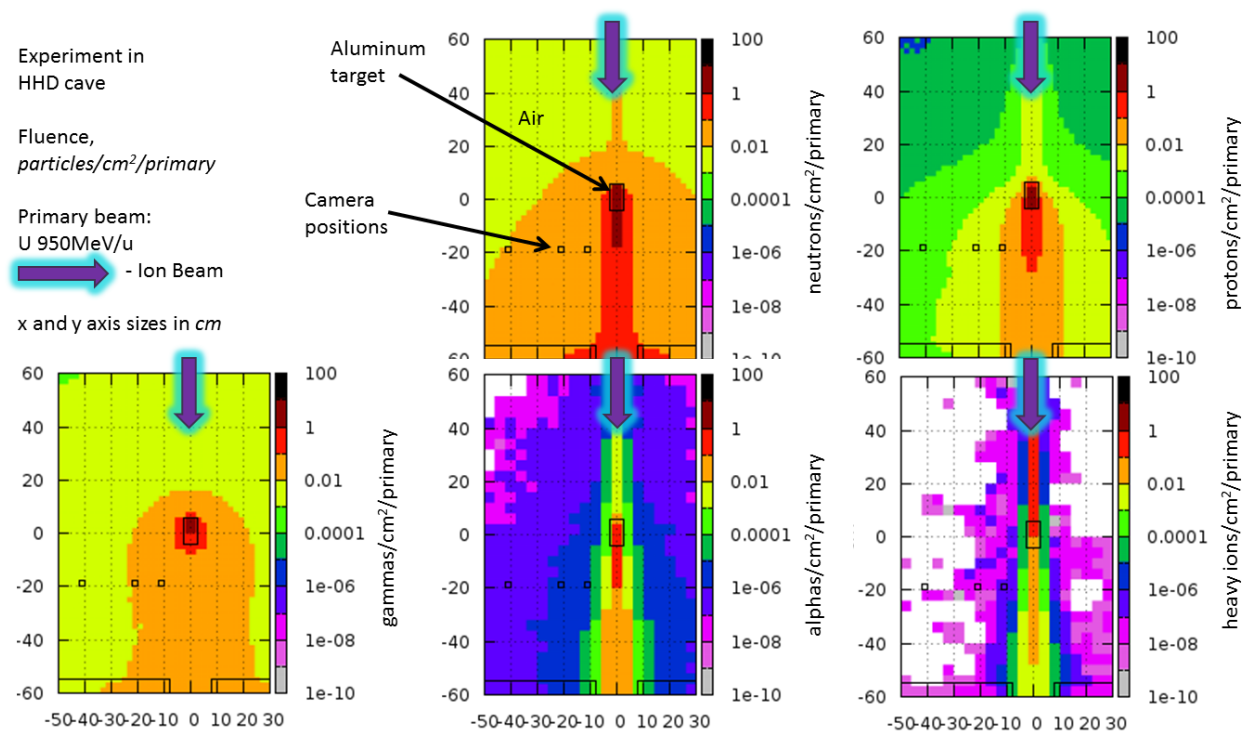


Fig. A.1: Monte Carlo FLUKA simulations of the experiment with U 950 MeV/u primary beam hitting Aluminum target. Particle fluence.

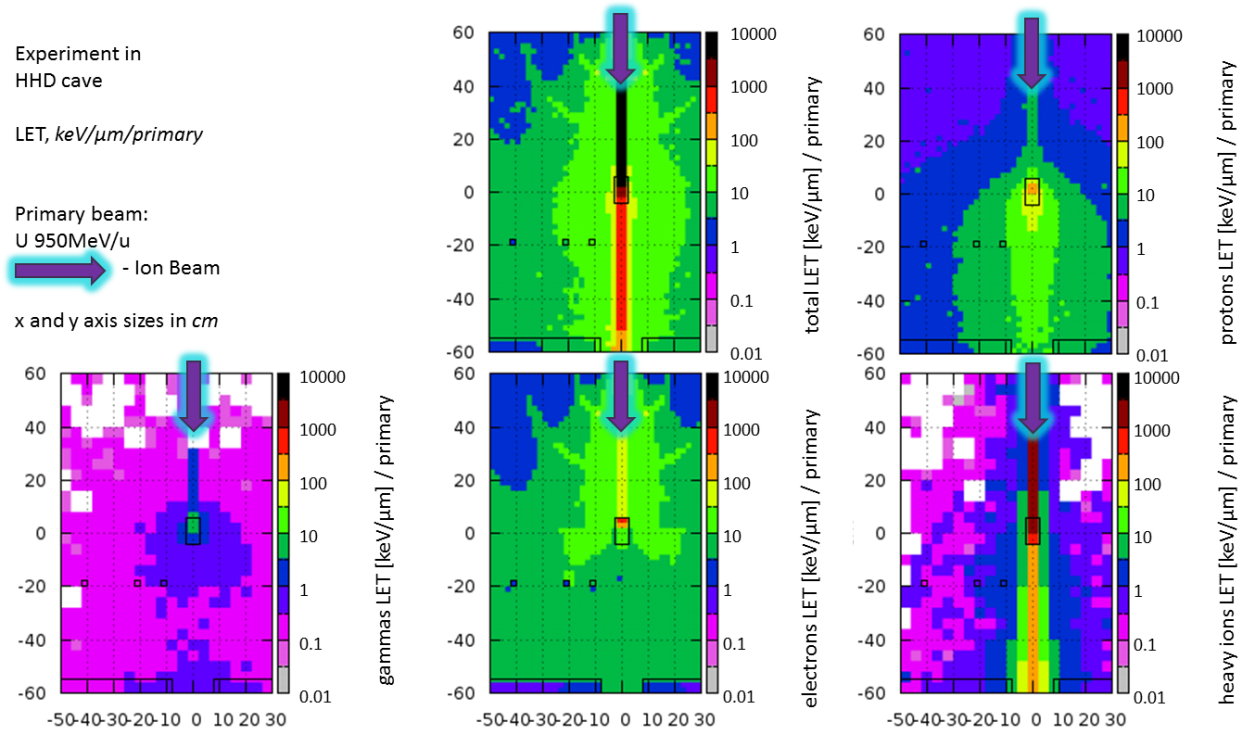


Fig. A.2: Monte Carlo FLUKA simulations of the experiment with U 950 MeV/u primary beam hitting Aluminum target. Particle LET.

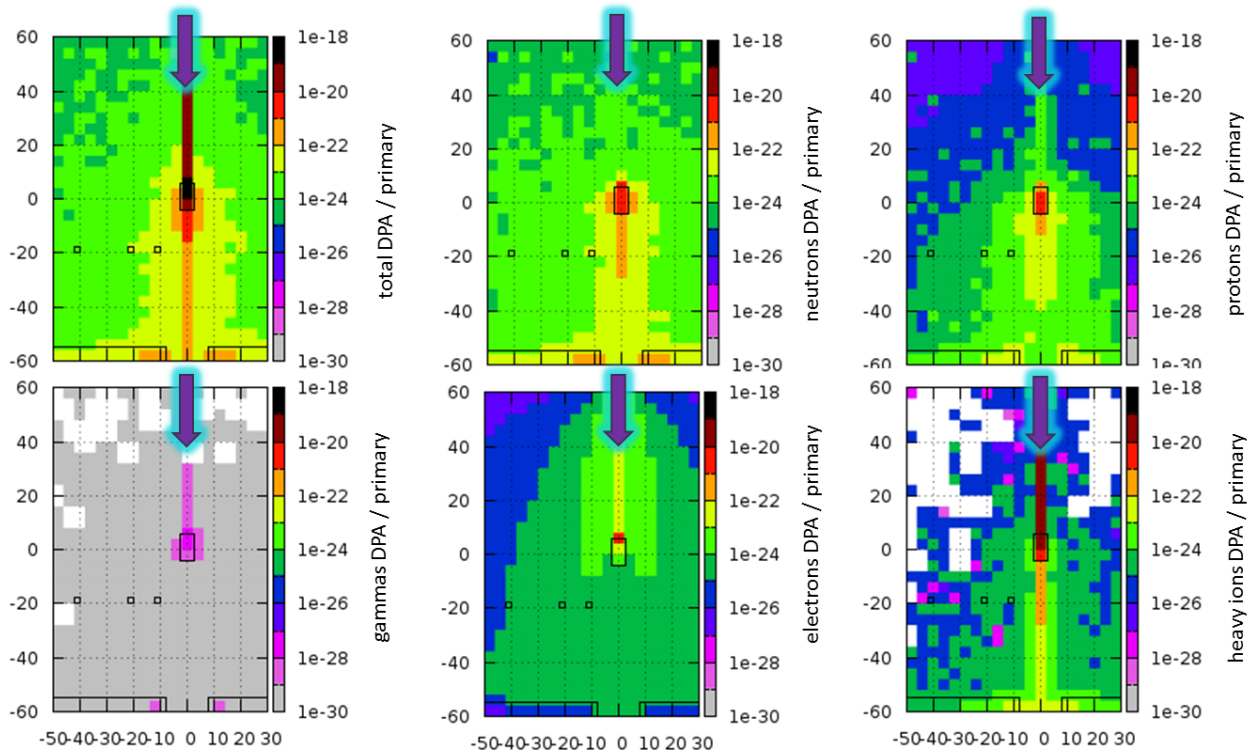


Fig. A.3: Monte Carlo FLUKA simulations of the experiment with U 950 MeV/u primary beam hitting Aluminum target. Particle DPA.

---

## References

- [1] The Effects of Nuclear Weapons Compiled and edited by Samuel Glasstone and Philip J. Dolan, Third Edition, Prepared and published by the United States Department of Defense and the Energy Research and Development Administration 1977.
- [2] Kopp, Carlo (October 1996). "The Electromagnetic Bomb - A Weapon of Electrical Mass Destruction". USAF CADRE Air Chronicles (U.S. Air Force). DTIC:ADA332511. Retrieved 12 January 2012.
- [3] IBM experiments in soft fails in computer electronics (1978–1994), from Terrestrial cosmic rays and soft errors, IBM Journal of Research and Development, Vol. 40, No. 1, 1996. Retrieved 16 April 2008.
- [4] Scientific American (2008-07-21). "Solar Storms: Fast Facts". Nature Publishing Group. Retrieved 2009-12-08.
- [5] Intel plans to tackle cosmic ray threat, BBC News Online, 8 April 2008. Retrieved 16 April 2008.
- [6] I. Augustin. Status of the FAIR project, Nuclear Instruments and Methods in Physics Research Section B: Beam Interactions with Materials and Atoms, Bd. 261, Nr. 1-2, Aug. 2007, pages 1014-1017.
- [7] P. Spiller and G. Franchetti. The FAIR accelerator project at GSI, Nuclear Instruments and Methods in Physics Research Section A, Bd 561, Nr. 2, June 2006, pages 305-309.
- [8] I. Augustin, H. H. Gutbrod, D. Krämer, K. Langanke, H. Stöcker. New Physics At The International Facility For Antiproton And Ion Research (Fair) Next To GSI, Invited Talk presented at the "Fourth International Conference on Fission and

---

Properties of Neutron-Rich nuclei", held at Sanibel Island, Florida, November 11-17, 2007.

[9] G. Barbottin and A. Vapaille. *Instabilities in Silicon Devices, New Insulators, Devices and Radiation Effects*. Elsevier, 1999.

[10] A. Jorio, A. Zounoubi, Z. Elachheb, C. Carlone, and S. M. Khann. Displacement damages created by  $\gamma$  particles radiation in n type GaAs. *M. J. of Condensed Matter*, 2(1), 1999.

[11] G. Messenger and M. Ash. *The Effects of Radiation on Electronic Systems*. Van Nostrand Reinhold Company Inc., 1986.

[12] L. Adams A. Holmes-Siedle. *Handbook of Radiation Effects*. Oxford University Press, 2004.

[13] F. Giustino. *Radiation Effects on Semiconductor Devices, Study of the Enhanced Low Dose Rate Degradation*. PhD thesis, Politecnico di Torino, 2001.

[14] R.A.B. Devine. The structure of  $\text{SiO}_2$ , its defects and radiation hardness. *IEEE Transactions on Nuclear Science*, 41(3), 1994, pages 452–459.

[15] F. Wrobel. *Fundamentals of Radiation-Matter interaction. New Challenges for Radiation Tolerance Assessment, Radiation Effects on Components and Systems*, 2005, pages 5–31.

[16] D. M. Fleetwood. Emerging issues for total ionizing dose effects on microelectronics. *New Challenges for Radiation Tolerance Assessment, Radiation Effects on Components and Systems*, 2005, pages 33–46.

- 
- [17] C. E. Barnes, D. M. Fleetwood, D. C. Shaw, and P. S. Winokur. Post irradiation effects (PIE) in integrated circuits. *IEEE Transactions on Nuclear Science*, 39(3), 1992, pages 328–341.
- [18] H. L. Hughes and J. M. Benedetto. Radiation effects and hardening of MOS technology: devices and circuits. *IEEE Transactions on Nuclear Science*, 50(3), 2003, pages 500–521.
- [19] O. Calvo, M. Gonzalez, C. Romero, E. Garcia-Moreno, E. Isern, M. Roca, and J. Segura. Integrated CMOS linear dosimeters. In: *Integrated Circuit Design, 1998. Proceedings. XI Brazilian Symposium on*, 1998, pages 78–81.
- [20] T. R. Oldham and F. B. McLean. Total ionizing dose effects in MOS oxides and devices. *IEEE Transactions on Nuclear Science*, 50(3), 2003, pages 483–499.
- [21] A. Paccagnell, A. Candelori, A. Milani, E. Formigoni, G. Ghidini, F. Pellizzer, D. Drera, P.G. Fuochi, and M. Lavale. Breakdown properties of irradiated MOS capacitors. *IEEE Transactions on Nuclear Science*, 43(6), 1996, pages 2609–2616.
- [22] M. Da Rold, A. Paccagnella, A. Da Re, G. Verzellesi, N. Bacchetta, R. Wheadon, G.-F. Dalla Betta, A. Candelori, G. Soncini, and D. Bisello. Radiation effects on breakdown characteristics of multiguarded devices. *IEEE Transactions on Nuclear Science*, 44(3), 1997, pages 721–727.
- [23] T. L. Meisenheimer and D. M. Fleetwood. Effect of radiation-induced charge on 1/f noise in MOS devices. *IEEE Transactions on Nuclear Science*, 37(6), 1990, pages 1696–1702.
- [24] Z. Li. Experimental comparisons among various models for the reverse annealing of the effective concentration of ionized space charges ( $n_{\text{eff}}$ ) of neutron

---

irradiated silicon detectors. IEEE Transactions on Nuclear Science, 42(4), 1995, pages 224–234.

[25] Z. Li, W. Chen, L. Dou, V. Eremin, H.W. Kraner, C.J. Li, G. Lindstroem, and E. Spiriti. Study of the long term stability of the effective concentration of ionized space charges ( $n_{\text{eff}}$ ) of neutron irradiated silicon detectors fabricated by various thermal oxidation processes. IEEE Transactions on Nuclear Science, 42(4), 1995, pages 219–223.

[26] O. Gilard and G. Quadri. Radiation effects on electronics: displacement damages. New Challenges for Radiation Tolerance Assessment, Radiation Effects on Components and Systems, 2005, pages 47–69.

[27] R. D. Schrimpf. Recent advances in understanding total-dose effects in bipolar transistors. In: Radiation and its Effects on Components and Systems, 1995. Radiation Effects on Components and Systems, Third European Conference on, 1995, pages 9–18.

[28] K. Makino, M. Berz, D. Errede, and C.J. Johnstone. Nonlinear transfer map treatment of beams through systems with absorbing material. In: Physics and Control, 2003. Proceedings. 2003 International Conference, volume 3, 2003.

[29] A. A. Hahn and J. R. Zagel. Observation of Bethe-Bloch ionization using the booster ion profile monitor. In: Particle Accelerator Conference, volume 1, 1999, pages 468–470.

[30] C. Detcheverry, C. Dachs, E. Lorfevre, C. Sudre, G. Bruguier, J.M. Palau, J. Gasiot, and R. Ecoffet. SEU critical charge and sensitive area in a submicron CMOS technology. IEEE Transactions on Nuclear Science, 44(6), 1997, pages 2266–2273.

- 
- [31] K. Label and L. Cohn. Radiation testing and evaluation issues for modern integrated circuits. *New Challenges for Radiation Tolerance Assessment, Radiation Effects on Components and Systems*, 2005, pages 71–93.
- [32] Actel. Effects of neutrons on programmable logic. White Paper, December 2002.
- [33] A. V. Sannikov. Single event upsets in semiconductor devices induced by highly ionizing particles. *Radiation Protection Dosimetry*, 110(1–4), 2004, pages 399–403.
- [34] R. B. Katz. Radiation effects on current field programmable technologies, *IEEE Transactions on Nuclear Science*, Volume 44, Issue 6, Part 1, 1997, pages 1945 – 1956.
- [35] A. Candelori. High-energy ion irradiation effects on thin oxide p-channel MOSFETs, *IEEE Transactions on Nuclear Science*, Volume 49, Issue 3, 2002, pages 1364 – 1371.
- [36] D. N. Nguyen and L.Z. Scheick. SEE and TID of emerging non-volatile memories. In: *Radiation Effects Data Workshop, 2002 IEEE*, 2002, pages 62–66.
- [37] F. Faccio. COTS for the LHC radiation environment: the rules of the game. Krakow, Poland, presented at the 6th Workshop on Electronics for LHC Experiments, 2000.
- [38] E. Mikkola, B. Vermeire, H. J. Barnaby, H. G. Parks, and K. Borhani. SET tolerant CMOS comparator. *IEEE Transactions on Nuclear Science*, 51(6), 2004, pages 3609–3614.

- 
- [39] Y. Boulghassoul, J. D. Rowe, and L. W. Massengill. Applicability of circuit macromodeling to analog single-event transient analysis. *IEEE Transactions on Nuclear Science*, 50(6), 2003, pages 2119–2125.
- [40] J. M. Benedetto, P. H. Eaton, D. G. Mavis, M. Gadlage, and T. Turflinger. Variation of digital set pulse widths and the implications for single event hardening of advanced CMOS processes. *IEEE Transactions on Nuclear Science*, 52(6), 2005, pages 2114–2119.
- [41] Y. Boulghassoul, L. W. Massengill, A. L. Sternberg, and B. L. Bhuva. Effects of technology scaling on the SET sensitivity of RF CMOS voltage-controlled oscillators. *IEEE Transactions on Nuclear Science*, 52(6), 2005, pages 2426–2432.
- [42] P. Mongkolkachit and B. Bhuva. Design technique for mitigation of alpha-particle induced single-event transients in combinational logic. *IEEE Transaction on Device and Materials Reliability*, 3(3), 2003, pages 89–92.
- [43] S. D. LaLumondiere, R. Koga, P. Yu, M. C. Maher, and S. C. Moss. Laser-induced and heavy ion-induced single-event transient (SET) sensitivity measurements on 139-type comparators. *IEEE Transactions on Nuclear Science*, 49(6), 2002, pages 3121–3128.
- [44] A. S. Sedra and K. C. Smith. *Microelectronics Circuits*. Oxford University Press, 1998.
- [45] G. Bruguier and J.-M. Palau. Single particle-induced latchup. *IEEE Transaction on Nuclear Science*, 43(2), 1996, pages 522–532.
- [46] J.L. Titus and C.F. Wheatley. Experimental studies of single-event gate rupture and burnout in vertical power MOSFETs. *IEEE Transactions on Nuclear Science*, 43(2), 1996, pages 533–545.

---

[47] J. R. Brews, M. Allenspach, R.D. Schrimpf, K.F. Galloway, J.L. Titus, and C.F.Wheatley. A conceptual model of a single-event gate-rupture in power MOSFETs. IEEE Transactions on Nuclear Science, 40(6), 1993, pages 1959–1966.

[48] J. L. Titus, C. F. Wheatley, K. M. Van Tyne, J. F. Krieg, D. I. Burton, and A.B.Campbell. Effect of ion energy upon dielectric breakdown of the capacitor response in vertical power MOSFETs. IEEE Transactions on Nuclear Science, 45(6), 1998, pages 2492–2499.

[49] M. N. Darwish, M. A. Shibib, M. R. Pinto, and J. L. Titus. Single event gate rupture of power DMOS transistors. Washington, DC, USA, Electron Devices Meeting, 1993. Technical Digest., International, 1993, pages 671–674.

[50] R. Koga and W.A. Kolasinski. Heavy ion induced snapback in CMOS devices. IEEE Transactions on Nuclear Science, 36(6), 1989, pages 2367–2374.

[51] Y. Fong and C. Hu. High-current snapback characteristics of MOSFETs. "IEEE Trans. Electron Devices", 37(9), 1990, pages 2101–2103.

[52] <http://www.fluka.org/fluka.php?id=about>

[53] G. Battistoni, S. Muraro, P.R. Sala, F. Cerutti, A. Ferrari, S. Roesler, A. Fasso`, J. Ranft, The FLUKA code: Description and benchmarking Proceedings of the Hadronic Shower Simulation Workshop 2006, Fermilab 6-8 September 2006, M. Albrow, R. Raja eds., AIP Conference Proceeding 896, 2007, pages 31-49.

[54] A. Ferrari, P.R. Sala, A. Fasso`, and J. Ranft, FLUKA: a multi-particle transport code. CERN-2005-10, 2005, INFN/TC\_05/11, SLAC-R-773.

[55] <http://www.fluka.org/flair/>

---

[56] H. Reeg and N. Schneider, Current transformers for GSI's keV/u to GeV/u ion beams - an overview, in Proceedings of the Fifth European Workshop on Diagnostics and Beam Instrumentation DIPAC2001, ESRF, Grenoble, France, 2001, PS08.

[57] I. Strašík, V. Chetvertkova, E. Mustafin, M. Pavlovič, A. Belousov, Depth profiling of residual activity of  $^{237}\text{U}$  fragments as a range-verification technique for  $^{238}\text{U}$  primary ion beam. Physical Review Special Topics Accelerators and Beams 15, 2012, pages 071001(13).

[58] V. Chetvertkova, I. Strasik, A. Belousov, H. Iwase, N. Mokhov, E. Mustafin, L. Latysheva, M. Pavlovic, U. Ratzinger, N. Sobolevsky. Activation of aluminum by argon: Experimental study and simulations. Nuclear Instruments and Methods in Physics Research B 269, 2011, page 1336.

[59] [http://datasheet.eeworld.com.cn/pdf/INFINEON/357415\\_BSS131.pdf](http://datasheet.eeworld.com.cn/pdf/INFINEON/357415_BSS131.pdf)

[60] [http://www.baslerweb.com/media/documents/BD00041201\\_Basler\\_scA640-74gm\\_EMVA\\_Standard\\_1288.pdf](http://www.baslerweb.com/media/documents/BD00041201_Basler_scA640-74gm_EMVA_Standard_1288.pdf)

[61] <http://www.ni.com/LabVIEW/>

[62] EMVA Standard 1288 Standard for Characterization of Image Sensors and Cameras Release 3.0 November 29, 2010 Issued by European Machine Vision Association, [www.emva.org](http://www.emva.org)

[63] J. R. Janesick, CCD characterization using the photon transfer technique. In: Prettyjohns, K. and E. Derenlak, eds., Solid State Imaging Arrays, vol. 570 of SPIE Proceedings, 1985, pages 7-19.

[64] J. R. Janesick, Photon Transfer. SPIE Press Monograph, vol. PM170, 2007.

[65] <http://h30094.www3.hp.com/product/sku/10208301>

---

[66] R. B. Hayes, E. H. Haskell, A. Wieser, A. A. Romanyukha, B. L. Hardy, J. K Barrus. Assessment of an Alanine EPR Dosimetry Technique with Enhanced Precision and Accuracy, Nuclear Inst. and Methods in Physics Research, a, volume 440 issue 2 (30 November 1999), pages 453-461.

[67] H. Feist, D. Regulla, A. Wieser, Is alanine/ESR dosimetry now an alternative to ferrous sulphate dosimetry? GSF-Forschungszentrum für Umwelt und Gesundheit D(W)-8042 Neuherberg, Germany; Radiologische Klinik der Universität München D(W)-8000 München 70, Germany Applied Radiation and Isotopes, 1993.

[68] H. Schraube, E. Weitzenegger, A. Wieser, D. Regulla, Fast neutron response of alanine probes. Gesellschaft für Strahlen- und Umweltforschung (GSF) München, D-8042 Neuherberg, F.R.G. International Journal of Radiation Applications and Instrumentation Part A Applied Radiation and Isotopes, 40, 1989, pages 941-944.

[69] A. Belousov, E. Mustafin, W. Ensinger, Short and long term ionizing radiation effects on charge-coupled devices in radiation environment of high-intensity heavy ion accelerators. Journal of Instrumentation, Volume 7, November 2012, C11002.

[70] E. B. Holzer, B. Dehning, E. Effinger, J. Emery, V. Grishin, C. Hajdu, S. Jackson, C. Kurfuerst, A. Marsili, M. Misiowiec, M. Nagel, E. Nebot Del Busto, A. Nordt, C. Roderick, M. Sapinski, C. Zamantzas, Beam Loss Monitoring for LHC Machine Protection. Physics Procedia, Volume 37, 2012, pages 2055-2062.

[71] L. Sarchiapone, M. Brugger, B. Dehning, D. Kramer, M. Stockner, V. Vlachoudis Mario Bocciolini, Antonio Conti, Giuliano di Caporiacco, Giuliano Parrini, Angela Quarenì Vignudelli, FLUKA Monte Carlo simulations and

---

benchmark measurements for the LHC beam loss monitors. Nuclear Instruments and Methods in Physics Research Section A: Accelerators, Spectrometers, Detectors and Associated Equipment, Volume 581, Issues 1–2, 21 October 2007, pages 511-516.

[72] R. E. Shafer et al., Proceedings international Conference High Energy Accelerators, Batavia, 1983, page 609 and D. Gassner et al., Beam Instrumentation Workshop BIW 2000, Cambridge, 2000, page 392.

[73] J. R. Parker et al., A beam-spill monitor for LAMPF, IEEE Transactions on Nuclear Science, 18, 1971, pages 825–826.

[74] G. Knoll, Radiation Detection and Measurement, JohnWiley, New York, 1999.

[75] K. Wittenburg, Specific instrumentation and diagnostics for high-intensity hadron beams, 9<sup>th</sup> Beam Instrum. Workshop BIW, Cambridge, 2000, page 3.

[76] V. D. Shiltsev, Fast PIN-diode beam loss monitors at Tevatron, Nuclear Instruments and Methods in Physics Research Section A: Accelerators, Spectrometers, Detectors and Associated Equipment, Volume 411, Issue 1, 1 July 1998, pages 81-92.

[77] G. C. Smith, G. P. Williams, A channel electron multiplier and optically coupled amplifier used as an incident flux monitor, Nuclear Instruments and Methods in Physics Research, Volume 222, Issues 1–2, 15 May 1984, pages 262-265.

[78] Zhen Xue, Tao Hu, Jian Fang, Zi-Zong Xu, Xiao-Lian Wang, Jun-Guang Lü, Li Zhou, Xiao Cai, Bo-Xiang Yu, Zhi-Gang Wang, Li-Jun Sun, Xi-Lei Sun, Ai-Wu Zhang, The radiation hardness of silica optical fiber used in the LED-fiber

---

monitor of BLM and BESIII EMC. Nuclear Instruments and Methods in Physics Research Section A: Accelerators, Spectrometers, Detectors and Associated Equipment, Volume 664, Issue 1, 1 February 2012, pages 71-74.



---

List of conferences attended:

1. 12th European Conference on Radiation and its Effects on Components and Systems (RADECS 2011) : Sevilla, Spain, September 19-23, 2011
2. Applied Physics of Condensed Matter (APCOM 2012), 18 th international conference in the series of the Solid State workshops, Štrbské Pleso, High Tatras, Slovak Republic, June 20-22, 2012. **Talk, proceedings.**
3. 14th International Workshop on Radiation Imaging Detectors (IWORID 2012), 1-5 July 2012 Figueira da Foz, Coimbra, Portugal. **Poster, proceedings.**

List of publications:

1. **A Belousov**, E Mustafin, W Ensinger, CCD based beam loss monitor for ion accelerators, Nuclear Instruments and Methods in Physics Research A, Volume 743, 11 April 2014, pages 86–89
2. **A Belousov**, E Mustafin, W Ensinger, Short and long term ionizing radiation effects on charge-coupled devices in radiation environment of high-intensity heavy ion accelerators, Journal of Instrumentation, Volume 7, November 2012, C11002
3. I Strašik, V Chetvertkova, E Mustafin, M Pavlovič, **A Belousov**, Depth profiling of residual activity of <sup>237</sup>U fragments as a range verification technique for <sup>238</sup>U primary ion beam, Physical Review Special Topics - Accelerators and Beams, 15(7), July 2012, pages 071001(13)
4. V Chetvertkova, I Strasik, **A Belousov**, H Iwase, N Mokhov, E Mustafin, L Latysheva, M Pavlovic, U Ratzinger, N Sobolevsky, Activation of aluminum by argon: Experimental study and simulations, Nuclear Instruments and Methods in Physics Research B, Volume 269, 15 June 2011, pages 1336–1340



---

Belousov Anton

01 Aug 1987

*Messeler-Park-Str. 119A, 64291 Darmstadt, Germany*

a.belousov@gsi.de

## EDUCATION:

- 2010– current Technische Universität Darmstadt, Materials Science Department.  
PhD thesis: “Radiation effects on semiconductor devices in high energy heavy ion accelerators”
- 2004 – 2010 M. V. Lomonosov Moscow State University, Faculty of Physics,  
General Nuclear Physics Department. GPA 4.5 out of 5.0  
Diploma thesis: “Extraction of the cross section for elastic electron-proton scattering at a beam energy  $E = 2.039$  GeV”  
Yearly project (2008): “HPGe detector response modeling”
- 2001 – 2004 Physical and Mathematical School N2
- 1994 – 2001 School of the intensive English N1260
- 1994 – 2001 Art School

## EXPERIENCE:

- 2011 – 2013 Investigated radiation effects to semiconductor elements:
- Designed and successfully carried out several experiments at the GSI heavy ion accelerator.
  - Performed Monte Carlo simulations of the experiments, using FLUKA.
  - Created a LabVIEW based software for CCD cameras, featuring extended control and acquisition considering specific needs of the study.
- Calculated shielding for the FAIR experimental hall being built, using FLUKA Monte Carlo code. Published twice and contributed to one conference. Supervised a foreign student in the summer program: assigned tasks and controlled work progress.

- 
- 2010 Performed Monte Carlo simulations of heavy ion beam interaction with Aluminum, using Geant4. Published results in NIM B journal.
  - 2010 Analyzed experimental data from Jefferson Lab, using ROOT data analysis framework.
  - 2008 Performed Monte Carlo simulations of HPGe detector operation with Geant4 and developed a code for analysis of the detector response, using ROOT.

---

## ACKNOWLEDGEMENTS

I would like to thank Prof. W. Ensinger for giving me an opportunity to study in TU and do my research in GSI facility.

I address my greatest gratitude to my advisor Dr. Edil Mustafin, who introduced me to GSI and gave a lot of useful advices during my research.

I would like to thank the following coworkers for pieces of advice, interesting discussions and help with experimental equipment: Harald Brauning, Sven Loechner, Andreas Reiter, Beata Walasek-Hoehne, Rosemarie Vinchelli, Ralph Baer, Niels Pyka, Ivan Strasik, Wolfgang Schiebel, Rainer Haseitl.

Many thanks to GSI accelerator operators and radiation safety personnel for being kind and helpful during beam times and equipment installation/removal.

I kindly thank Paola Karampougiouki for helping me with all kinds of organization and communication issues.

Special thanks to Vera Chetvertkova, who was my contact person together with Edil Mustafin, when I started my application to do my PhD study in GSI.

I am eternally grateful to my family, and especially to my parents, who invested a lot of their energy and time in me.

